



Universität Hamburg  
DER FORSCHUNG | DER LEHRE | DER BILDUNG

## Dissertation

zur Erlangung des akademischen Grades eines Doktors der  
Naturwissenschaften (Dr. rer. nat.) an der Universität Hamburg

---

# **Supramolecular Assemblies of Hybrid Nanoparticles towards Biomedical Applications**

---

vorgelegt von

**Leroy Marwin Nack**

geboren am 09.12.1995

in Hamburg

Fakultät für Mathematik, Informatik und Naturwissenschaften

Institut für Nanostruktur- und Festkörperphysik

**2022**

These experimental studies were carried out under supervision of Prof. Dr. Wolfgang Parak at the Institute of Nanostructure and Solid-State Physics (Faculty of Mathematics, Informatics and Natural Sciences) of the University of Hamburg between October 2019 and October 2022.

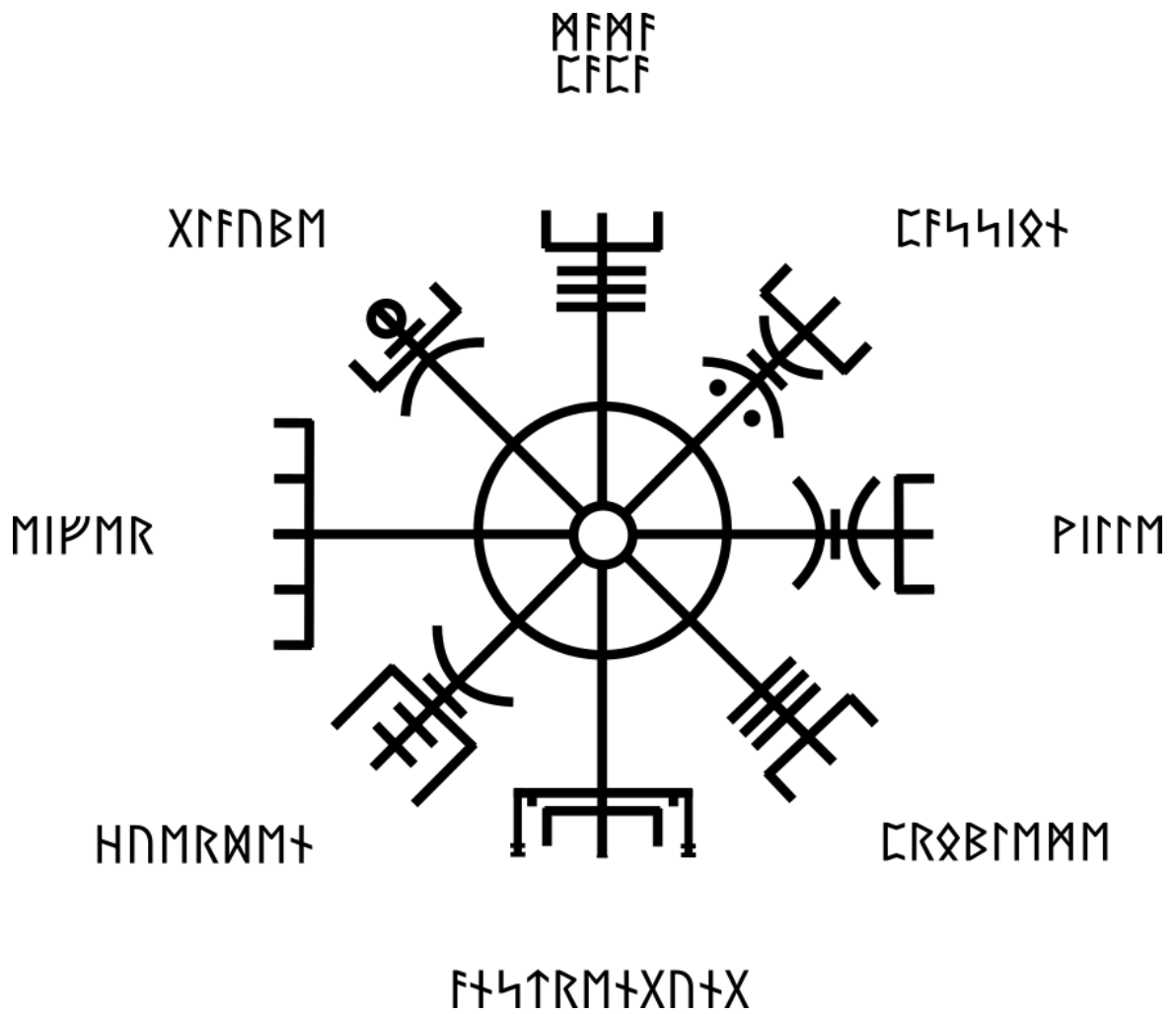
**Date of Submission:**                      **October 7, 2022**

**Thesis Examinators:**                      **Prof. Dr. Wolfgang Parak**  
**Prof. Dr. Carmen Herrmann**

**Date of Disputation:**                      **December 9, 2022**

**Disputation Committee:**                      **Prof. Dr. Wolfgang Parak**  
**Prof. Dr. Michael Steiger**  
**Prof. Dr. Alf Mews**

Important information: All names or labels mentioned in this thesis may be registered labels appertaining to their owner. Possible industrial rights violations are not intended.



“If this sign is carried,  
 one will never lose one’s way  
 in storms or bad weather,  
 even when the way is not known.”



## List of Publications

1. Y. Kang, **L. Nack**, Y. Liu, B. Qi, Y. Huang, Z. Liu, I. Chakraborty, F. Schulz, A. Ahmed, M. Clavo Podeva, F. Hafizi, S. Roy, M. Mutas, M. Holzapfel, K. David Wegner, N. Feliu, W. Parak, **“Quantitative considerations about the size dependence of cellular entry and excretion of colloidal nanoparticles for different cells”**, *ChemTexts* **8, 9** (2022).
2. S. Hecht, **L. Nack**, Y. Zhou, D. Zhu, W. Parak, **Probing Cell Viability by Using Light-Mediated Read-Out**, *In progress*.

## Conference Contributions

1. **NanoMed 2021**: NanoMedicine International Conference and Exhibition 2021 – as part of the joint conference additionally including Smart Materials and Surface (SMS 2021) and European Graphene Forum (EGF 2021), Milan, Italy, 20. – 22. Oktober 2021 (Poster presented: **“Magnetically Induced Cargo Release Inside Living Cells”**). Website: <https://www.setcor.org/conferences/nanomed-2021>, **Poster awarded as Best Poster.**

## Internships

1. **CiQUS**: Centro Singular de Investigación en Química Biolóxica e Materiales Moleculares / Center for Research in Biological Chemistry and Molecular Materials, Montenegro Lab, University of Santiago de Compostela (USC), **“Etching of Gold Cages from Silver Precursors for Use in Supramolecular Organic Frameworks (SOFs)”**, June 2022 – August 2020 (10 Weeks).

## Abstract

Drug delivery remains one of the most investigated fields in scientific medicine.<sup>1</sup> Control over dose, liberation rate and time, degradation as well as many other factors is crucial for medical application in the human body.<sup>2,3</sup> With development of the micro- and nanoscopic scale, multiple new opportunities were enabled. From then on, carrier size could be decreased significantly. Polyelectrolyte multilayer-capsules (PEMCs) represent one example for an encouraging candidate as they offer tuneable sizes across both the nano- and the micrometre regime. To date, controlled opening of PEMCs as well as corresponding biomedical applications have already been extensively studied. In this process, several trigger systems were developed to enable remote opening. Two methods to be highlighted here are laser- and magnetically induced mechanisms. Use of NIR-lasers and photothermal heating already shows reliable delivery of encapsulated cargo *in vitro*. When focused onto single capsules, release success-rates are very high.<sup>4-7</sup> Compared to well-investigated laser-induced opening, alternating magnetic fields (AMFs) are poorly probed as triggers.<sup>8-10</sup> Due to their deep penetration depth into thick biological samples without damage, which is enabled by significantly reduced absorption, they are highly favoured.<sup>8</sup> Moreover, the lateral field expansion allows for irradiation of multiple carriers simultaneously.

Herein, the development process of magneto-responsive polyelectrolyte microcapsules for controlled release is described. Given various magnetic nanoparticles (MNPs), being known as heat-mediators for hyperthermia therapy, their exploitability as trigger sources for capsule opening *in vitro* is evaluated initially. To achieve high heat-generation efficiency, MNPs with different shapes and sizes ranging from 10 nm to 147 nm were prepared. The most promising representatives, showing extremely high specific absorption rate (SAR) values of up to more than 1000 W/g, were integrated into the microcapsules. At that, carrier functionalization is achieved by insertion of the MNPs into the shell. Afterwards, AMF-triggered controlled release of the encapsulated cargo is monitored inside different cancer cell lines and the corresponding pass rates are evaluated. To visualize the cargo release, a highly fluorescent dye molecule (calcein) is loaded into the cavity. Different encapsulation strategies are adjusted and optimized to minimize premature and maximize triggered release. In the presence of AMFs, the MNPs are able to produce sufficient heat to destroy the surrounding polymer shell, leading to dye release from the confined situation inside the capsules towards the cell cytosol. The delivery ratios thereby range in a regime of 10 % or below. A detailed look on the factors hampering heat generation and release during *in vitro* trials is pointed out subsequently. It provides an

explanation for low cargo delivery tendencies of the present system and compares it to an excellently working system: laser-induced opening via infrared radiation treatment. Strong discrepancies in local temperature during illumination are recorded. Accordingly, the first part of this elaboration demonstrates the possibility of magnetoresponsive capsule opening inside living cells under specific circumstances but simultaneously points out the critical restrictions and issues for potential biomedical use. In the second thesis part, laser-induced opening is transferred onto 3D-cell systems. Under use of both plasmonic and magnetic nanoparticles, the possibility of cargo release from PEMCs into single cells being located deeply inside tumor spheroids is tested. While opening of carriers located on the surface is a common technology, the process has only scantily been recorded deeply inside the spheroid centre. To confirm the carrier positioning, differently coloured capsules are distributed across the whole cell bundle and the colour spread is imaged. In this way, just specific capsules in the middle part can be chosen for examination, legitimizing their big distance from the surface. Then, individual PEMCs are illuminated, and cargo movement is imaged. Fluorescent dyes, thereby, enable direct observation of delivery under fluorescence microscopy and allow for simultaneous execution of viability testing. When irradiated by NIR laser-light, opening is also achievable behind tens of micrometres of stacked cells. Multiple runs with independent capsules confirm success and reproducibility of deep-tissue release.

Overall, two different trigger-systems for capsule disruption are investigated for release opportunities in living cell systems. It is pointed out that magnetism doesn't represent an equivalent to established triggers in terms of release due to many unmanageable problems. For its light-responsive counterpart the exploitability is, however, expanded towards deep-level viability examination.

## Zusammenfassung

Gezielte lokale Freisetzung medizinischer Substanzen stellt eines der am stärksten untersuchten Felder wissenschaftlicher Medizin dar. Dabei ist die Kontrolle über Dosis, Bereitstellungsrate und -zeit, Zersetzung und viele weitere Faktoren entscheidend für die medizinische Anwendung im menschlichen Körper. Mit der Entdeckung der Mikro- und Nanoskala eröffneten sich viele neue Möglichkeiten. Von diesem Zeitpunkt an konnte die Größe der Transportmoleküle deutlich reduziert werden konnte. Polyelektrolytkapseln (PEMCs) sind dabei, dank ihrer im Mikro- und Nanobereich modifizierbaren Größe, ein vielversprechender Kandidat. Zum jetzigen Zeitpunkt sind kontrollierte Öffnungsvorgänge solcher PEMCs sowie damit verbundene biomedizinische Anwendungen bereits für viele Triggersysteme intensiv untersucht worden. Zwei spezielle Methoden, die in der vorliegenden Ausarbeitung eine spezifische Rolle spielen, sind Öffnungsmechanismen auf Basis von Lasern und Magnetfeldern. Die Nutzung von NIR-Lasern in Verbindung mit photothermischem Heizen ermöglicht bereits eine zuverlässige Bereitstellung eingekapselter Ladung *in vitro*. Fokussierung des Lasers auf einzelne Kapseln liefert hohe Erfolgsraten. Im Vergleich zum umfassend untersuchten lichtinduzierten Öffnen sind alternierende magnetische Felder (AMFs) als Auslöser dagegen wenig erforscht. Dank ihrer Fähigkeit, tief und schadensfrei in dicke biologische Proben einzudringen, die auf deutlich verringerter Absorption beruht, sind sie allerdings deutlich vielversprechender. Außerdem erlaubt die große laterale Ausdehnung der Felder eine Bestrahlung etlicher Kapseln zur gleichen Zeit.

In dieser Ausarbeitung wird der Entwicklungsprozess magnetisch-reaktiver Polyelektrolyt-Mikrokapseln beschrieben. Auf Basis von verschiedenen magnetischen Nanopartikeln (MNPs), die ursprünglich als Hitzequelle für die Therapie mittels Hyperthermie bekannt sind, wird eingangs deren Nutzbarkeit als Auslöser für gesteuertes Öffnen von Kapseln *in vitro* bewertet. Um hohe Effizienz bei der Hitzeerzeugung zu erreichen sind unterschiedlichst geformte MNPs im Größenbereich von 10 nm bis 147 nm hergestellt worden. Die herausragendsten unter ihnen, welche extrem hohe Werte der Spezifischen Absorptionsrate (SAR) im Bereich bis über 1000 W/g aufweisen, sind in die Mikrokapseln integriert worden. Die Kapseln sind dabei durch die Insertion der MNPs in ihre Hülle funktionalisiert worden. Anschließend wird die Freisetzung aufgenommener Ladung mittels AMF-Bestrahlung in verschiedenen Krebszelllinien bewertet und dargestellt. Um die Freisetzung der Ladung sichtbar zu machen, werden die Kapseln mit einer stark-fluoreszierenden Farbstoffsubstanz (Calcein) beladen. In Anwesenheit von AMFs zeigen die MNPs eine ausreichend starke Hitze-generation, sodass die sie umgebende Hülle beschädigt und das Farbmolekül vom beschränkten Raum in der Kapsel

ins umgebende Zellcytosol freigesetzt wird. Die Freisetzungsrates bewegt sich dabei im Bereich bis maximal 10 %. Im darauffolgenden Abschnitt wird ein detaillierter Blick auf die Faktoren geworfen, die Hitzeerzeugung und Freisetzung *in vitro* behindern. Zum einen ergibt sich dabei eine Erklärung für die geringen Freisetzungsrates des vorliegenden Systems. Des Weiteren wird ein Vergleich mit einem exzellent arbeitenden System geliefert: Laser-basiertes Öffnen mittels Infrarotbestrahlung. In diesem Zusammenhang werden deutliche Unterschiede in der lokal vorliegenden Temperatur während der Bestrahlung beobachtet. Dementsprechend zeigt dieser Teil der Ausarbeitung die prinzipielle Möglichkeit, Kapseln unter bestimmten Umständen auf magnetische Weise in lebenden Zellen zu öffnen, stellt aber gleichzeitig die kritischen Einschränkungen und Probleme für potenzielle Bioanwendungen dar. Im zweiten Teil der Thesis ist Laser-basiertes Öffnen auf dreidimensionale Zellsysteme transferiert worden. Unter Nutzung von sowohl plasmonischen als auch magnetischen Nanopartikeln wurde die Realisierbarkeit von Ladungsablieferung aus PEMCs tief im Inneren von Tumorsphäroiden untersucht. Während das derartige Öffnen von auf der Oberfläche befindlichen Transporter bereits gängige Praxis ist, gibt es über den Prozess im Zentrum der Sphäroide nur spärliche Aufnahmen. Um ihre Position abzusichern, werden verschiedenfarbige Kapseln über das gesamte Zellbündel verteilt und die komplette Farbverteilung aufgenommen. Auf diese Weise können zur Untersuchung explizit Kapseln im Mittelteil ausgewählt und damit ihre große Distanz zur Oberfläche gewährleistet werden. Einzelne PEMCs werden dann bestrahlt und die Farbstoffbewegung aufgezeichnet. Fluoreszente Farbstoffe ermöglichen dabei eine direkte Beobachtung mittels Fluoreszenzmikroskopie und erweitern das Einsatzgebiet auch um gleichzeitige Analyse der Lebensfähigkeit. Unter NIR-Bestrahlung zeigt sich auch hinter Dutzenden von Mikrometern an gestapelten Zellen eine erfolgreiche Freisetzung. Mehrere Durchläufe mit unabhängigen Kapseln belegen Erfolg und Reproduzierbarkeit. In Summe werden zwei verschiedene Auslöser-Systeme zur Kapselöffnung in lebenden Zellen untersucht. Es wird gezeigt, dass Magnetismus aufgrund von unkontrollierbaren Problemen mit der Freisetzung in diesem Bereich kein Äquivalent zu etablierten Auslösesystemen darstellt. Das lichtabhängige Gegenstück wird dagegen um die Untersuchung der Zellebensfähigkeit in tieferliegenden Anwendungsgebieten erweitert.

# Table of Contents

|   |     |
|---|-----|
| Abstract  | I   |
| Zusammenfassung   | III |
| Table of Contents   | V   |
| Table of Abbreviations  | VII |
| Introduction  | 1   |
| 1 Theory/State-of-the-Art                                       | 3   |
| 1.1 Magnetic Nanoparticles                                      | 3   |
| 1.2 Plasmonic Nanoparticles                                     | 6   |
| 1.3 Magnetothermal Heating                                      | 9   |
| 1.4 Photothermal Heating  | 11  |
| 1.5 Polyelectrolyte Capsules                                    | 12  |
| 1.6 Cancer Cells as Model Systems                               | 14  |
| 1.7 Viability assays  | 16  |
| 1.8 Two-Photon Microscopy                                       | 17  |
| Main Project: Magnetothermal Cargo Delivery <i>in vitro</i>     |     |
| 2 Objective/Motivation  | 20  |
| 3 Materials, Synthesis and Methods                              | 22  |
| 3.1 Materials   | 22  |
| 3.2 Elemental Analysis  | 23  |
| 3.3 Synthesis   | 23  |
| 3.4 Water Transfer of Magnetic Nanoparticles                    | 23  |
| 3.5 Synthesis and Functionalization of Polyelectrolyte Capsules | 24  |
| 3.6 2D Cell Culture and Capsule Incubation                      | 25  |
| 3.7 3D Cell Culture   | 25  |
| 3.8 Imaging Principle   | 26  |
| 3.9 Magnetic Heating  | 26  |
| 3.10 Flow Cytometry   | 27  |
| 3.11 Thermal Imaging  | 28  |
| 4 Results   | 29  |
| 4.1 Improving Particle Properties and Heating Behavior          | 29  |
| 4.2 Capsule Characterization                                    | 34  |
| 4.3 Capsule Opening Studies in 2D                               | 39  |
| 4.4 Heating Evaluation  | 55  |
| 4.5 Final Insights  | 73  |
| 5 Summary and Conclusion  | 78  |

## Side Project: Deep-Tissue Viability Probing by Photothermal Cargo Delivery

|                           |   |     |
|---------------------------|---|-----|
| 6                         | Objective/Motivation                            | 80  |
| 7                         | Materials, Synthesis and Methods                | 82  |
| 7.1                       | Synthesis and Tuning of Plasmonic Nanoparticles | 82  |
| 7.2                       | Capsule Synthesis and Loading                   | 82  |
| 7.3                       | Preparation and Tuning of Cell Spheroids        | 82  |
| 7.4                       | Photothermal Capsule Opening                    | 83  |
| 7.5                       | Testing Viability using PI and Calcein          | 83  |
| 8                         | Results   | 84  |
| 8.1                       | Capsule Fine-Tuning                             | 84  |
| 8.2                       | Capsule-Pervaded Spheroids                      | 84  |
| 8.3                       | 2-Layer Spheroids                               | 85  |
| 8.4                       | Capsule-Opening at Deep Levels                  | 87  |
| 9                         | Summary/Outlook                                 | 90  |
| Appendix                  |   |     |
| 10                        | Additional Tasks/Minor Projects                 | 92  |
| 10.1                      | Viability Assessment in MHS and CTLL-2 cells    | 92  |
| 10.2                      | Etching Au-Cages from Ag-Cube Templates         | 94  |
| 11                        | Supporting Information                          | 98  |
| 11.1                      | SAR values                                      | 98  |
| 11.2                      | Particle chains                                 | 98  |
| 11.3                      | GNRs  | 99  |
| 12                        | List of Hazardous Substances                    | 100 |
| References                |   | 104 |
| Acknowledgements          |   | 111 |
| Eidesstaatliche Erklärung |   | Ω   |

## Table of Abbreviations

|                   |  |
|-------------------|--|
| AHC               | Ammonium Hydrogen Carbonate                  |
| AMF               | Alternating Magnetic Field                   |
| AuNP              | Gold Nanoparticle                            |
| CaCO <sub>3</sub> | Calcium Carbonate                            |
| CTAB              | Cetyltrimethylammonium Bromide               |
| DDA               | Dodecylamine                                 |
| DDAB              | Dimethyldidodecylammonium bromide            |
| DMEM              | Dulbecco's Modified Eagles Medium            |
| DMSA              | Dimercaptosuccinic Acid                      |
| DMSO              | Dimethyl Sulfoxide                           |
| EM                | Electromagnetic                              |
| Eppi              | Eppendorf Tube                               |
| Falcon            | Falcon Tube                                  |
| FCM               | Flow Cytometry                               |
| FITC              | Fluorescein Isothiocyanate                   |
| FM                | Ferromagnetism                               |
| HC                | Hydrogen Carbonate                           |
| HCl               | Hydrogen Chloride                            |
| HeLa cell         | Human Cervical Cancer Cell                   |
| ICP-MS            | Inductively Coupled Plasma Mass Spectrometry |
| IONP              | Iron Oxide Nanoparticle                      |
| LbL               | Layer-by-Layer                               |
| LSPR              | Localized Surface Plasmon Resonance          |
| MC                | Methyl Cellulose                             |
| MCF-7             | Human Breast Cancer Cell                     |
| MNP               | Magnetic Nanoparticle                        |
| ND                | Nitrodopamine                                |
| NIR               | Near Infrared                                |
| NP                | Nanoparticle                                 |
| PAA               | Poly(acrylic acid)                           |
| PAH               | Poly(allylamine hydrochloride)               |
| PBS               | Phosphate Buffered Saline                    |
| PEI               | Polyethylenimine                             |

|                  |   |
|------------------|---|
| PEMC             | Polyelectrolyte Multilayer Capsule              |
| PMA              | Poly(isobutylene- <i>alt</i> -maleic anhydride) |
| PNP              | Plasmonic Nanoparticle                          |
| PSS              | Poly(styrene sulfonate)                         |
| SAR              | Specific Absorption Rate                        |
| SHC              | Sodium Hydrogen Carbonate                       |
| SiO <sub>2</sub> | Silicon Dioxide                                 |
| SPM              | Superparamagnetism                              |
| SPR              | Surface Plasmon Resonance                       |
| TCAA             | Tetrachloroauric Acid (HAuCl <sub>4</sub> )     |
| THF              | Tetrahydrofuran                                 |

## Formula Symbols

|              |                                |
|--------------|--------------------------------|
| $c_x$        | Heat Capacity for Molecule $x$ |
| $d$          | Diameter                       |
| $e$          | Electron Charge                |
| $\epsilon_0$ | Dielectric Constant            |
| $E$          | Energy                         |
| $f$          | Frequency                      |
| $H$          | Magnetic Field Strength        |
| $m_e$        | Electron Mass                  |
| $m_l$        | Solvent Mass                   |
| $m_{np}$     | Nanoparticle Mass              |
| $M_w$        | Molecular Weight               |
| $N$          | Number Density of Electrons    |
| $P$          | Power                          |
| $Q$          | Generated Heat                 |
| $t$          | Time                           |
| $\Delta t$   | Time Span                      |
| $T$          | Temperature                    |
| $\Delta T$   | Temperature Difference         |
| $V$          | Volume                         |
| $\omega_p$   | Plasma Frequency               |

## Introduction

*"No amount of experimentation  
can ever prove me right; a single  
experiment can prove me wrong."  
Albert Einstein*

Medicine is amongst the best-known fields of science around the world. Recognizing, treating or curing diseases represents an indispensable part of human life. At date, cancer is the main cause of unnatural death. According to the World Health Organization, nearly 10 million people died due to this illness in 2018.<sup>[a]</sup> From 2020 on, corona took its place in the top-tier list as well. To counteract not only the aforementioned but also any other natural danger, medical research is permanently developing. One major research area focusses on the specific delivery of the molecule of interest at its desired target side. Such molecules can comprise of countless different chemical compositions and compounds, aggravating successful transport towards the destination. Several challenges arise with intracellular portage of free drugs and substances. These include for example the lack in solubility and stability as well as unwanted toxicity.<sup>11</sup> As a consequence, encapsulation of the cargo can be useful in regard of safeguarding from degrading enzymes, modification of distribution inside cells or whole organisms but most importantly to control its specific delivery.<sup>12</sup> Several encystment techniques have been reported already. They cover a multitude of carriers and materials like liposomes or nanoparticles.<sup>13</sup> Each of them provides unique advantages and disadvantages. When it comes to targeted delivery, additional delivery-specific factors come into account as well. One auspicious carrier type are multilayer capsules achieved by layer-by-layer adsorption of various molecules onto a template via electrostatic interactions.<sup>11,13-15</sup> With cavity and shell they offer two separate compartments nearly independently changeable. Numerous chemicals can act as core or shell materials for this type, offering a great versatility in size, composition, and usability. Based on the chemical composition, multifarious substances can be trapped inside. The list includes for instance proteins, peptides or even nucleic acids like DNA.<sup>16</sup> One major subject are polyelectrolyte based capsules (PEMCs), especially with sizes in the micrometer regime. Despite their massive volume, occupying several percent of the cell, their internalization happens on a natural way by an phagocytosis-related mechanism.<sup>17</sup> Nonetheless, cell type and capsule factors strongly influence time scale and effectivity of the process.<sup>16</sup> As the requirements of a delivery carrier not only include cargo protection but also final liberation at the target side it is of utmost

importance to ensure final capsule degradation. Therein lies another big advantage of PEMCs: the possibility to finely tune their release mechanism. Hence, controlled release from these carriers has been reported for a variety of trigger systems. They range from pH changes over ultrasound microwave irradiation to photothermal heating.<sup>12,15,16,18,19</sup> Particularly the latter method has gained major interest due to high controllability and efficiency. Cargo release under NIR-irradiation has already reached a reliable state for several *in vitro* approaches.<sup>12</sup> However, this technique lacks operational capability for *in vivo* experiments as biological tissue shows strong light absorption and scattering.<sup>12</sup> As a consequence, opening at deeper tissue levels remains challenging. Meanwhile, a slight modification of the system helps overcome the absorption issue. By replacing the plasmonic nanoparticles in the capsule shell, which are responsible for the capsule opening via interaction with the laser, with magnetic NPs (MNPs), the external trigger source can be changed towards an alternating magnetic field (AMF). As AMFs are operated at completely different frequencies absorption issues are minimized.<sup>8,12,15,16,18</sup> At the same time, the major benefit of local heating in the shell remains. As temperature peaks only occur within a few nanometers around the particles, cell health is secured.<sup>15</sup> Conveniently, MNPs combine a disruptive heating effect with a non-heating equivalent in form of vibrations under field irradiation.<sup>12</sup> Several materials qualify for MNP formation, but it stays mandatory to use particles with outstanding heating ability. The most promising substance is iron oxide, which shows protruding biocompatibility and excellent magnetic properties.<sup>20</sup> Several synthesis strategies<sup>21-27</sup> have been established with focus on superlative Specific Absorption Rate (SAR)<sup>25</sup>. This value displays the amount of heat produced per weight. And the opportunity to release cargo from such magneto-responsive systems based on iron oxide has already been proven.<sup>12</sup> The *in vitro* or *in vivo* outcome, however, lacks examination.

This thesis majorly tackles this actuality. For that, it is divided into two projects. The first part of this work aims exactly at answering the uncertainty of magnetically induced opening in living media. It includes a step-by-step approach from nanoparticle preparation over capsule functionalization towards opening trials in cells and the elaboration of occurring problems. The second part focusses on improvements on laser-induced opening at deeper tissue level and consists of spheroid preparation techniques and laser-irradiation tuning.

## 1 Theory/State-of-the-Art

*“Scientific theory is a contrived foothold in the chaos of living phenomena.”*

*Wilhelm Reich*

### 1.1 Magnetic Nanoparticles

The term ‘magnetic nanoparticle’ (MNP) summarizes matter with at least one dimension in the submicrometer regime (typically 1-100 nm)<sup>28</sup> that simultaneously shows magnetic properties. Similar to other nanoparticles, MNPs can be synthesized from several substances. Especially important are metals and their oxides.<sup>29</sup> The particle size thereby complies with the entities of application (e.g. cells, viruses or genes)<sup>28</sup>, which strongly improves the interplay. Moreover, they offer beneficial characteristics in comparison to the bulk material such as enormous surface-to-volume ratio, strong reactivity and enhanced tissular diffusion.<sup>29-32</sup> An additional feature of MNPs relies in their ability to interact with external magnetic fields due to their magnetism.<sup>28,31</sup> This opens up two big opportunities: 1) the MNPs can be directed to a target site and 2) energy can be transferred from field to particle.<sup>28,33</sup> The latter mechanism plays a major role if an alternating magnetic field (AMF) is applied. Each time the field changes its direction the magnetization inside the particles rotates and completes a cycle called hysteresis loop. This process delivers heat amounts proportional to the loop area.<sup>28</sup> The magnetic properties and the loop are massively affected by particle size, morphology and composition.<sup>28,33</sup> At really small diameters (< 20 nm) the interaction with magnetic fields often significantly changes. At these sizes superparamagnetism can appear under standard conditions. In this condition, magnetic moments only show parallel orientation inside an external field but disorientate otherwise, making the loop disappears (*cf.* figure 1). In this specific case, relaxation mechanisms come into validity for heat production.<sup>28,34-36</sup> Such behavior still allows for high saturation magnetization but the residual magnetic forces between particles completely disappear under absence of external fields, which represents a big advantage.<sup>28,37,38</sup>

The crucial factor for the adjustment of intrinsic NP-parameters comes from the synthesis. Small changes in execution can have significant consequences on the final MNPs. Most importantly, nucleation and growth should be isolated to achieve monodisperse batches. Suitable ligands need to be included to avoid agglomeration or aggregation, which are otherwise caused by magnetic interaction and the tendency to reduce surface energy.<sup>37,38</sup> Several synthesis

approaches, fitting the aforementioned requirements in different extent, have been processed. Examples are laser pyrolysis, microemulsion synthesis, coprecipitation and thermal decomposition.<sup>37</sup> All these methods deliver stable but hydrophobic particles due to the ligands on the surface, with the latter typically being long carbon-chains. To enable their biocompatibility for use in biomedicine, a change in surface coating is required towards a hydrophilic substitute. This can be achieved by replacement of or addition to the original capping agent.<sup>30,37</sup> The corresponding occurrence also allows for functionalization of the surface for interaction with the target system or to reduce toxicity.<sup>29,30</sup>

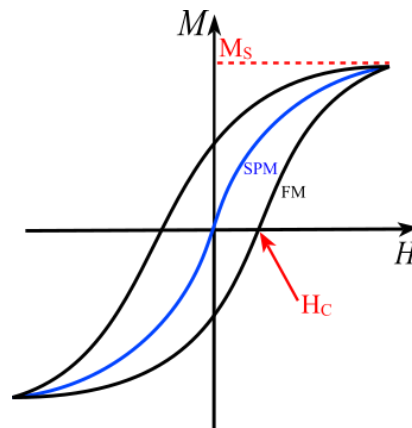
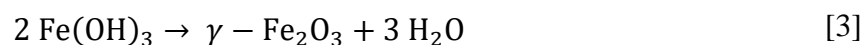
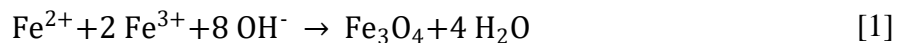


**Figure 1:** **Hysteresis Loop showing magnetic responses.** For a ferromagnetic material (FM, black) the magnetization runs through a cycle once it has reached its saturation magnetization ( $M_s$ ) and can only be fully demagnetized if a specific coercive field ( $H_c$ ) is applied. On the contrary, superparamagnetic material (SPM, blue) doesn't show a loop and magnetization disappears without a field. Modified from [28], [34] and [36].

In accordance with the special properties, MNPs have led to versatile new biomedical applications. Those range from detection and targeting to delivery and cancer treatment.<sup>28-30,37,39</sup> So far, it has for instance been achieved to bind magnetic nanoparticles onto cells.<sup>28,39-41</sup> In molecular imaging, MNPs are already used as contrast agents with high sensitivity due to reduced relaxation times.<sup>28,39</sup> Advances in cancer treatment include for example therapies based on hyperthermia.<sup>28,39,42</sup> And for drug delivery they can significantly enhance the specificity by carrying the cargo to the treated area, which benefits the treatment in terms of confining intended and minimizing side-effects.<sup>28,39</sup> Despite all the promising features it is crucial to ensure biocompatibility of the particles, as they could otherwise harm the tissue during later application. Many materials were tested regarding toxicity. However, only a few (2010: 12)<sup>29</sup> made it through the approval process. Complete examination and elimination of toxicity are complicated as the behavior is based on multiple factors (e.g. dose, size, solubility).<sup>29</sup>

### 1.1.1 Iron Oxide Nanoparticles

To qualify for biomedical use, a material needs to combine outstanding experimental properties with minimal toxicity and brilliant biocompatibility. For MNPs, the most important experimental parameter is the intrinsic magnetism plus their interaction with external fields.<sup>37</sup> One of the most prominent and a very promising compound for the preparation of such particles is iron oxide.<sup>20,22,31,38</sup> Especially the brilliant magnetic behavior, but also its biocompatibility, the low cost production and its good stability have gained it a lot of attraction for bioapplications.<sup>20,22,33</sup> Focusing just on the magnetism, pure iron would be much better due to a significantly higher magnetization. But it cannot be used due to nearly immediate oxidization. Iron oxide appears in a multitude of variants with differing stability. The important forms include hematite ( $\alpha\text{-Fe}_2\text{O}_3$ ) and the biocompatible<sup>38</sup> constitutions maghemite ( $\gamma\text{-Fe}_2\text{O}_3$ ) and magnetite ( $\text{Fe}_3\text{O}_4$ , more detailed:  $\text{Fe}^{2+}(\text{Fe}^{3+})_2\text{O}_4$ ).<sup>43</sup> Sufficient performance of the particles strongly belongs to their size and composition. Similarly important are the magnetic properties like (high) magnetic susceptibility, (low) Curie temperature and superparamagnetism.<sup>31,38</sup> Therefore, synthesis fine-tuning plays a major role and can be extremely useful to manipulate the particles (e.g. size, crystallinity) for a desired application.<sup>43,44</sup> An easy, fast and cheap synthesis strategy is called coprecipitation and describes the mixture of  $\text{Fe}^{2+}$ - and  $\text{Fe}^{3+}$ -ions under basic conditions to form magnetite (*cf.* formula 1) or maghemite (*cf.* formulas 1-3).<sup>20,37,38</sup>



The resulting particles are, however, usually broadly distributed in size and their crystallinity is low.<sup>20</sup> Nevertheless, some size and shape modifications can be achieved by changing the precursor iron salts, the ion ratio, reaction temperature and/or other parameters.<sup>20,31</sup> For the preparation of very narrowly distributed iron oxide nanoparticles (IONPs) other synthesis principles are more promising. Such routes generally require either high temperature or high pressure which makes them more complicated. In a hydrothermal synthesis the precursors are for instance mixed inside an airtight reservoir and heated above the boiling point at high vapor pressure.<sup>20,31</sup> Another prominent strategy is called thermal decomposition because it is based

on the decay of the precursors at high temperatures (*i.e.*  $T \gg 100 \text{ }^\circ\text{C}$ ).<sup>20,31</sup> Those are mixed with or injected into a solution of surfactants. Subsequent heating initiates nucleation and induces the formation of particles under stabilization by the ligands.<sup>31</sup> The compounds used for passivation are usually organic (e.g. oleic acid, oleylamine) and improve not only their stability by influencing the repulsion between individual MNPs but also their reactivity by adding new reactive groups.<sup>31,37</sup> Reaction time, temperature, solvents and precursor type are some determining factors for the resulting IONPs. Thermal decomposition can deliver high quality particles directly from the precursors and does not require a size-selection. But the used precursor chemicals are mostly toxic and the resulting particles are typically not water soluble.<sup>20,31,37</sup>

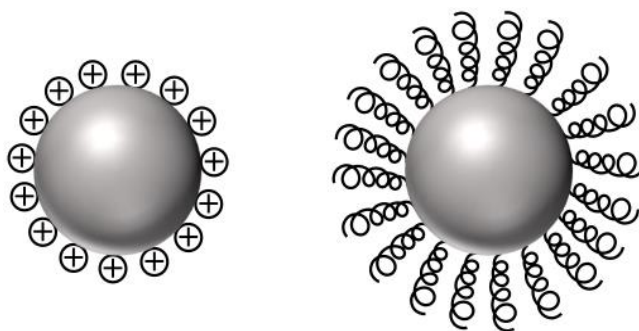


**Figure 2:** **Particle Stabilization Methods.** Single NPs can be stabilized by coating the surface with compounds influencing electrostatic (left) or steric (right) repulsion. Both types can help avoiding agglomeration and aggregation. Modified from [43].

To transfer the particles into aqueous solution - as necessary for bioapplication -, a change in surface coating is required.<sup>31,37</sup> Several sufficient hydrophilic surfactants and transfer methods are reported by now. Specific choice depends on the individual approach.<sup>31,37,45,46</sup> All in all, iron oxide is already well understood and has been used in a multitude of applications like molecular imaging, drug delivery and hyperthermia.<sup>43,47</sup>

## 1.2 Plasmonic Nanoparticles

Plasmonic nanoparticles (PNPs) represent structures with at least one dimension in the nanometer range that show plasmonic behavior. They represent emerging research objects due to outstanding properties and are used in multiple applications already. Some examples are biosensing, detection and targeted delivery.<sup>48</sup> At present date, PNPs can be synthesized with brilliant control of size, shape and composition. Most commonly, the particles are the final result of reduced metal precursors when high amounts of surfactant are around.<sup>49</sup>

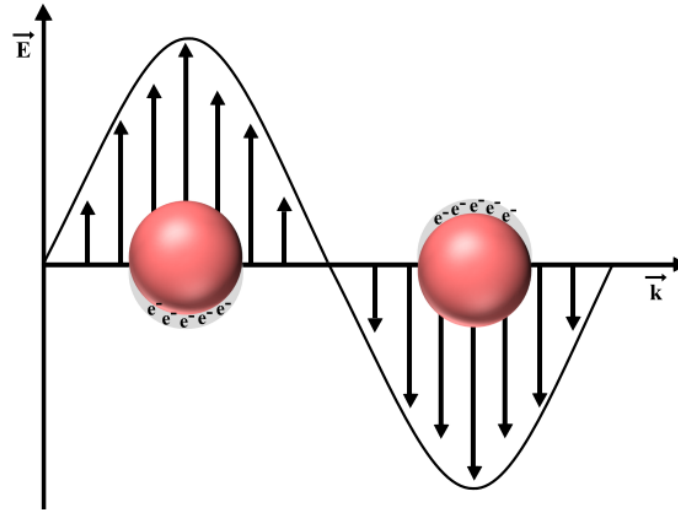


**Figure 3:** **Localized Surface Plasmon Resonance.** If irradiated electromagnetically, free electrons in the particle conduction band are forced to oscillate collectively with the incoming light-wave. Confined to a single particle, this leads to formation of a dipole due to charge separation. Modified from [49].

If plasmonic materials are irradiated by for instance a laser, free electrons located in particle conduction bands are forced to oscillate coherently with the electromagnetic wave due to its alternating electric field. Under specific conditions, this leads to a resonance case. This principle is called surface plasmon resonance (SPR).<sup>49-53</sup> The affiliated plasma frequency – for a bulk system with infinite size - can be calculated by means of the following equation where  $N$  represents the number density of electrons,  $\epsilon_0$  the dielectric constant in vacuum and  $m_e$  and  $e$  mass and electric charge of a single electron.<sup>49</sup>

$$\omega_p = \sqrt{\frac{Ne^2}{\epsilon_0 m_e}} \quad [4]$$

Actual systems are, however, of limited dimensions, which causes a change in  $\omega_p$ . At very low scale, SPR undergoes localization. For nanoparticles, whose size falls significantly below the incoming wavelength, the dislocated electrons carry a negative charge to one end of the NP while positive charges remain on the other end. This represents the formation of a dipole switching direction with the light-wave. (LSPR, *cf.* figure 3).<sup>52,53</sup> Resulting from that is a frequency shift towards the near-infrared or visible spectrum. Shape and composition strongly influence the outcome of the LSPR, but it also depends on several other factors including the used element.<sup>52</sup>

Resulting from the dipole oscillation, light absorption and scattering are significantly increased. During relaxation, the absorbed light can then be transformed into different light or heat.<sup>50-52,54</sup> One possibility to utilize this heating phenomenon lies in the desired destruction of carriers to deliver their cargo. In this way, polymer capsules have been widely used to carry and deliver materials under laser irradiation of the included PNPs.<sup>55,56</sup>

### 1.2.1 Gold Nanoparticles

One of the most prominent materials used as core material for PNP formation is gold. Gold has been known all over the world for centuries, mainly for its use in jewelry. In recent years, significant property changes at really low size ranges have aroused a lot of interest. While corresponding color changes away from the striking, shiny yellow-gold have already been utilized for decades, other effects of size reduction include the emerging catalytic ability and localized plasmon resonance.<sup>57</sup> As a consequence, gold-based nanoparticles (AuNPs) are important research objects nowadays. They can mostly be synthesized fast and easy with good quality and yield.<sup>58,59</sup> Usually, gold precursor salts are reduced to form ions, which subsequently form nuclei. Those then grow further to form NPs. A reducing agent ensures the reduction, surfactants are added during preparation to avoid aggregation.<sup>58-60</sup> The final size outcome significantly depends on the ratio between gold ions and other involved substances.<sup>60</sup> In addition to size, shape has a huge impact on the particle properties as well. Prominently used shapes are spheres and rods.<sup>61</sup> A successful and common way to achieve spherical particles is based on the reduction of tetrachloroauric acid (TCAA,  $\text{HAuCl}_4$ ) (*i.e.* improved citrate method evolved by Turkevich *et al.*).<sup>48</sup> Rods require a more sophisticated two-step synthesis including the use of cetyltrimethylammonium bromide (CTAB). At first, seeds need to be prepared which are added to a growth solution subsequently. However, the more difficult conditions go ahead with a finely tunable plasmon resonance based on size and/or aspect ratio.<sup>48</sup> Multiple other shapes including cages, stars and shells have also been observed and tested. Modifications of size and shape consequently allow for an adjustment towards the final use.<sup>48</sup> Another important factor results from the surface: manipulation and functionalization of the surface represent a decisive opportunity to influence the particle behavior. Changes in the coating can impinge stability, biodegradation/-compatibility, biological visibility and targeting.<sup>57</sup> Usually, charged surfactants bind to the NPs during synthesis, which secures stability by electrostatic forces.<sup>59</sup> Subsequent ligand exchange can then be acquired to change the compartment, to transfer the particles into different solvents or for several other purposes.<sup>59</sup>

Based on narrowly-adjustable size distributions and tunable properties, AuNPs are used in several application fields already. Some mentionable ones are electronics, sensing, diagnostics and therapeutics.<sup>57,60</sup> Therapeutics also enclose hyperthermia and drug delivery<sup>57</sup>, which play a major role in this elaboration.

### 1.3 Magnetothermal Heating

As indicated in chapter 1.1, MNPs strongly tend to interact with external magnetic fields. During this process an energy transfer from field to particle can take place, which causes the production of heat.<sup>62</sup> This process is known as magnetothermal heating. Especially magnetic fields alternating with radiofrequency enhance the heating, forcing the magnetic moments inside the NPs to constantly flip against their energy barrier. These moments afterwards surpass relaxation while going back to the original state. For small particles, being at least as small as one magnetic domain, Néel and Brownian relaxation are the predominant mechanisms. If for example the whole particle rotates, heat is delivered through friction and shear stress between the surface and the surrounding medium (*i.e.* Brownian relaxation). If, however, only the inner moments change direction, the energy is consumed by rearrangement of atomic dipole moments. Both mechanisms are strongly connected. Size and anisotropy of the particles as well as the surrounding medium strongly influence which mechanism outweighs the other. However, Néel is to some extent reported to show more impact for smaller particles and in highly viscous medium whereas Brown prevails for bigger particles and low viscosity.<sup>62,63</sup>

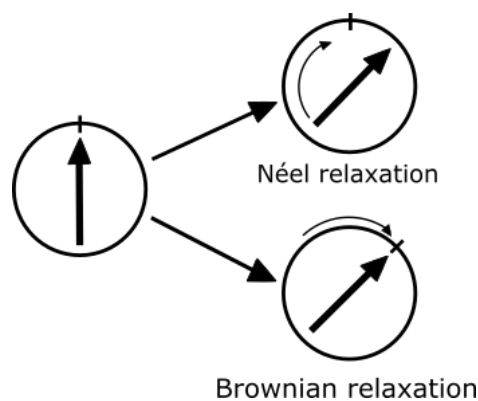


**Figure 4:** Néel and Brownian relaxation. Based on an external alternating magnetic field the magnetic moments of MNPs tend to align their direction with the field. This can either be only the magnetic moments inside (Néel) or include the movement of the whole particles (Brownian). Modified from [63].

Each mechanism has a specific relaxation time  $\tau$  (*cf.* formulas 5.1 and 5.2) determining the duration of spin reversal. While Néel relaxation is majorly affected by the magnetic anisotropy (K) and the particle volume (V), major impact on the Brownian time arises from fluid viscosity ( $\eta$ ) and hydrodynamic volume ( $V_H$ ).<sup>62,63</sup> Manipulation of the particle properties, therefore, not always impacts both mechanisms.<sup>63</sup>

$$\tau_{Brownian} = \frac{3 \eta V_H}{k_B T} \quad [5.1]$$

$$\tau_{Néel} = \tau_0 \exp\left(\frac{KV}{k_B T}\right) \quad [5.2]$$

$$\frac{1}{\tau_{effective}} = \frac{1}{\tau_{Néel}} + \frac{1}{\tau_{Brownian}} \quad [5.3]$$

The values  $k_B$  and  $T$  in the formulas correspond to the Boltzmann constant and the temperature. Interplay of both processes, which becomes especially important for superparamagnetic NPs, regulates the actual heating. It can be evaluated by means of the effective relaxation time  $\tau_{effective}$  (*cf.* formula 5.3).<sup>62,63</sup> The resulting power output (P) from the system is directly connected to this value. The correlation is given by formula 6, in which  $f$  represents the applied frequency.

$$P \sim \frac{2\pi f \times \tau_{effective}}{1 + (2\pi f \times \tau_{effective})^2} \quad [6]$$

For bigger particles (*i.e.* more than one domain) another mechanism named hysteresis loss, which describes the process of domain wall shifting, takes place as well.<sup>12,27,36,63</sup> Independent from their size, all nanoparticles are additionally stimulated to vibrate.<sup>12,64</sup> To allow for comparison of the heating behavior between different particles the specific absorption rate (SAR) was developed.<sup>65</sup> It connects the resulting power to the mass of producing material and can be calculated using the following equation [7.1].

$$SAR = \frac{P}{m_{np}} = \frac{1}{m_{np}} \frac{Q}{\Delta t} = \frac{(m_{np}c_{np} + m_l c_l) \Delta T}{m_{np} \Delta t} \quad [7.1]$$

$$SAR = \text{area of hysteresis loop} \cdot \text{frequency}. \quad [7.2]$$

Here  $P$  represents the power,  $m_{\text{np}}$  the nanoparticle mass,  $Q$  the generated heat in a time period  $\Delta t$ ,  $c_{\text{np}}$  and  $c_l$  the specific heat capacities of the nanoparticles and the liquid and  $\Delta T$  the temperature increase. In a typical measurement, the temperature course is recorded over time and, subsequently, a specific time span is picked out. If all other parameters are known, the temperature increase during this time span allows for direct calculation of the SAR.<sup>27</sup> Equation 7.2 describes the calculation for particles showing hysteresis loss by multiplication of loop area with the applied frequency. Unfortunately, it connotes that a steady increase in frequency would cause the SAR to reach unlimitedly high values. In reality, such values cannot be used in biomedical applications. On the contrary to magnetic fields at moderate frequency and field strength, these extreme AMFs would induce harmful eddy currents inside the body. As a consequence, a safety limit has been set by Atkinson and Brezovich.<sup>62</sup> The product of field strength ( $H$ ) and frequency ( $f$ ) is not allowed to overcome  $4.85 \times 10^8 \text{ Am}^{-1}\text{s}^{-1}$  for medical use.<sup>62,63</sup> Research, however, is also done above the limit; especially in case of proof-of-principle tests. The most prominent field is alternating at a frequency of  $f = 300 \text{ kHz}$  with field strength of  $H = 24 \text{ kA/m}$ .<sup>12</sup>

#### 1.4 Photothermal Heating

Photothermal heating describes a local increase in temperature under irradiation by light. Typically, monochromatic light - as present in a laser beam - is focused onto an object which undergoes excitation during light absorption. Multiple materials including dyes and metals can act as the absorber.<sup>61</sup> Metal nanoparticles are, however, favored due to mobile free-electrons in the conduction band forming LSPR. Light absorption is greatly enhanced at the corresponding resonance frequency (*cf.* chapter 1.2).<sup>66-68</sup> The most prominent photothermal heaters are gold nanoparticles as they are showing outstanding absorption (*i.e.* 1,000 times higher than dyes)<sup>50</sup> and heating efficiency.<sup>50,51,54</sup> Modern approaches utilize ultrashort laser pulses to illuminate the sample for very short durations.<sup>68</sup> Once the light interacts with these particles, excited oscillating electrons result. After a very short time period these plasmons decay again, leading to dispensation of excess energy. This process can occur either radiative by emission of photons or non-radiative.<sup>66</sup> In the latter case, the energy is transformed into heat.<sup>67</sup> This results from rapid energy transfer to the NP-lattice (phonons) by means of electron-electron and subsequent electron-phonon scattering.<sup>67,68</sup> During final phonon-phonon scattering or thermal diffusion, the heat is then transported from the lattice into the surrounding area.<sup>50-52,54,68</sup> Efficiency of each step, thereby, relies on multiple parameters of absorber and environment.

For maximum yield, the incoming laser light should also be minimally absorbed by the surrounding medium. Tuning the particle properties enables manipulation of the required laser light wavelength by changing the LSPR region of the absorber.<sup>50,61,69</sup> This allows for a use of frequency ranges with reduced tissue interaction. Near-infrared is the most common window for biomedical applications as it represents a range of reduced absorption, which permits deeper penetration and maximal heat conversion.<sup>67</sup> These days, enormous amounts of heat are producible at low laser intensities by right choice of the heat mediators. In this way, the laser irradiation is confined to the PNPs and a small tissue volume around, minimizing harm and side effects.<sup>67</sup>

## 1.5 Polyelectrolyte Capsules

One of the crucial factors during therapeutic application is the final efficiency at the target site. Medical drugs, similar to every other exogenous substance, meet several mechanisms with massive influence on effectivity (e.g. denaturation or degradation) once they enter the biosystem.<sup>16</sup> Protection of the drug and delivery towards its desired location can hinder or even minimize such mitigation.<sup>13,15,70</sup> Accordingly, a great number of transport-systems has been evolved. They strongly differ in properties like size or material, which spreads their use to a variety of applications. Some examples are nanoparticles, carbon nanotubes and liposomes.<sup>13</sup> In most cases, a specific carrier kind is limited regarding its extent of includable therapeutics and targetable areas. Hence, an ideal carrier would be very stable, able to transport the whole spectrum of cargo types towards every target location and set it free if necessary.<sup>8,13,15,16</sup> Polyelectrolyte multilayer capsules (PEMCs) with sizes from around 0.1  $\mu\text{m}$  to 10  $\mu\text{m}$  represent a promising carrier class for this field.<sup>13,71</sup> PEMCs are hollow capsules (*i.e.* cavity area) surrounded by a shell consisting of several polymer layers. They enable encapsulation of a wide range of cargos.<sup>13,72</sup> Possible cargo substances include inter alia proteins, vaccines and nucleic acids. However, chemical drugs represent the most prominent type.<sup>18,70</sup> Preparation of PEMCs is achieved by Layer-by-Layer (LbL) adsorption of oppositely charged materials onto a core substrate. Fortunately, LbL works on an immense number of substrates and isn't linked to a specific surface chemistry.<sup>70</sup> The core material can be the cargo itself or a removable placeholder which defines the size.<sup>13,70,72</sup> The template selection strongly impacts the final capsule properties. Both organic and inorganic materials can serve as the template. Some common examples are silicon dioxide (organic,  $\text{SiO}_2$ ) and calcium carbonate (inorganic,  $\text{CaCO}_3$ ). The shell, in contrast to the cavity, permanently interacts with the medium around and biases for instance the biocompatibility and degradability.

Correspondingly, it requires a fine tuning as well.<sup>13,73</sup> The list of shell materials is long and versatile. Some are biodegradable others are almost completely stable. Important examples for degradable polymers are alginate, chitosan and dextran whereas poly(styrene sulfonate) (PSS), poly(allylamine hydrochloride) (PAH), polyethyleneimine (PEI) and polyacrylic acid (PAA) are the most prominent non-degradable ones.<sup>12,13,70,73-75</sup> Choosing the best fitting material plays a major role to conduct the final outcome during application.<sup>13</sup>

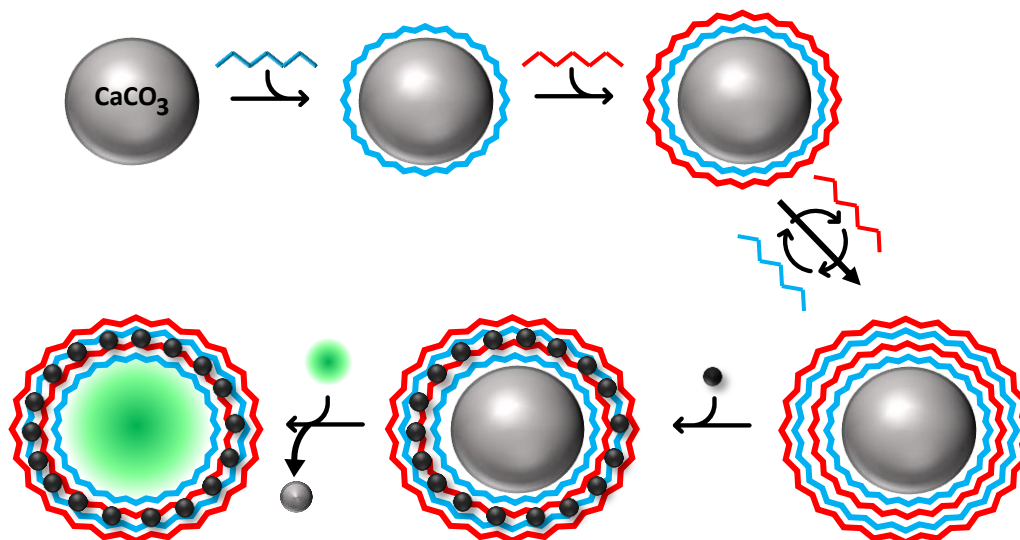


**Figure 5:** **Capsule preparation via LbL-assembly and postloading.** By repeatedly attaching polyelectrolytes (blue + red) of opposite charge onto a template (here:  $\text{CaCO}_3$ , grey) a shell is produced. This shell can be functionalized by adding nanoparticles (black) in between. After attachment of all layers, the core can be removed, leaving hollow carriers. Finally, these can be loaded with a cargo (green) which requires a subsequent change in permeability of the shell to cage it. Such changes are for example achieved by heat shrinkage. Modified from [13].

Three different loading strategies for the capsules are feasible. The cargo can either be preloaded into the core material, added into the shell or postloaded after core dissolution.<sup>16,18,70</sup> For preloading, the core material on the one hand needs to be sufficient to cage the cargo and on the other hand should be easily removable in a way which is harmless for the freight.<sup>16,18,70</sup>  $\text{CaCO}_3$  constitutes such a material which works brilliant due to high porosity and simple degradation.<sup>16</sup> The incorporation into the polyelectrolyte is accomplished by including a cargo layer into the shell or conjugating it thereto.<sup>70</sup> Finally, postloading requires a change in shell permeability to allow for diffusion through the layers into the core during loading but subsequent inclusion.<sup>16,18,70</sup> Capsules that are not degraded automatically by intracellular mechanism (e.g. enzymatic or hydrolytic degradation)<sup>70</sup> need a specific opening mechanism or

trigger. One way to functionalize the system for a controlled release is the incorporation of (charged) nanoparticles into the shell. This process adds new qualities (e.g. magnetic, photothermal or optical) to the capsules.<sup>13</sup> Thus, gold nanoparticles were implemented to enable interaction with near infrared (NIR) laser light. By transforming the laser light into heat the capsules shell is destabilized and the cargo diffusion into the surrounding region restored. In this way, controlled and precisely targeted cargo release is achievable.<sup>10,13,18,55,73,74</sup> However, NIR-lasers cannot penetrate infinitely far into biological tissue due to either absorption or the requirement of high intensity short pulses which clearly hampers *in vivo* application.<sup>8</sup> In contrast, magnetic fields are not attenuated by human tissue and do not cause damage to it. So if the gold nanoparticles are replaced by magnetic substitutes, which are able to interact with the field, the heat production and the associated release under irradiation is restorable at deep tissue level.<sup>8,12</sup> This opens up a variety of new approaches.

## 1.6 Cancer Cells as Model Systems

Cells are the smallest living unit in any creature. Determination of cell behavior and health, therefore, is of utmost importance to gain knowledge about the overall condition of the organism they are part of. In this way, the influence of external factors on the internal constitution and mechanics can be analyzed. Moreover, specific properties of cancerous cells can be examined.<sup>76,77</sup> It has already been gained a lot of information about the cellular level, but some processes and properties remain undiscovered or unencrypted. Cell-cell communication and the bystander effect represent two examples for occurrences not completely unwrapped.<sup>78</sup> To allow for a more detailed look into the intrinsic biology and mechanisms, different cell model systems are usable. Although cultured cancer cells are not completely identical to healthy body cells many similarities are given, making them an excellent mock-up.<sup>79,80</sup> As a consequence, several human cell lines (*i.e.* in 2010: 1200)<sup>79</sup> were cultured and used since their discovery.<sup>79,80</sup> 2D-cell culture is the most common tool. It usually describes the attachment and growth of cell single-layers onto the flat surfaces of flasks or dishes at human body temperature (37 °C).<sup>76,77,81</sup> Since its development, multiple improvements were established. Those include for example growth area, feeding difficulties and bacteria protection.<sup>81</sup> Nowadays, this method is simple, low-cost and leads to homogeneously grown cell layers.<sup>77</sup> However, it strongly differs from a real *in vivo* situation in several points: cell shapes are not controllable plus morphology and polarity change due to culturing.<sup>76,77</sup> Cells are also not always in close contact to neighboring cells. As a consequence, the cell-to-cell and cell-to-exterior communication is not reestablished, which affects multiple cell parameters (*i.e.*

amongst others differentiation, proliferation, health) and responses (*e.g.* apoptosis).<sup>77</sup> Nevertheless, 2D-cell systems are an excellent environment for monitoring capsule-based drug delivery, which - in terms of observation - only pertains the individual cell. For examination, the carriers at first need to enter the system by surpassing the cell membrane. Naturally happening uptake is strongly connected to size and other parameters and can be tuned by capsule modification.<sup>15,17,70,82,83</sup> The corresponding internalization process is still investigated. However, it has been observed that cells form a phagocytic cup around micrometer-sized capsules which may suggest phagocytosis.<sup>17,83</sup> If fully surrounded by the membrane, ingestion into the cell interior takes place. Capsules were observed to finally end up in acidic compartments.<sup>17,83</sup> It has also been determined that no infiltration into the nucleus is possible.<sup>17</sup> Once located inside lysosomes, being an example for acidic compartments,<sup>84</sup> the release process becomes challenging and requires lysosomal escape.<sup>70</sup> Without disruption of the surrounding membrane-network, the cargo remains confined to the lysosome and never enters the cytosol. Moreover, long-time presence in such an acidic environment might harm the capsule and the cargo. Ideal trigger-systems induce capsule opening and lysosomal escape simultaneously, allowing for direct cargo movement from carrier to cytosol.<sup>78</sup>

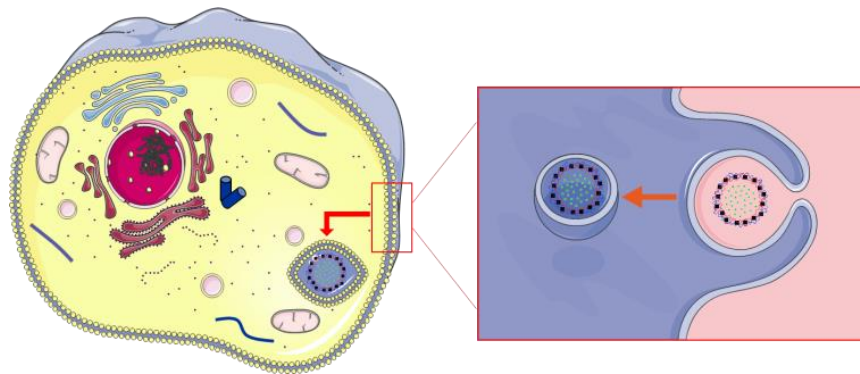


**Figure 6:** **Capsule uptake-principle into cells.** Uptake of nearby capsules starts with a formation of a phagocytic cup around them. After full engulfment of the membrane around the carriers internalization is completed and the capsules are located inside the cytosol while surrounded by a bilayered shell.<sup>[c]</sup>

3D-models offer higher comparability and simulate the outcome inside living organisms in a more precise way. By including the third dimension, cell-to-cell interaction is restored, which causes several similarities to the *in vivo* situation to reappear. Moreover, cell polarity and morphology are preserved from changes. The technique is especially important in cancer research. Three-dimensional tumor spheroids represent an ideal research object, which offers multiple concords to their body counterparts.

If attachment of clumped cells to a surface is avoided, their tendency to aggregate increases and spheroids are formed.<sup>85</sup> Due to the multi-layer growth the constant supply of nutrients, oxygen and other vital substances, as it is given for 2D models, is unbalanced in deeper parts which matches the necrotic area inside body tumors.<sup>76,77,81</sup> Nevertheless, it remains hard to gain information about the processes at deeper levels without influencing the whole system. Staining of single inner cells or the observation of communication between cells in form of transport or signaling is still under research.<sup>86,87</sup> Previously introduced functionalized polymer capsules constitute a promising tool to observe and analyze the events happening inside the three-dimensional cell cluster. They can be loaded with multiple substances and materials, are stable enough to reach the inner part of the spheroids without losing the cargo and can be remotely opened under specific circumstances, which allows for a release of cargo at specific sites and time points.<sup>19,88</sup> In this way, cell impermeable substances can be transported into the center part of 3D cell models without harming the cells and be delivered controllably, which can give rise to time resolution and course of local processes. One interesting field for controlled delivery are for instance viability tests. Especially in biomedical applications it is mandatory to evaluate biocompatibility and the influence of substances and molecules on the touched cells. Under use of NP-functionalized polymer capsules, the molecule acting as viability tester could be delivered into the cell and the outcome could be directly observed.<sup>88</sup>

## 1.7 Viability assays

Already in 1538, when Paracelsus published his world-famous quote telling that everything is toxic based on its dose, it was thought about the effect of matter on health.<sup>89</sup> For evaluation of the usability of experiments, substances or other parameters in biomedical applications it is mandatory to examine their biological compatibility. One corresponding strategy bears on viability assays. Multiple different parameters can be utilized to value the cell functionality while fluorescence allows for direct observation.<sup>90</sup> Such assays usually rely on the ability of healthy cells to convert molecules into detectable products. A damaged or dead cell eventually loses the desired skill which allows for easy recognition due to missing fluorescence signal. Common examples for molecules used as reducible agents are calcein-AM, tetrazolium compounds, resazurin, glycyphenylalanin-aminofluorocoumarin (GF-AFC) and propidium iodide (PI).<sup>90,91</sup> Two possible approaches are most suitable to analyze the viability: distinction between different colors or observation of presence or absence of one specific signal to distinguish between live and dead cells. One example for a single signal is the cell-permeable resazurin. Intact cells act as reducers to form a pink-fluorescent resorufin. This process requires

the presence of NADH as the reducing agent which is not produced in dead cells. The resulting output signal is proportional to the number of healthy cells. However, several factors such as incubation time and cell density need to be finely tuned for each cell line. Moreover, cytotoxic side effects have been observed during exposure for several hours.<sup>90</sup> For evaluation based on two signals, propidium iodide and calcein-AM can be utilized together. Calcein-AM can enter cells through their membrane which leads to a conversion into the green-fluorescent, cell-impermeable calcein by esterase. Dead cells are missing on the esterase and cannot form the fluorescent version. Moreover, calcein can easily diffuse out again if the membrane isn't intact anymore. Big advantages of calcein-AM are great fluorescence intensity and low leaching.<sup>92</sup> On the contrary to calcein-AM, propidium iodide is cell-impermeable and can only enter cells with damaged membrane. As soon as PI enters the cells, it binds to RNA and DNA and marks the cell in a red color. Unfortunately, alive cells with slightly damaged membrane are also marked (false positive) whereas dead cells with intact membrane are not entered and remain unmarked (false negative). In combination, a direct assessment of cell health is possible: healthy cells appear green whereas dead cells show red fluorescence.<sup>91,92</sup> It is also possible to use calcein, the fluorescent form, directly. This approach requires its delivery into intact cells which can be acquired by use of carriers such as the herein examined polyelectrolyte capsules.

### 1.8 Two-Photon Microscopy

Detailed observation of the entity of interest is a crucial factor to analyze and understand the processes occurring inside. Depending on the size, type and character of the specific environment, choice of the correct set-up is an important ingredient. Among the field of microscopes, laser scanning microscopy (LSM) represents one standing-out system for observation of biological samples.<sup>93,94</sup> In such a device, the final image of the probe is achieved by assembly of multiple signals attained from individual sample spots. Those signals arise from stepwise scanning of a focused laser-beam across the specimen and include information about transmission, reflection and emission.<sup>94-96</sup> In terms of the previous parameters, an LSM strongly differs from conventional microscopes, where direct imaging of the probe is used.<sup>95</sup> Modern systems, furthermore, offer *optical sectioning* as an additional improvement, which describes the reduction of background signal and blur from area outside the focus. This outcome is achieved by insertion of a spatial filter.<sup>97,98</sup> Such microscopes are usually called Confocal-LSMs (CLSMs). This principle is especially important for the localized detection of fluorescence. Fluorescence describes the process of photon emission shortly after excitation of an electron due to absorption of energy. The incoming energy typically comes from a photon

hitting the electron-containing molecule and must be high enough to induce excitation of the negative charge-carrier from a ground to an excited state.<sup>93</sup> The energy carried by a photon is inversely proportional to its wavelength  $\lambda$  and can be calculated by the following formula, in which  $h$  represents the Planck constant and  $c$  the speed of light in vacuum:<sup>93</sup>

$$E = h \times \frac{c}{\lambda} \quad [8]$$

As this energy has a wide range of possible values, excited electrons might end up at higher-energetic vibrational levels inside the excited state. Once the system recombines to its initial state, the excess energy is emitted in form of another photon. For this process to happen, electrons need to undergo - mainly non-radiative – energetic relaxation or conversion to reach the lowest vibrational level beforehand. Consequently, emitted photons are usually lower-energetic than their absorbed counterparts, which is also known as the *Stokes shift*.<sup>93</sup> Correspondingly, incoming and outgoing light are separable due to different color and longer wavelength for the outgoing light.

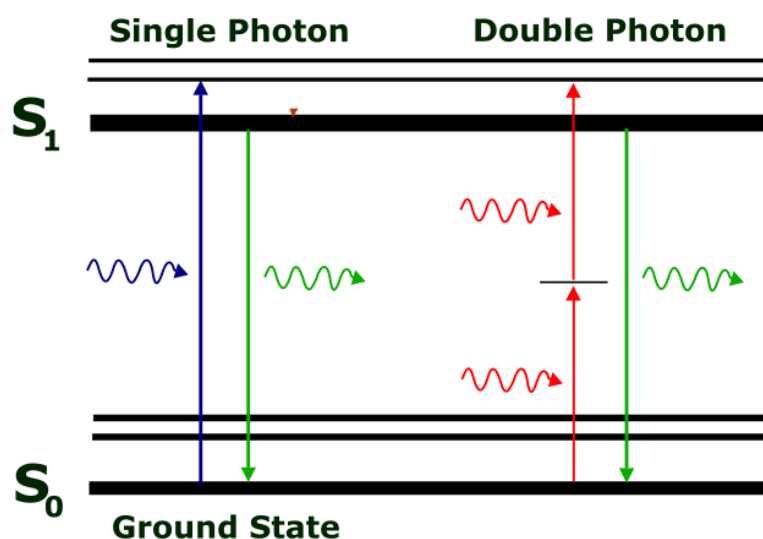


**Figure 7:**

**Contrast of the Jablonski diagram of single- and double-photon excitation.** Both processes induce raise of an electron onto the excited state by absorption of photon energy. However, the absorption involves different number of photons with identical sum of energy. The emitted photon is, therefore, identical in both types. Modified from [98] and [100].

Some modern microscopes, however, use non-linear interactions involving multiple-photon excitation to overcome this issue. Such systems are usually termed as two-photon microscopes (2PLSM)<sup>99</sup>, because more than two photons are rarely involved.<sup>100</sup> These devices enable the use of lower-energetic light to induce higher-energetic fluorescence by interaction of photons. A single photon can, thereby, even carry less energy than the band gap between ground and excited state as long as the energy carried by the sum of all photons is sufficient. For multiple photons to interact, their time-difference of contact with the molecule needs to be shorter than around five hundred attoseconds ( $\sim 500 \times 10^{-18}$  s). The probability of such an event is relatively low, but can be greatly increased by use of ultrashort pulses with high photon density.<sup>99</sup> In a successful case, the energy of all involved photons adds up and is simultaneously transferred onto the molecule. A schematic illustration of the comparison of single and two-photon absorption is shown in figure 7. The illustration shows that either one high-energetic (blue,  $\sim 400$  nm) photon is sufficient for transition to a higher state, or two lower-energetic (red,  $\sim 800$  nm) ones, as they deliver the same energy together as well. In both cases a similar photon (green,  $800 \text{ nm} > \lambda > 400 \text{ nm}$ ) is emitted finally.<sup>98</sup> Correspondingly, the output signal is not changed between both cases, whereas the input regime is finely tunable. Even though adjustment becomes more and more challenging, benefits from nonlinearity are huge. 2PLSMs offer less photobleaching outside the irradiated area, minimized autofluorescence and high 3D-resolution. Moreover, the use of two lower energetic photons allows for a wavelength shift towards regimes with different absorption and scattering behavior, like the NIR-regime.<sup>99</sup> In this way, analysis at deeper tissue level can be highly improved.<sup>99</sup>

# I. Main Project: Magnetothermal Cargo Delivery *in vitro*

## 2 Objective/Motivation

*"Everything is theoretically impossible, until it is done."*  
Robert A. Heinlein

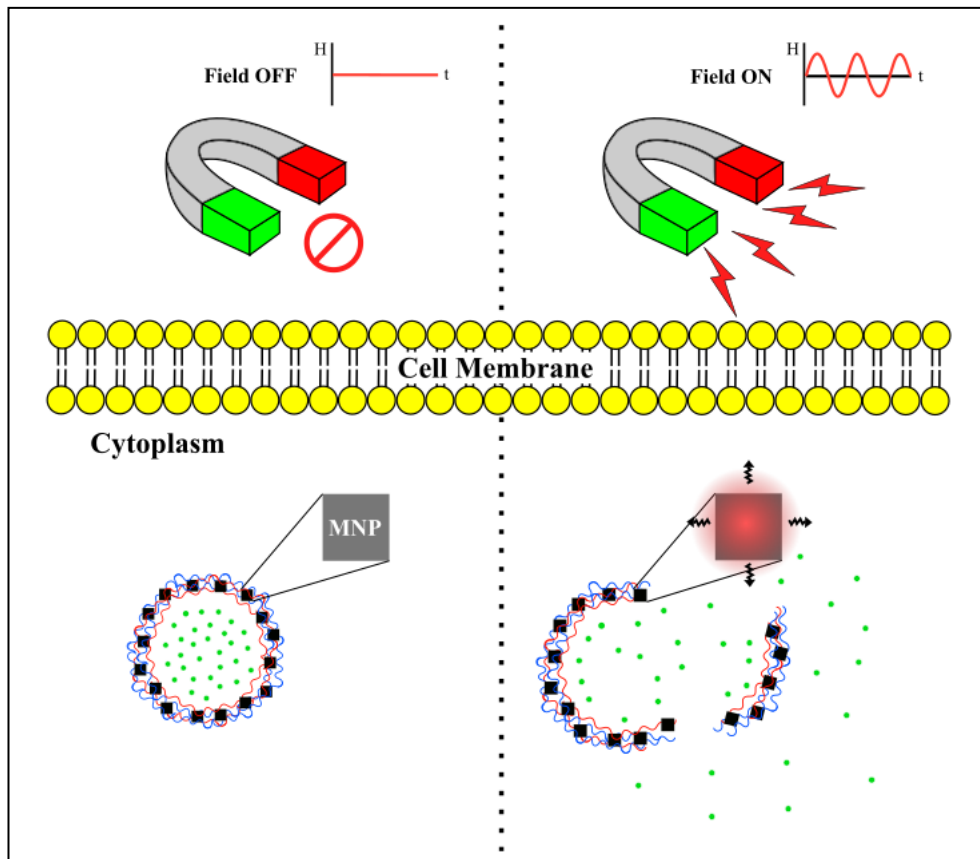


**Figure 8:** Principle of magnetothermal capsule opening in cells. By application of an alternating magnetic field the heating process of magnetic nanoparticles (MNPs) included into the shell of polymer capsules is triggered. As a consequence, the shell is debilitated or destroyed, and the encapsulated cargo is allowed to diffuse out. By use of fluorescent cargo the process can be visualized through fluorescence microscopy.

The target structure of this elaboration are polymeric multilayer capsules for drug delivery purposes. The objective deals with the synthesis and adjustment of such carriers for remote opening under the influence of an external magnetic field. Living cells represent the environment for release evaluation. A schematic overview of the underlying principle is shown in figure 8. Therein, everything below the yellow cell membrane is located in the cytoplasm whereas the area above the bilayer represents the exterior. For absent field (left side), no effect

is induced, and capsules remain stable. Under presence of an alternating field (right), heating of the included MNPs takes place and the capsules release their cargo. Magnetic opening represents a promising approach for medical applications like drug delivery as it is non-invasive and relies on magnetic fields as the trigger. Those offer superiority to comparable triggers like lasers due to less absorption and minimal harm to the body under ideal adjustment. Observation of delivery is enabled by use of fluorescent dyes as cargo. The *in vitro* and *in vivo* outcome of this promising alternative technique, however, needs further investigation.

The first step of the present work was aimed at synthesis and investigation of magnetic nanoparticles. They represented the connector between capsule and field, making them a crucial factor for sufficient cargo delivery. The initial process was directed on a seek for particles with ideal magnetic behavior in alternating magnetic fields. Strong potential to transform the external magnetic into local thermal energy was the prevailing research subject. Analyzation of stability and water solubility plus information gain about properties like size and shape were similarly essential. Outstanding NPs would show very high energy-transformation abilities, which are characterized by high SAR values.

During the follow-up task, the framework was expanded to polymer capsules, especially on their *in vitro* behavior when affected by an AMF. The idea was to include exceptional particles from the first part into the capsule shell to act as the component reacting on the field. Resulting heat surges would induce damage to the surrounding environment and enable shell permeability. Consequently, encapsulated cargo would only be released into the cell interior if triggered by the field but remain restricted inside the capsule core unless. Different shell-sealing and cavity-loading approaches were prepared for investigation. Stability in a trigger-free environment but destabilization under trigger-presence were key points. Brilliant capsules would offer minimal leaching but nearly immediate release when triggered. In an ideal constitution, release would even take place for weak external AMFs restricted by biological safety limits.

In the final section, difficulties and problems were targeted. This explicitly included hurdles related to biocompatible conditions. Center of attention was the actual quantity of heat present across the capsule shell during safely applicable magnetic irradiation. It was decided to compare temperature changes under presence and absence of trigger. Main emphasis was on direct visibility of the issues. For that, infrared imaging was striven as the analyzation technique. Last but not least, it was intended to underline the discrepancies by comparison of the magnetic system with a system working excellent regarding heating and release.

### 3 Materials, Synthesis and Methods

*"A popular cliché in philosophy says that science is pure analysis or reductionism, like taking the rainbow to pieces; and art is pure synthesis, putting the rainbow together. This is not so. All imagination begins by analyzing nature."*

*Jacob Bronowski*

#### 3.1 Materials

##### 3.1.1 Synthesis components

Ammonium bicarbonate (#1066-33-7), benzyl ether (#103-50-4), biphenyl-4-carboxylic acid (#92-92-2), cadmium acetate hydrate (#04-04-43), calcein (#154071-48-4), calcium chloride anhydrous (CaCl<sub>2</sub>, #10043-52-4), Meso-2,3-dimercaptosuccinic acid (DMSA, #304-55-2), (N,N)-dimethylformamide (#68-12-2), ethylenediaminetetraacetic acid disodium salt dihydrate (EDTA (disodium salt), #6381-92-6), ethylene glycol (#107-21-1), iron(III) acetylacetonate (Fe(acac)<sub>3</sub>, #14024-18-1), iron(III) chloride hexahydrate (#10025-77-1), iron pentacarbonyl (#13463-40-6), 1-octadecene (#112-88-9), oleic acid (OA, #112-80-1), oleylamine (#112-90-3), poly(allylamine hydrochloride) (PAH, M<sub>w</sub> ≈ 17.5 kDa, #71550-12-4), poly(ethyleneimine) (#25987-06-8), poly(sodium 4-styrenesulfonate) (PSS, M<sub>w</sub> ≈ 70 kDa, #25704-18-1), sodium carbonate (Na<sub>2</sub>CO<sub>3</sub>, #497-19-8), sodium sulfide (#1313-82-2), triethylamine (#121-44-8) and trioctylamine (#1116-76-3) were purchased from Sigma Aldrich. Chloroauric acid (#27988-77-8) and silver nitrate (#7761-88-8) were bought from Alfa Aesar. Fluorescein-5-isothiocyanate was bought from Fluka. Acetone (#67-64-1), boric acid (#10043-35-3) chloroform (#67-66-3), diethyl ether (#60-29-7), ethanol (#64-17-5), hexane (#110-54-3), sodium hydroxide (#7647-14-5) and toluene (#108-88-3) were ordered from Roth. Propidium iodide (#25535-16-4) was purchased from Invitrogen. Dimethyldioctadecylammonium bromide (#3700-67-2) was purchased from TCI. All chemicals were used as received.

##### 3.1.2 Cell components

Dulbecco's Modified Eagles Medium (DMEM), penicillin/streptomycin (P/S) and trypsin ethylenediaminetetraacetic acid solution (trypsin) were purchased from Fisher Scientific, fetal bovine serum (FBS) and phosphate-buffered saline (PBS) from Biochrom Germany.

## 3.2 Elemental Analysis

Detailed information about elemental concentration in solution was gained by inductively coupled plasma mass spectrometry (ICP-MS). For each analyzed sample a dilution row was prepared. Typically, the stock solution was diluted 20-, 30-, 40- and 50-times. For samples which were expected to be low concentrated the initial dilution was reduced to 15-fold. 20  $\mu$ L of each diluted sample were afterwards digested in 180  $\mu$ L concentrated aqua regia or hydrochloric acid overnight. Before measurement these combined 200  $\mu$ L were finally diluted with 1.8 mL of HCl (2%). Each sample accordingly underwent a hundredfold dilution in acid.

## 3.3 Synthesis

### 3.3.1 Synthesis of Iron Oxide Nanoparticles

#45, #77, #80: 0.71 g (2 mmol) Fe(acac)<sub>3</sub>, 1.1 g (3.89 mmol) oleic acid, 10.42 g (52.6 mmol) benzyl ether and 0.4 g (2 mmol) 4-biphenylcarboxylic acid were mixed inside a 3-neck glass flask. The mixture was degassed at 90 °C for 45 min under continuous stirring at 500 rpm. Afterwards, nitrogen atmosphere and vacuum were alternately applied for 3 times to minimize residual oxygen. The system was then heated to 292 °C at a heating rate of 20 °C/min and subsequently kept at this temperature for 30 min. To purify the resulting particles the substance was cooled down to room temperature and acetone (70 mL) was added. Next, the mixture was centrifuged at 6,000 rpm for 5 – 7 min and the pellet was redispersed in chloroform (~20 mL).<sup>23</sup>  
#34: The amount of oleic acid was 1.27 g (4.4 mmol) and the final temperature 300 °C.

## 3.4 Water Transfer of Magnetic Nanoparticles

### 3.4.1 Transfer using PMA-Nitrodopamine

The transfer by means of a nitrodopamine-linked PMA was achieved by a route slightly modified from literature:<sup>101</sup> 20 mg particles were mixed with 15 mL ethanol and centrifuged at 9,000 rpm for 5 minutes. The supernatant was discarded and the pellet redispersed in a mixture of 1 mL pure tetrahydrofuran (THF) and 33.33 mg poly(isobutylene-alt-maleic anhydride)-nitrodopamine (PMA-ND) previously dissolved in THF (16.66 mg/mL). For better dispersion sonication was applied for 5 minutes. After addition of 5 mL ethanol the mixture was shaken for 3 hours. The particles were precipitated by addition of 20 mL n-hexane and centrifugation at 4000 rpm for one minute. Subsequent redispersion was initiated in 3 mL NaOH (2M) by sonication. Finally, the particles were centrifuged at 5,000 rpm for 3:30 min and washed with water thrice.

### 3.4.2 Transfer using DMSA

Dimercaptosuccinic acid (DMSA) was reported to be a promising candidate,<sup>102</sup> which is well known as medication for heavy metal poisoning.<sup>103</sup> The transfer *via* DMSA was executed slightly modified from literature:<sup>102,104</sup> A specific amount of NPs was dissolved in a solvent like THF or chloroform (e.g. 10 mg in 2 mL) and a significantly higher amount of DMSA (e.g. 40 mg) dissolved in 2 mL DMSO was added. The mixture was sonicated for 1h and then shaken overnight. Afterwards, it was centrifuged at 5,000 rpm for 5 min. A similar amount of DMSA was added to the precipitated particles to induce further connection of ligands.

### 3.4.3 Nanoparticle Transfer using PMA-Dodecylamine

Transfer was achieved by a slightly adjusted protocol:<sup>105</sup> 10 mg particles were mixed with PMA-Dodecylamine (PMA-DDA) in 50 mL chloroform at a ratio between 3,000 and 9,000 PMA-monomers per particle surface unit area.<sup>106</sup> The solvent was evaporated for 10 min at 310 mbar and 40 °C inside a rotary evaporator. The resulting film was redispersed in chloroform and evaporated two more times. 15 mL water were added together with a small amount of NaOH (2 platelets) to hydrolyze the PMA under continuous movement and sonication. The mixture was centrifuged and the resulting pellet washed with water twice.

### 3.4.4 Nanoparticle Transfer using PEI

5 mg of particles dissolved in chloroform were mixed with 10 kDa PEI ( $M_w = 25$  kDa) dissolved in 50 mL DMSO. After 48 h reaction at room temperature the particles were collected magnetically and redispersed in 5 mL water.<sup>46</sup>

## 3.5 Synthesis and Functionalization of Polyelectrolyte Capsules

PEMCs were synthesized corresponding to the typical protocol around calcium carbonate ( $\text{CaCO}_3$ ) cores.<sup>12</sup> Initially,  $\text{CaCO}_3$ -templates were prepared under room temperature by mixing equal volumes (typically 1 mL) of  $\text{Na}_2\text{CO}_3$  (0.33 M) and  $\text{CaCl}_2$  (0.33 M). The mixture was magnetically stirred (1000 rpm) for 30 s, subsequently left still for 135 s, transferred into an Eppendorf tube (2 mL) and finally washed with Milli-Q water for three times. The typical average template size was determined as around 4 to 6  $\mu\text{m}$  from confocal images. Subsequent LbL-assembly of a polymer shell around the template was achieved by addition of polymer solutions to the cores. For that, 2 mL solution of positively charged PAH ( $M_w = 17.5$  kDa) and negatively charged PSS ( $M_w = 70$  kDa) (both: 10 mg/ml in 0.05 - 0.1 M NaCl (aq.)) were

alternately added to the precipitated cores after removal of previous supernatant and washing. The tubing was then sonicated for 3 min and subsequently shaken for 10 min to allow for adsorption. Residual polymer was washed away in three washing steps with Milli-Q water. After formation of two polymer bilayers (PSS/PAH)<sub>2</sub> and followed by an additional PAH-layer, MNP solution could be added to form a particle layer by electrostatic interaction. Multiple MNP-layers are optional but need to be separated by one PAH layer. After complete assembly, the cores were dissolved by addition of ethylenediaminetetraacetic acid (EDTA, 0.2 M, pH 7) overnight which allowed for complexation of the Ca<sup>2+</sup> ions. The hollow capsules were then postloaded with dye by addition of dye solution for 1 h and subsequent heat-shrinkage at ~75 °C for 90 min. Free dye was washed away in three washing runs with MilliQ-water. Some specific capsules were capped with DDAB liposomes on the shell instead of heat shrinkage. For that, DDAB had to be set up. It was initially dissolved in chloroform at a concentration of 0.5 mg/mL with subsequent removal of CHCl<sub>3</sub> under rotary evaporation. Afterwards, 25 mL water were added and the DDAB-water-system was sonicated for a few minutes. The liposomes could then be added to the capsules (outmost layer PSS!) similar to the polymer shells due to electrostatic forces between PSS and DDAB. The concentration of capsules for a system achieved by mixing 1 mL of each initial chemical was usually around  $5 \times 10^7 \text{ ml}^{-1}$ .

### 3.6 2D Cell Culture and Capsule Incubation

For *in vitro* examination, human breast cancer cells (MCF-7) and human cervical cancer cells (HeLa) were cultured in Dulbecco's modified Eagle's medium (DMEM) supplemented with 10% (v/v) fetal bovine serum and 1% (v/v) antibiotics at 37 °C and 5% CO<sub>2</sub> inside culture flasks. For observation, a total number of around  $1.5 \times 10^5$  (HeLa) or  $3 \times 10^5$  (MCF-7) human carcinoma cells was seeded inside 2 mL cell medium on a 35 mm diameter ibidi  $\mu$ -dish. After attachment overnight, the culture medium was replaced, a precise number of capsules was added and the system incubated for roughly 24 h. Due to their micron-size, the number of capsules could be counted and calculated with a hemocytometer before addition. Directly before observation a second medium change was applied and free capsules were washed away with PBS. Finally, the dish was moved to the microscope and placed on its three-dimensional stage.

### 3.7 3D Cell Culture

Tumor spheroids were obtained from cell monolayers *via* a hanging drop method.<sup>107</sup> Initially, a standard trypsinization procedure was utilized to detach cultured cells. Then, cells were resuspended in culture medium and the concentration was counted. The cell medium containing the desired cell number ( $\sim 350,000 \text{ mL}^{-1}$ ) was mixed with methyl cellulose (MC, 1-2 %) at a volume ratio of 3:1. Multiple individual droplets, containing 20  $\mu\text{L}$  each, were taken from the mixture and placed on a petri dish lid, which was subsequently inverted and placed above the dish. The latter was previously filled with deionized water to minimize droplet evaporation. Incubation took place at 37 °C and 5%  $\text{CO}_2$  for 24 h. Formed aggregates were transferred into a 24-well plate previously coated with 300-400  $\mu\text{L}$  agarose. Final spheroids were collected after 2-3 days of growth time. For capsule tests, the specific amount of capsule solution was added during the mixing step. In a typical synthesis the capsule-to-cell ratio was set as 2:1.

### 3.8 Imaging Principle

Fluorescence and optical images were recorded with an upright confocal laser scanning microscope (LSM880, here also referred to as: 2-photon) from Zeiss. For classical observation, a water-immersed objective (W Plan-Apochromat 20x/1.0 DIC D = 0.17 (UV) VIS-IR M27 75mm) was inserted into the medium and the sample illuminated by the laser (typically:  $\lambda_{\text{ex}} = 488 \text{ nm}$ ). Emitted light was recorded by a PMT and a GaAsP PMT spectral detector. Under simultaneous scan of phase contrast and the (green) fluorescence, both cells and capsules could be identified and their condition be evaluated. For capsule opening analysis, pictures were commonly recorded before and after contact with the magnetic field to visualize changes. On this account specific positions on the petri dish were initially chosen based on cell density and the amount of capsules present. This was facilitated by use of dishes from ibidi with an imprinted location grid of 500  $\mu\text{m}$  lateral expansion. Transmission and fluorescence were captured for each position. The dish was subsequently moved to the coil set for field irradiation to induce capsule opening. Immediately after field shutdown the dish was re-transferred to the microscope and the previously chosen positions were observed regarding phase contrast and fluorescence again. The microscope settings were not changed in between.

### 3.9 Magnetic Heating

Magnetic fields were produced by a device called D5 Series, which was fabricated by nanoScale Biomagnetics. The system has been designed specifically for magnetic heating and hyperthermia experiments. The device comes with several coil sets and attachments for multiple

applications. Classical opening tests were done under use of either a planar or a calorimetry coil set for magnetothermal heating with each producing alternating magnetic fields of diversely tunable properties. For seeded cells, the experimental petri dish was positioned on top of the planar coil set. Magnetic fields were then applied for a specific time duration. To minimize influences of field irregularities across the system, dishes were always placed in the center of the coil set. Moreover, their lid was always kept close to avoid evaporation or other external influence factors. At later stages the dish was occasionally rotated during the experiments by hand but still not moved horizontally or vertically. Seeded cells were usually irradiated by the maximum field achievable by the planar set ( $f = 300$  kHz,  $H = 15.5$  kA/m) as it fulfills the biological limit (*i.e.*  $H \cdot f < 4.85 \times 10^8$  Am<sup>-1</sup>s<sup>-1</sup>) for biomedical applications. Calorimetry tests required a solution of detached cells in culture medium, which was transferred into a specifically designed small glass vial and then irradiated by the field. The majorly used condition ( $f = 487$  kHz,  $H = 29$  kA/m) for solutions, however, exceeded the limit. In both cases a control sample was kept outside the field at room temperature in parallel to allow for comparison and evaluation. Fluorescence and optical imaging were applied both prior as well as after field application to compare both situations and to look for opened capsules. Opening was identified by dye release into the cell cytosol. In the case of calorimetry opening, the cells were either seeded after irradiation or analyzed by flow cytometry.

#### 3.10 Flow Cytometry

To analyze release for a higher cell number, the principle of flow cytometry was used. For that, cells were mixed with capsules inside a falcon tube at a desired concentration and rotated (10 turns per minute) overnight inside the incubator. Next, a specific cell amount was taken out, centrifuged at 300 rcf for 5 minutes, resuspended in PBS solution (400  $\mu$ l) and transferred into a flow cytometry tube. Upon irradiation with a laser ( $\lambda = 488$  nm) the resulting fluorescence was recorded for a total of 10,000 cells. Beforehand, the cell population was confined on single, intact cells by gating. The forward-scattered signal was acquired and tuned to remove cell debris and free capsules. A sample of pure cells without capsules was used as control.

#### 3.11 Thermal Imaging

Thermal images were recorded by a Optris Xi 400 infrared camera (Optris, Germany) equipped with a spectral range lens of 18° x 14°. The camera has an uncooled FPA detector with a frame rate of 80 Hz and a resolution of 382 x 288 pixel. Detection included infrared waves in the spectral regime from  $8 \mu\text{m} \leq \lambda \leq 14 \mu\text{m}$ . Any infrared emission from the sample was

recalculated by the corresponding PIX Software and directly displayed as temperature-related colored structures. Structures with low temperature were plotted as black or blue while hot areas appeared yellow or orange. Temperature differences of 0.1 °C or higher were resolved. In a typical measurement the sample was placed inside a 35 mm ibidi dish and observed from above. Distance between camera and sample was set to around 15 cm.

## 4 Results

*"There are two possible outcomes: If the result confirms the hypothesis, then you've made a measurement. If the result is contrary to the hypothesis, then you've made a discovery."*

*Enrico Fermi*

The aim was to establish a magneto-responsive carrier utilizable for controlled release of cargo inside living cells. In fact, the *in vitro* usability of such carriers lacked extensive examination. Previously made progress on the establishment procedure can be gleaned in the literature.<sup>108</sup> Briefly, it was confirmed that magneto-responsive release was possible inside living cells. However, significant problems concerning the intended but also the premature release occurred. The initial future target was to improve the stability and release behavior in 2D cell systems. Further on, analyzation of differences to the photothermal counterpart and display of the local heating ability/procedure during field application were intended.

### 4.1 Improving Particle Properties and Heating Behavior<sup>[b]</sup>

Numerous particles varying in composition, size and shape had already been synthesized.<sup>108</sup> However, their heating ability remained below expectations. As a consequence, new synthesis strategies and approaches were tested regarding a boost in heat production. Focus was on iron oxide nanoparticles (IONPs), which were multiply reported to show outstandingly high SAR values.<sup>21-23,27,109-111</sup> After synthesis, all particles underwent surface ligand-exchange to enable water-solubility. Subsequently, tests regarding their heating ability under magnetic field irradiation were carried out. Each new particle batch was classified based on its specific absorption rate.

#### 4.1.1 Iron Oxide Particles

Several published synthesis strategies were reproduced to gain a big library of iron oxide nanoparticles. Structure and size within these reports strongly varied, which was beneficial due to literature contradicting in terms of ideal MNP properties.<sup>21,23,27,109-111</sup> Resulting diameters ranged from around 10 nm to above 100 nm. This huge regime envelopes ferromagnetism (FM) for bigger but also superparamagnetism (SPM) for smaller NPs, as the transition takes place below 20 nm.<sup>112</sup> Both types come with different mechanisms of heat production:<sup>113</sup> while SPM relies on Néel and Brown relaxation, FM is based on hysteresis loss. Each principle is said to

enable high amounts of heat.<sup>113</sup> Gained shapes included spheres, cubes and other forms. Both form and size were determined by scanning electron microscopy. Main focus of the library was the particle-based heat generation under irradiation by a magnetic field alternating with radio frequency (AMF). This ability is characterized by the specific absorption rate (SAR). High SAR values determine strong capability of field conversion into heat. The majority of syntheses ended up with poorly heating particles ranging close to or even below 100 W/g (*cf.* Appendix). One synthesis route<sup>23</sup>, however, delivered particles with outstanding specific absorption rates in the regime above 1000 W/g, being significantly above average.

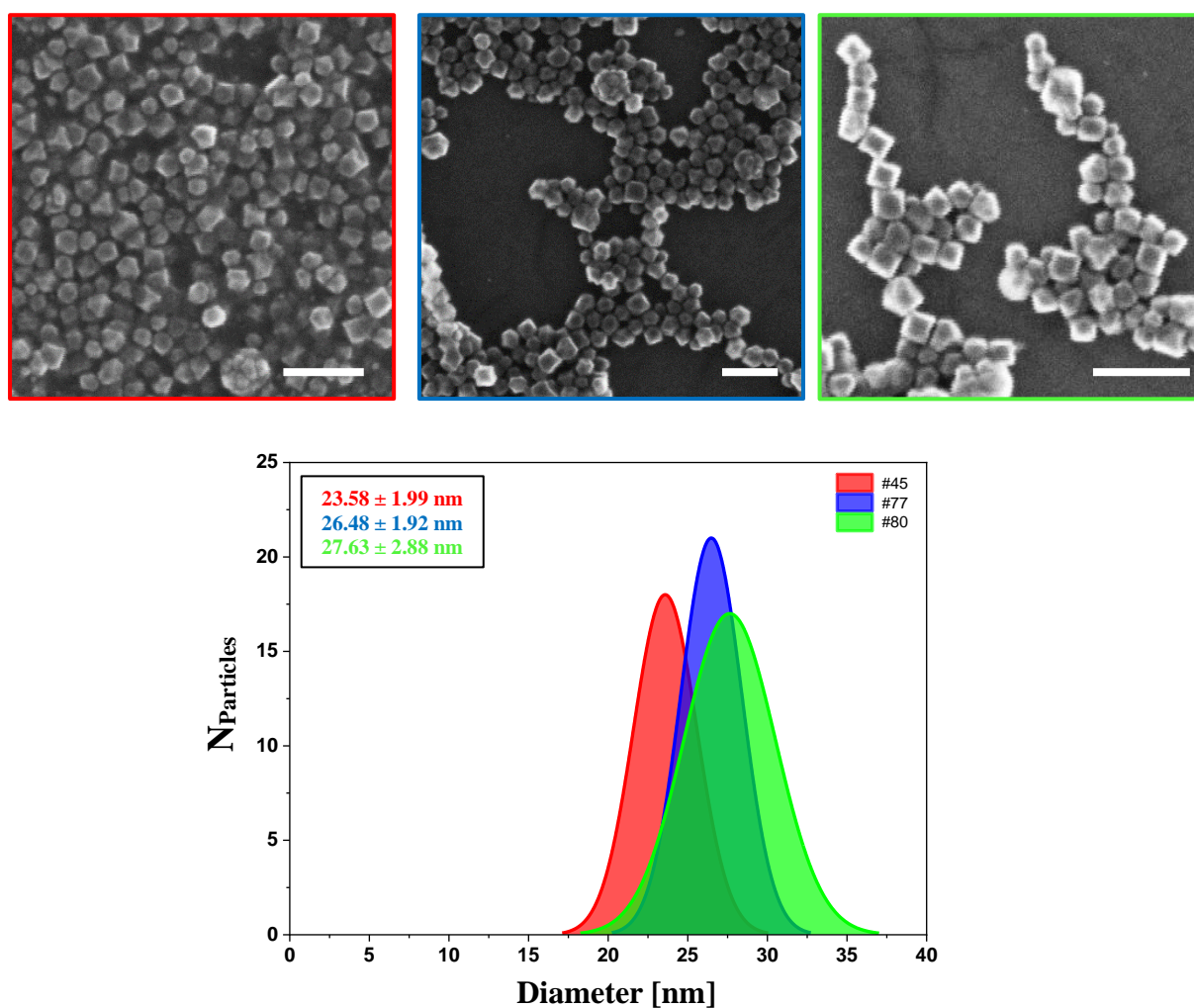


**Figure 9:** SEM image and size distribution of three outstanding IONP batches. These particles (#45: red, #77: blue, #80: green) consisted of iron oxide and showed superior heating ability. Their size was distributed around a mean diameter close to 25 nm and the shape was a mixture of cubes and diamonds. **Scales: 100 nm**

This specific route was redone several times to gain a big stock of strongly heating MNPs. Resting on their position in the chain of production they were named as for instance #34, #45, #77 and #80. The SEM images of the three strongest heaters are shown together with their size distribution in figure 9, #34 is not featured as its maximum value ( $\sim 662$  W/g) didn't exceed 1000 W/g. Major shapes present for these NPs are cubes and diamonds, mean diameters range between 23 and 28 nm. The field used for SAR determination was set to a field strength of  $H = 29$  kA/m while alternating with a frequency of  $f = 487$  kHz. It represented the highest field achievable with the present machine. Heat conversion was not identical for the three batches. A diagram of their values is shown below in figure 10. The lowest SAR was measured as slightly below 1500 W/g whereas the highest reached around 2340 W/g. These values clearly exceed 1000 W/g. Moreover, they nearly equal the excellent values achieved by Guardia *et al.* (1400 W/g)<sup>21</sup> and Tong *et al.* (2560 W/g)<sup>27</sup>. All mentioned values were obtained by NPs dissolved in water after ligand transfer towards PMA-DDA.

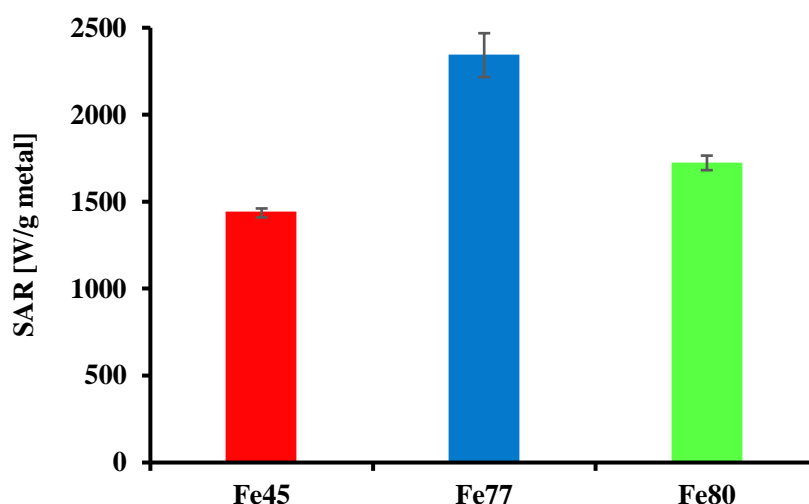


**Figure 10:** Highest SAR values of the used IONPs. The three particles #45, #77 and #80 which offer values up to 2340 W/g are the best heaters synthesized during the studies. All shown results are connected to water-transfer by PMA-DDA.

#### 4.1.2 Coating Strategies<sup>[b]</sup>

Based on the synthesis procedure used for the particle preparation (*i.e.* thermal decomposition), all sample batches resulted in particles insoluble in water due to a hydrophobic surface. This lack of solubility is a well-known outcome caused by the surface stabilizer (here: oleic acid) used as the ligand during the synthesis.<sup>114,115</sup> Fortunately, an exchange of this ligand doesn't represent a nerve-wracking problem as several replacement procedures have already been

published.<sup>12,21,114,115</sup> Different transfer routes and transfer ligands offer diverse results concerning for instance yield, exchange ratio and solubility. Here, a number of coating strategies based on different hydrophilic molecules were applied and tested. Some ligands were tried but didn't result in good dispersibility as for example poly(acrylic acid) (PAA). The four satisfactory molecules included poly(isobutylene-*alt*-maleic anhydride)-linked dodecylamine (PMA-DDA) and nitrodopamine (PMA-ND) as well as dimercaptosuccinic acid (DMSA) and polyethyleneimine (PEI). For those, particles were initially transferred into water successfully. After ligand exchange, the particle behavior under field irradiation was examined immediately. Despite their similarity in size, shape and composition to the reported model, the particle ability to produce heat continuously remained below expectations. This might be caused by the choice in transfer ligands, which differed from literature. As a consequence, the previously mentioned coating strategies were compared regarding their influence on the heating efficiency. For that, each ligand was linked to particles from batch #77. After exchange, comparison of SAR was carried out under similar field conditions [ $H = 29$  kA/m,  $f = 487$  kHz] at the same concentration [ $c_{\text{Fe}} = 1$  mg/mL, determined by ICP-MS].

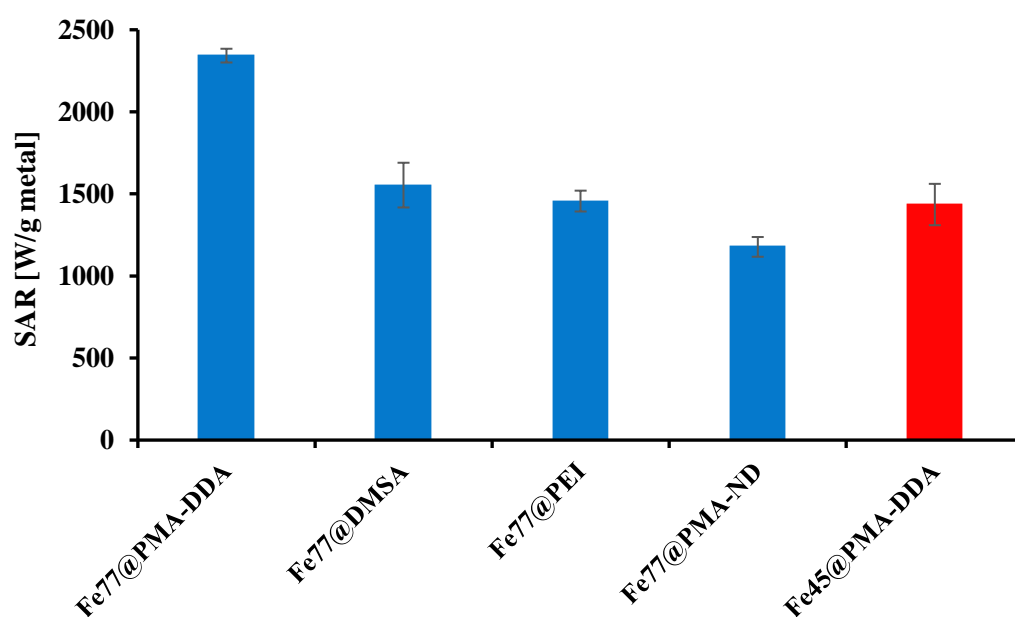


**Figure 11:** **Transfer-ligand influence on heating ability.** To determine the influence of different water transfer strategies on the heating capability, IONPs from the same batch (#77) were coated in four different ways and their SAR was compared (blue bars). Significant differences occurred, showing that PMA-DDA offered the highest value. It was even higher than the previously best particle, which is shown in red.<sup>[b]</sup>

In figure 11 the resulting SAR values are presented. In addition to the four differently coated particles from batch #77 (blue bars), another sample based on batch [#45] is shown as a control group (red bar). Till the preparation of the examined batch #77, particle #45 exhibited the strongest heating ability with a value of 1937 W/g. Both batches were synthesized via the same route, #45 was coated with PMA-DDA. It is clearly visible that the ligand-dependent values are not similar. Quite the contrary, a gap of more than 1000 W/g appears between the best (@PMA-DDA) and the worst (@PMA-ND) condition. During the previously reported tests<sup>108</sup> all particles were either coated with PMA-ND or DMSA. The latter replaced the nitrodopamine-relative due to advantages including increased transfer speed and omission of elaborate steps like hydrolyzation. Unfortunately, these ligands both represent agents causing a reduction in heating capability in a more or less drastic way, which explains discrepancies to literature. Major variances between different water-transfer ligands lie in the residual amount of original stabilizer bound to the particle surface and the effects during substitution. During the ligand-exchange, it can either be replaced by the new molecule or interact with hydrophobic side chains of the new ligand to form a bilayer. In the second example, the primal ligand remains attached to the particle but gets capped with a layer of hydrophilic ligands.<sup>46,115</sup> Both alternatives affect the particle interaction with the field in a specific way. For the herein analyzed particles, the original ligand was oleic acid (OA). From the used transfer-ligands, PEI and DMSA consist of functional groups (*i.e.* amine group and thiol/carboxylic groups, respectively) with strong binding affinity to IONPs.<sup>46,102</sup> They are most likely to replace their hydrophobic predecessor.<sup>46,102</sup> A small amount of residual OA-molecules will, however, still remain on the surface.<sup>102</sup> On the contrary, PMA-DDA fits into the group of ligands linking to the oleic acid to form a bilayer.<sup>105</sup> While its dodecylamine interacts with the oleic acid through Van-der-Waals forces between the long alkyl chains the PMA forms a hydrophilic outer layer. As a consequence, the amount of OA at the surface remains mainly unchanged. Finally, PMA-ND was invented as a new ligand, which consists of a ND linked to the PMA through an amide bond. It represents a replacing ligand despite the included PMA. Similar to dopamine-based PMA molecules<sup>105</sup> the connection of NP to ligand appears with help of the strongly binding catechol group. Due to the nitro-group attached to the catechol the binding tendency is additionally enhanced. Based on the measurement results, PMA-DDA is most-favored in terms of heating whereas PMA-ND is deprived and PEI and DMSA range in the middle. In connection to their capping mechanisms it seems plausible that removal of OA weakens the heating capability. The lower the residual amount the stronger the drop in SAR, down to PMA-ND with expected remaining OA on the surface to be least. Surface properties are a crucial influencer on

magnetic properties, especially in nanoparticles where surface atoms take a huge percentage.<sup>116,117</sup> Through exchange, processes like oxidation or ion removal appear on the particle surface. In this context, replacement towards DMSA has for instance been observed to induce increased presence of maghemite in close contact to magnetite, which confirms enhanced oxidation after exchange.<sup>118</sup> This process significantly affected the magnetic properties. With respect to the formation of maghemite from magnetite the saturation magnetization ( $M_s$ ) dropped significantly.<sup>118,119</sup> A total decrease in  $M_s$  of 30% was observed for a ligand change from oleic acid to DMSA by Palma *et al.*<sup>118</sup> All these surface changes go along with a more or less strong influence on the particle (magnetic) anisotropy.<sup>63,116,117,120</sup> This in turn impacts the heating mechanisms, especially Néel relaxation (*cf.* chapter 1.3). Alterations in anisotropy go along with transformation of the energy barrier dividing the two orientations of the magnetic moment along its easy axis inside the particle. Hence, the relaxation time for the mechanism is modified and the overall heating behavior manipulated.<sup>63,121</sup> As a consequence, ligands with strong impact on the surface (here especially: PMA-ND) are likely to show a more intense impact on heating in comparison to capping ligands.<sup>63,118</sup> In terms of solubility and long-time stability all coatings were expected to be suitable corresponding to literature.<sup>46,101,102,105</sup> Nevertheless, significant differences appeared when solubility was checked after some storing break. Particle batches coated with DMSA showed irreversible precipitation of a portion of NPs after some hours. Batches capped by PMA-DDA were stable for a longer time but ended up insoluble as well. The only precipitation-free coating was PMA-ND which, however, required a multi-step cleaning procedure to remove hydrolyzed PMA and had the worst influence on heating. In case of DMSA this might for instance be explained by formation of disulfide bonds in between different particles over time which leads to delayed aggregation.<sup>118</sup> Reasons for the other coatings were not worked out. As solubility represents a crucial property for biomedical application, only PMA-ND was further used as soon as the precipitation was detected for the other coatings. Despite its attenuating behavior on hyperthermia it still allows for outstandingly high SAR values.

## 4.2 Capsule Characterization

Polyelectrolyte multilayer capsules were chosen as carrier systems. By means of LbL-assembly differently structured containers were prepared. All of these PEMCs were predominantly shaped spherically. By variation of the time parameters during synthesis, the capsule diameter could be tuned finely. In this way it was usually centered around 4 - 6  $\mu\text{m}$ . With PAH and PSS

two common non-biodegradable<sup>13,18</sup> polyelectrolytes were used for shell formation around the core. Due to their opposite charge (PAH = +, PSS = -), electrostatic interaction allowed for simple attachment of subsequent layers onto the predecessor. Meanwhile, the most promising MNPs were taken from the particle library and inserted into the shell for functionalization. Arising from their negative charge, implementation was achieved by placement in-between two positively charged PAH-layers. While transporters with polymer-only shells are non-interactive, particle-tuned counterparts show significant interaction with external magnetic fields. Adjusting the amount of MNPs attached to the surface represented the crucial factor. In terms of capsule opening, too little quantity of particles might lack heating efficiency whereas too much can lead to unbound particles, influencing cell viability during later application. Fluorescent dyes were used as cargo. They allowed for direct observation via fluorescence microscopy. Typically, the green-fluorescent dye calcein was used. After excitation by a laser, *e.g.*  $\lambda_{\text{ex}} = 488 \text{ nm}$ , it shows strong fluorescence at around  $\lambda_{\text{em}} = 514 \text{ nm}$ . Due to its low molecular weight of around 622 Da, encapsulation was attained by postloading into the hollow cores.<sup>122</sup> Coming with cell impermeability, which is caused by its abundant carboxylic acid group, and long retention time it stays entrapped inside the cells over the whole experimental period once it is transported inside.<sup>123</sup> The less-used other dye was PEI-FITC. By attachment of FITC to the big polymer PEI, dye size and weight ( $M_w > 10 \text{ kDa}$ ) were significantly increased. With sizes overcoming pore diameter, preloading is required. FITC can be excited by the same laser as calcein and shows strong green fluorescence as well. A representative insight into the capsule properties is shown in figure 12. The illustration combines the principal idea with the finished product and its characterization. In subfigure A the theoretical structure is shown. Red and blue lines represent the differently charged polyelectrolytes representing the shell. Due to their electrostatic counterplay strong interaction takes place. The circular form is based on the shell formation around spherical  $\text{CaCO}_3$  templates, which are removed after addition of the final layer. The black squares display the potential nanoparticles. The cubic form is not representative for all library MNPs. Finally, green circles display the encapsulated cargo. The color is chosen on the expected green fluorescence. All major chemicals, *i.e.* PAH, PSS and calcein, are presented in part B of the illustration. Each one is colored in accordance with its appearance in part A. Corresponding functional groups are clearly visible. Direct insight into the finished capsules is offered by subpicture C, which shows an image taken by fluorescence microscopy. It can be seen that the carrier is shaped spherically and that the fluorescence of the loaded calcein is confined to the capsule interior. Moreover, the shell appears darker than the core, which links to the presence of black iron-oxide nanoparticles in the shell.

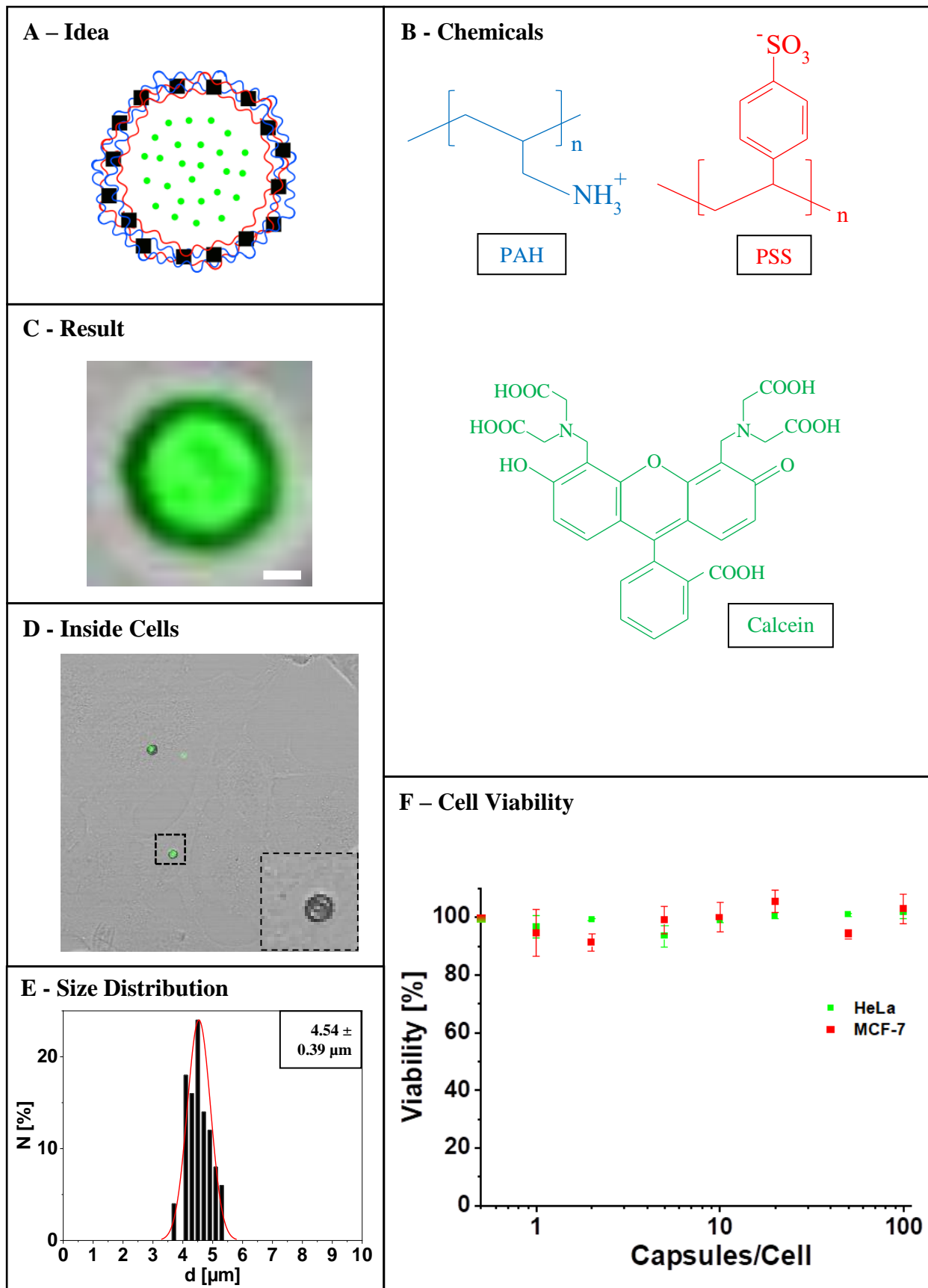


**Figure 12: Polymer Capsules: Idea, Characterization and Outcome.**  
**(A): Sketched Idea** Spherical carriers with polymer-based shell and MNP-functionalization are loaded with fluorescent cargo. **(B): Chemicals** The differently charged polymers PAH (+) and PSS (-) are used for shell formation. Cell impermeable and green-fluorescent calcein is used as cargo. **(C): Result** Manufactured carriers were analyzed by fluorescence microscopy to evaluate loading and shape. Both parameters fit expectations (*i.e.*, sphere, strong green color). **Scale: 2  $\mu\text{m}$**  **(D): Inside Cells** Capsules do not suffer damage, intensity drop or shape change during cell uptake. **(E): Size Distribution** Diameter was measured for 50 capsules. The resulting value was tightly centered around a mean of 4.54  $\mu\text{m}$  **(F): Cell Viability** To confirm minimal toxicity multiple capsules were added to single cells. Even at very high ratios viability did not drop which confirms safe use of capsules *in vitro*.

Comparison of subfigures A and C indicates clear agreement of principle and result. Subfigure D displays the situation inside living cells (here: HeLa). Capsule shape and fluorescence did not undergo significant changes during uptake. The carrier remained spherical and highly-fluorescent. The shape is additionally highlighted at the bottom right corner for clarification. Moreover, the cells are healthy and not visibly influenced by capsule presence in their cytosol. Square E portrays the size distribution calculated by analyzation of 50 different capsules. The diameter was centered on a mean value of 4.54  $\mu\text{m}$  with a standard deviation of 0.39  $\mu\text{m}$ , which complies with the intended regime of 4-6  $\mu\text{m}$ . Finally, part F demonstrates the cell viability against increasing capsule number per cell. Data received from HeLa cells is presented by green data points whereas MCF-7 data is shown in red. Results are averaged for well-triplets inside a 96-well ibidi plate. Each well contained 30,000 cells at initial seeding. Viability was evaluated after 24 h attachment time and subsequent overnight co-incubation with capsules by a resazurin viability assay. For both cell types, data points remain in a viability regime above 90 % for all conditions. This confirms minimal cell harm by uptake of several capsules ranging up to really high numbers of 100 capsules per cell. This unequivocally validates good biocompatibility of the present capsules. Typical experimental conditions included only two capsules per cell.

During this elaboration, multiple capsule types have been fabricated. The following tables 1 and 2 represent the entirety of capsule batches prepared. Batches usually included several millions of capsules per milliliter. The lists are divided into capsules loaded with either PEI-FITC or calcein. In addition to the cargo, the capsules varied in shell structure, particle choice and the amount of IONPs added per particle-layer. Due to limited space, some parts of the shell structure are replaced by symbols. The corresponding explanation can be found at the bottom of the list. A typical shell included four inner layers - two positive and two negative - followed by the first particle layer. A secondary particle layer was added in between two other positive layers if needed. The shell was completed by several additional polymer layers.

**Table 1: PEMCs loaded with PEI-FITC.**

| <i>Name</i>  | <i>Particle</i> | <i>Fe Amount / Layer</i> | <i>Total Structure</i>            | <i>Dye</i> |
|--|-----------------|--------------------------|-----------------------------------|------------|
| <i>CS A</i>  | #34             | 0.92 mg                  | $\Delta$ /NPs/PAH/PSS/PAH         | PEI-FITC   |
| <i>CS B</i>  | #34             | 0.92 mg                  | $\Delta$ /NPs/PAH/NPs/PAH/PSS/PAH | PEI-FITC   |
| <i>CS C</i>  | #34             | 0.92 mg                  | $\Delta$ /NPs/PAH/PSS/PAH         | PEI-FITC   |
| <i>CS D</i>  | #34             | 0.92 mg                  | $\Delta$ /NPs/PAH/NPs/PAH/PSS/PAH | PEI-FITC   |
| <i>CS E</i>  | #34             | 0.92 mg                  | $\Delta$ /NPs/PAH/PSS/PAH         | PEI-FITC   |
| <i>CS F</i>  | #34             | 0.92 mg                  | $\Delta$ /NPs/PAH/NPs/PAH/PSS/PAH | PEI-FITC   |
| Capsules CS C-F were also coated with DDAB and loaded with hydrogen carbonates (HC): Ammonium-HC (C+D) or Sodium-HC (E+F). |                 |                          |                                   |            |
| $\Delta$ : (PAH/PSS) <sub>2</sub> /PAH   |                 |                          |                                   |            |

**Table 2: PEMCs loaded with calcein.**

| <i>Name</i>   | <i>Particle</i> | <i>Fe Amount / Layer</i> | <i>Total Structure</i>                   | <i>Dye</i> |
|---|-----------------|--------------------------|--|------------|
| <i>CS 1</i>   | #34             | 0.92 mg                  | $\Psi$ /NPs/PAH/NPs/PAH                  | Calcein    |
| <i>CS 2</i>   | #34             | 1.38 mg                  | $\Psi$ /NPs/PAH/NPs/PAH                  | Calcein    |
| ( <i>mean CS</i> )                                  | #34             | 1.10 mg                  | $\Psi$ /NPs/PAH/NPs/PAH                  | Calcein    |
| <i>CS 3</i>   | #34             | 15.65 mg                 | III /P(Am-DDA)/NPs/PAH/PSS               | Calcein    |
| <i>CS 4</i>   | #34             | 1.10 mg                  | $\Psi$ /NPs/PAH/NPs/PAH/PSS              | Calcein    |
| <i>CS 01</i>  | #45             | 0.5 mg                   | $\Psi$ /NPs/PAH/PSS                      | Calcein    |
| <i>CS 02</i>  | #45             | 0.5 mg                   | $\Psi$ /NPs/PAH/NPs/PAH/PSS              | Calcein    |
| <i>CS 03</i>  | #77             | 0.5 mg                   | $\Psi$ /NPs/PAH/PSS                      | Calcein    |
| <i>CS 04</i>  | #77             | 0.5 mg                   | $\Psi$ /NPs/PAH/NPs/PAH/PSS              | Calcein    |
| <i>CS 05</i>  | #80             | 0.9 mg                   | III /PDADMAC/NPs/PAH/PSS                 | Calcein    |
| <i>CS 06</i>  | #80             | 0.9 mg                   | III /(PDADMAC/NPs) <sub>2</sub> /PAH/PSS | Calcein    |
| $\Psi$ : (PSS/PAH) <sub>2</sub><br>III: PSS/PAH/PSS |                 |                          |  |            |

### 4.3 Capsule Opening Studies in 2D

#### 4.3.1 Change of Encapsulated Dye

As indicated earlier, magnetically induced release was already observed but lacked a sufficient opening ratio.<sup>108</sup> To further improve opening and premature release, multiple approaches were tried in this study. As a lead-in, the encapsulated dye was changed towards a bigger molecule, which was expected to not pass through the pores of the capsule system. In this way, heat-shrinkage could be elided. Shrinkage was anticipated to represent one of the biggest concerns regarding a substantial release as it causes really tight and stiff shells.<sup>16,18</sup> The new dye consisted of fluorescent fluorescein-5-isothiocyanate (FITC) linked to the branched and size consuming polymer polyethylenimine (PEI). The maximum fluorescence emission for excited ( $\lambda_{\text{ex}} = 490 \text{ nm}$ ) PEI-FITC is located at a wavelength of  $\lambda_{\text{em}} = 525 \text{ nm}$ , appearing as a green color. Initially, one capsule set containing one IONP-layer (#34, 0.92 mg added) was prepared and loaded with PEI-FITC *via* preloading. Its structure was set as (PAH/PSS)<sub>2</sub>/PAH/NPs/PAH/PSS/PAH (CS A, *cf.* chapter 4.2, table 1). The resulting capsules offered strong green fluorescence when observed in solution but also after uptake by MCF-7 cells (*cf.* figure 13). Moreover, no cell turned green due to capsule leaching after uptake. So, premature release was prevented, indicating that these carriers are completely leakproof under the considered conditions.

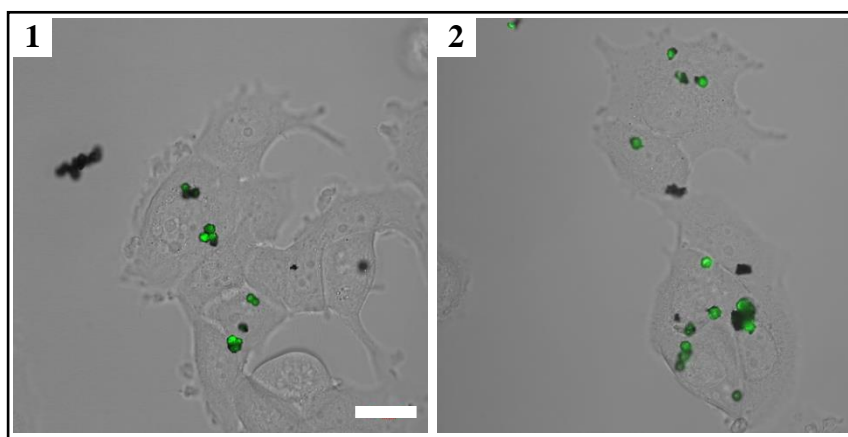


**Figure 13:** PEI-FITC loaded capsules inside MCF-7 cells. Despite the absence of heat shrinkage and the corresponding remaining porosity the capsules loaded with PEI-FITC showed no premature release but good fluorescence inside MCF-7 cells. Unfortunately, both one-layered (left) and two-layered (right) also didn't show intended release by magnetic heating [ $f = 296.6 \text{ kHz}$ ,  $H = 15.5 \text{ kA/m}$ ].  
**Scale: 20  $\mu\text{m}$**

Unfortunately, increased stability went along with poor opening. During release tests inside an ibidi 8-well plate, which was placed on the planar coil set and irradiated at a frequency of  $f = 296.6$  kHz and a field amplitude of  $H = 15.5$  kA/m for a time period of  $t = 1$  h, not a single opening process was observed. In addition to dye exchange, this might have been related to low amount of IONPs as only one layer was included. Lower particle amounts go along with lower destructive heat quantity. It is, however, more likely that complete carrier destruction is required for big dye-molecules to restore diffusion from the cavity into the cell. To check for the influence of particle concentration, another capsule set with two particle layers and thus increased amount of IONPs (CS B, *cf.* chapter 4.2, table 1) was prepared. The total amount of particles added was 1.84 mg with half for each layer, which represents twice the amount as before. To further raise the concentration of the encapsulated PEI-FITC these capsules were postloaded in addition to the preloading. In this way it was expected to cause a stronger cargo tendency to diffuse and burst out of the carrier during magnetic heating if small shell fractures appear. Unfortunately, the resulting carriers were as stable as the one-layered system regarding both premature and intended release. This suggests that complete destruction is necessary for big cargo molecules like PEI-FITC.

### 4.3.2 Simultaneous CO<sub>2</sub>-Generation

As a dye-change did not result in increased opening it was thought of different approaches that still abstain on heat-shrinkage. Based on reports mentioning enhanced drug delivery through the generation of carbon dioxide bubbles inside liposomes<sup>124</sup> it was thought of transferring this idea onto the present polymer capsules. Heating of the particles should, in addition to the disruption of the polymer shell, induce decomposition of precursor molecules to form CO<sub>2</sub>-bubbles. In theory, these gas bubbles would help burst the capsules open and enhance the cargo delivery. The principle is shown in figure 14. On position 1, the capsule loaded with both cargo (blue dots) and decomposing component (orange circles) is illustrated. They are encapsulated by the polymer shell (green/red lines) interspersed with the MNPs (black squares). Color of cargo is purposely changed to blue to not only illustrate the independency from calcein or PEI-FITC but also for better distinctness between dye and composing cargo. Position 2 represents the process of irradiation using an external magnet to induce particle heating. In the third step bubbles have already evolved from the orange component in the core part and start to pass the shell – without influence on the cargo molecules. This leads to the final step four where the shell is disrupted and both the CO<sub>2</sub> and the cargo are allowed to exit. For examination, carriers were loaded with dye and coated with Dimethyldidodecylammonium bromide (DDAB). This

lipid was functionalized with a hydrogen carbonate (HC) compound beforehand. HCs are well-known to form  $\text{CO}_2$  at sufficient temperatures in moderate regimes and even made their way into the food industry.<sup>125</sup> The lipid represented the barrier to ensure confinement of the  $\text{CO}_2$ -delivering component (and the cargo) inside the capsule since heat shrinkage had been removed from the protocol. Also, reducing size by heat would have been critical here as such temperatures might have induced the disintegration of the HCs simultaneously. Ammonium- and sodium hydrogen carbonate (AHC and SHC) were used as the decomposing chemicals due to their dioxide production at moderate temperatures around  $40\text{ }^\circ\text{C}$ .<sup>124,126</sup> This temperature range was expected to be attained locally inside the shell during field irradiation. The underlying concept was to heat the shell and decompose the  $\text{CO}_2$ -forming chemical concurrently for an enhanced destruction effect. Different concentrations for both chemicals were tried with two capsule types having either one or two iron-layers. PEI-FITC was used as cargo dye due to its big size, which resists diffusion through the capsule pores. The four capsules (CS C to CS F, *cf.* chapter 4.2, table 1) were then compared regarding stability and release behavior inside MCF-7 cells.

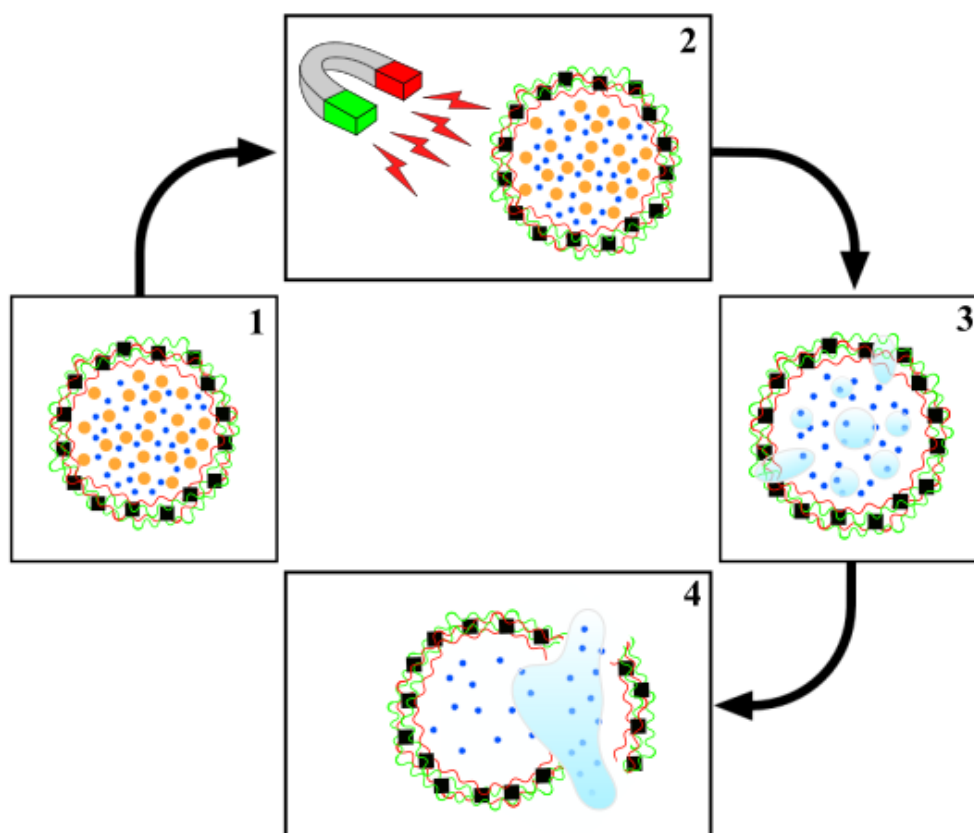


**Figure 14:** Principle of bubble-generation for a boost in cargo release. The idea was to increase release by production of  $\text{CO}_2$  in a four-step mechanism. Capsules loaded with precursor molecules and cargo (1) are irradiated by a magnet (2) to form bubbles (3), which help burst the polymer shell (4). Modified from [124].

For the low concentration systems ( $C_{\text{hydrogen carbonate}} = 10 \text{ mg/mL}$ ) the capsules were showing strong fluorescence and no leaching was observed inside the cells. This includes the one- and two-layered systems. Consequently, stability was once again brilliant. Moreover, the usability of PEI-FITC as dye was confirmed. Possible weakening interactions between HC and dye seem to be neglectable. Nevertheless, no release was observed for any of these carriers when irradiated magnetically (*cf.* figure 15 for AHC results). Despite field presence, capsules remained perfectly stable and no encapsulated dye diffused into the cytosol. Thus, low concentrations of hydrogen carbonate were not sufficient enough to improve release.

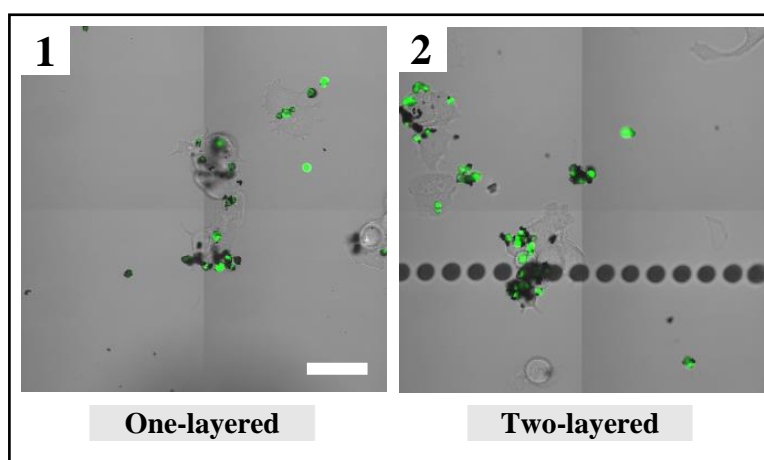


**Figure 15:** **Ammonium hydrogen carbonate-functionalized capsules inside MCF-7 cells after field application.** Polymer capsules functionalized with hydrogen carbonate were tested regarding stability and release inside MCF-7 cancer cells. They differed in their iron layer number and the loaded HC-component. Both shown images represent capsules loaded with ammonium hydrogen carbonate. None of them showed induced release via magnetic heating. Position 1: one-layered system; Position 2: two-layered system. **Scale: 50  $\mu\text{m}$**

This could have had three reasons: 1) the produced amount of  $\text{CO}_2$  was too low and the resulting bubbles were too small/inefficient, 2) the heat induced by the particles was too low and did not cause a decomposition or 3) the gas did just diffuse through the capsule without damage. In case of the first option an increase in HC should be a successful booster due to more/bigger bubbles. The more-concentrated version ( $C_{\text{hydrogen carbonate}} = 100 \text{ mg/ml}$ ) showed similarly stable capsules before field application. However, nearly every cell died under field contact. This could be related to an immense amount of  $\text{CO}_2$  resulting from decomposition, which killed the cells. Such a case would underline the assumption of weak  $\text{CO}_2$ -generation for the low-concentration system (=option 1). Simultaneously, it would refute the other two options as neither particle amount nor capsule structure were changed. Accordingly, no changes were

made on heat quantity or diffusion behavior. Unfortunately, a clear proof is missing for higher concentration as no cells could be recorded anymore. As a consequence of the dead cells release could not be analyzed. Furthermore, free capsules were also rare after field shut-down which prevented insight into release behavior by comparison of capsule fluorescence intensity. In summary, low amounts of HC component suffer disruptive capability while higher amounts cause damage to the surrounding cells. Since the modification in HC-amount of 10-fold was relatively small, it was concluded that adjustment towards a reliable system is complicated. For this reason, further investigation was set aside.

### 4.3.3 Reproduction and Confirmation of the Initial System

#### 4.3.3.1 Back to Heat Shrinkage

As none of the multiple approaches focusing on opening improvement turned out fruitful, it was planned to confirm the possibility of release. For that, two capsule variations were prepared. Their only difference was the amount of IONPs used for the two NP-layers (CS 1 and CS 2, *cf.* chapter 4.2, table 2). Each iron layer was achieved by the addition of either 0.92 mg or 1.38 mg of particles from batch #34. The finalized hollow carriers were postloaded with calcein (3 mg/ml seeding) and subsequently heat-shrunked. By that, the only difference to the original system was one missing outer PSS layer. Both variants appeared stable in water solution as no color change was visible for the supernatant when checked after two days by eye. Certainly, leaching was observed for a maximum of around 16% capsules inside MCF-7 cells for the variant with higher total iron amount and 7% for the lower version. Following release experiments were completed under the standard conditions [ $H = 15.5$  kA/m,  $f = 296.6$  kHz]. The release ratio was roughly calculated to 8% (low) and 0% (high) respectively. Admittedly, these results might not be reliable due to problems occurring with the confocal microscope which led to reduced fluorescence signal and other discrepancies. For confirmation purposes, the tests were repeated under slight modification of the iron amount towards 1.1 mg per layer. This system represented a mean value between both previous variants. Unfortunately, the leaching conduct didn't change and already 16% of the capsule-containing cells were colored before field application. For the control group, which wasn't placed in a field, the amount was even higher (22.6%). Anyhow, induced release was tested and the connected ratio was calculated to around 9%. Basis for the analysis was a total amount of around 27% colored cells for the sample after field influence and nearly no increase for the control group (23%). This suggested that the increase was caused by the field. However, the leaching tendency remained problematic.

#### 4.3.3.2 Reduction to one particle-layer

Based on the leaching tendency of the previous systems, which hampered evaluation of actual release, a small change in the shell structure was applied. One more outer layer (PSS) was added and all NPs were added to a single film in between the polymers instead of separation to two iron layers. This one film contained a massive number of particles being significantly higher than for all previous trials. Functionalization of capsules by confining a huge number of particles to a single layer was successfully done by others previously.<sup>12</sup> To ensure adsorption of all IONPs, one positive polymer layer was replaced by a stronger-positively charged polymer called poly(acrylamide-*co*-diallyl-dimethylammonium chloride) (P(Am-DDA)) which has been reported to enhance the attachment of negatively charged magnetic nanoparticles.<sup>12</sup> This should also include the IONPs used here. Those were added after finalization of the P(Am-DDA)-layer and the general protocol to induce accumulation was applied. In detail, 15.65 mg particles were thrown in to form an intense particle layer (CS 3, *cf.* chapter 4.2, table 2). The stronger charge did, however, not cause attachment of all NPs. On the contrary to literature, the resulting capsules were surrounded by many free particles. This might be proportionally explainable by the size differences of the IONPs in comparison to the reported system. The present nanoparticles were significantly bigger in diameter. As a result, the maximum surface number of particles per capsule might be reduced and all additional particles remained unbound. Certainly, due to the immense number of free NPs, other factors need to be implicated as well. When added to the living research platform, several cells didn't survive the uptake of these capsules. Others were filled or surrounded by immense amounts of free NPs. In addition, multiple cells were colored green prior to any field application due to strong leaching of the capsules. Both the free particles and the leaching can be observed in figure 16. This image presents a field-free condition 24 h after addition of capsules. Usually, cells appear predominantly transparent in the phase contrast image. The presented ones, however, are mainly black due to the NPs. In the enlarged image below, the presence of free IONPs is visible even better. The calcein image shows multiple colored cells linked to leaching events. One leaching event is shown more detailed in the bottom row. To conclude, high particle number confined to one layer didn't amend the results. On the contrary, it impaired them. Not only did many NP move freely in solution, but capsule stability also dropped significantly and some cells even suffered damage. Consequently, this approach was declared as unserviceable.

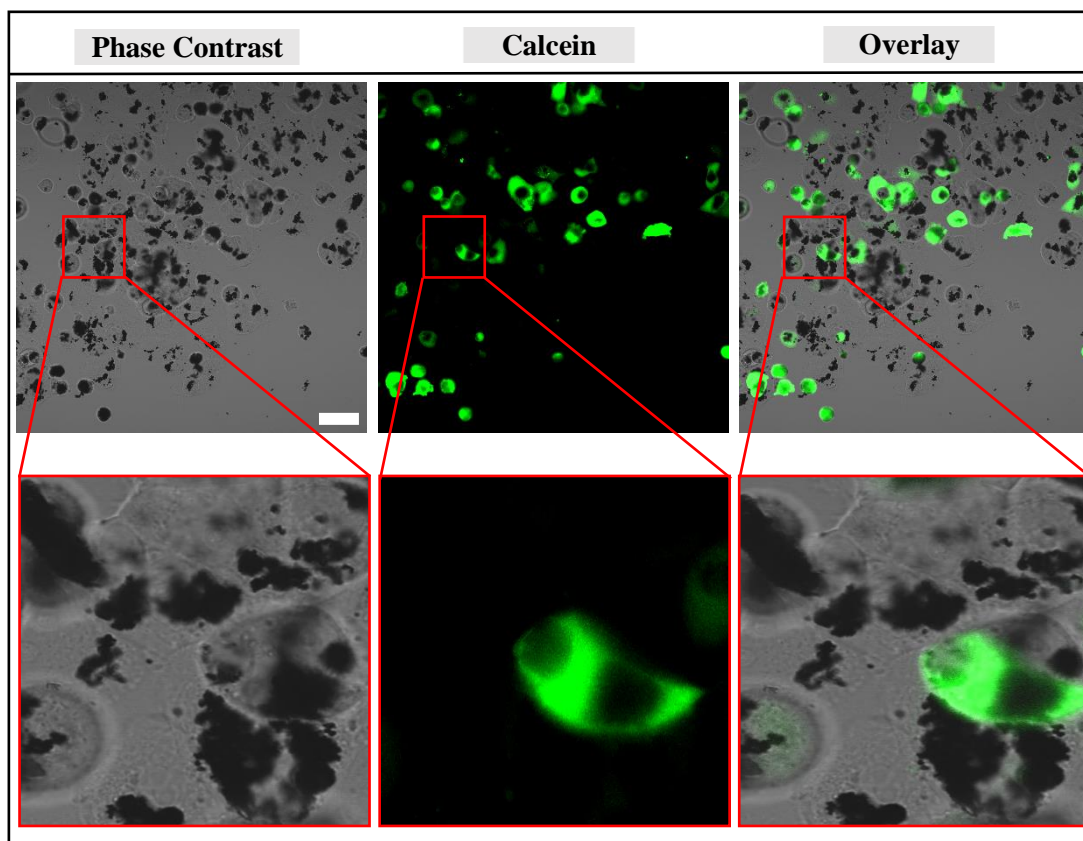


**Figure 16:** **Capsules surrounded by many free NPs.** By replacing one shell polymer by an alternative, which offers enhanced particle-attachment, it was tried to improve the opening efficiency. However, many particles remained unbound and the leaching ratio was high. **Scale: 50  $\mu\text{m}$**

#### 4.3.3.3 Heat Shrinkage with additional outer layer

Restoration of the two-layer structure for the magnetic species inside the shell and addition of the outer polymer layer was the next approach to restore minimal leaching conditions. Structure and composition were copied from the mean system used in chapter 4.3.3.1, but one outmost PSS-layer was appended to increase shell density and improve stability (CS 4, *cf.* chapter 4.2, table 2). After loading with calcein (3 mg/ml seeding) and heat-shrinkage at 70 °C the capsules were added to MCF-7 cells, which were seeded inside a grid petri dish beforehand. Analysis showed that only a very small amount (3%) of capsules showed premature release after uptake. This represents a clear improvement of stability in comparison to all previous calcein systems presented here. During the release experiments [ $H = 15.5 \text{ kA/m}$ ,  $f = 296.6 \text{ kHz}$ ] the release ratio dropped in return. It was calculated to around 1.2 % which is significantly below previous ratios of for instance 9 %. Fortunately, the grid dish enabled the direct observation of the same cell before and after field application, despite the transport towards the field and back to the

microscope. In this way the release from the capsules by magnetic heating was directly monitored for some cells. Four examples for this process are illustrated in the following figure 17. It is clearly noticeable that the green fluorescence spreads into the cytosol only after field contact (bottom row) while remaining confined beforehand (top row). Moreover, there is evidence that the sufficient release is not connected to the number of capsules per cell. On the contrary, there are either one (position 2) or multiple (position 1) capsules present in the shown cells. And for both cases release takes place. These specific capsules seem to react better to the field than those without opening. This could be based on, for instance, a higher particle number per capsule, weaker attraction between the polymers or individual particles with stronger heating efficiency. The exact explanation cannot be gathered from these images.

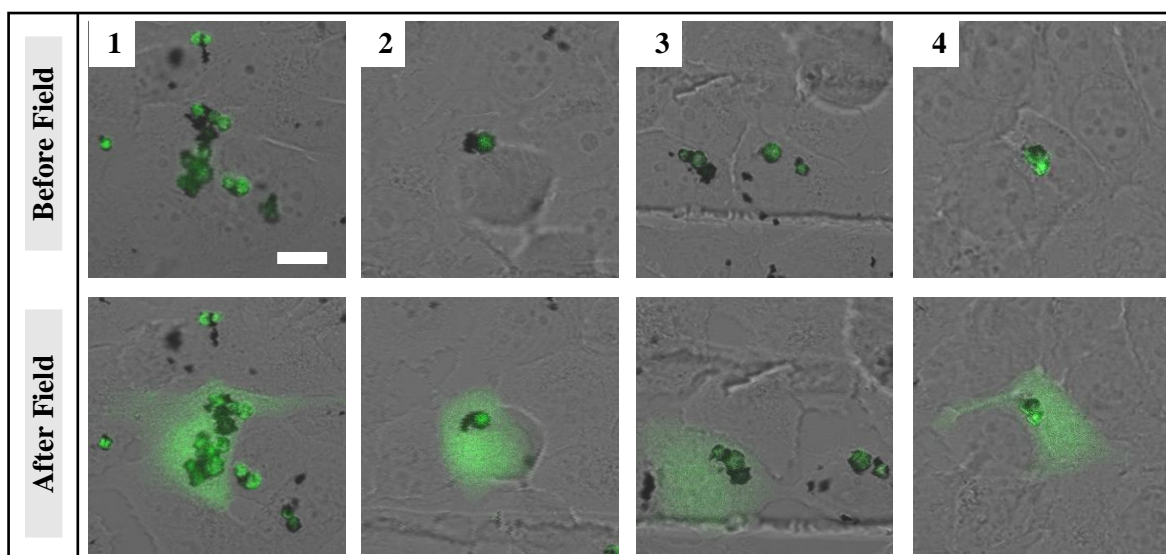


**Figure 17:** **Four successfully opened capsules.** By use of a grid petri dish it was possible to directly monitor the release of dye from capsules into the cells. It can be seen that the green fluorescence only spreads into the cytosol after field application. This secures the successful release *via* magnetothermal heating.

**Scale: 10  $\mu\text{m}$**

#### 4.3.4 Introduction of High-SAR Particles into the System

With availability of the particles #45, #77 and later on #80, offering outstandingly high SAR values of up to more than 2,300 W/g, the tests were redone. An increase in release percentage was expected because of their higher heating ability under identical AMFs. In theory, this should lead to more local heat inside the capsule shell, going along with higher tendency to disrupt it. Four different capsule sets were prepared initially. Two were based on particle #45 (*i.e.* CS 01 and CS 02) and two relied on particle #77 (*i.e.* CS 03 and CS 04, *cf.* chapter 4.2,

table 2). The only difference between capsules with identical NPs was the number of iron layers being either one or two.

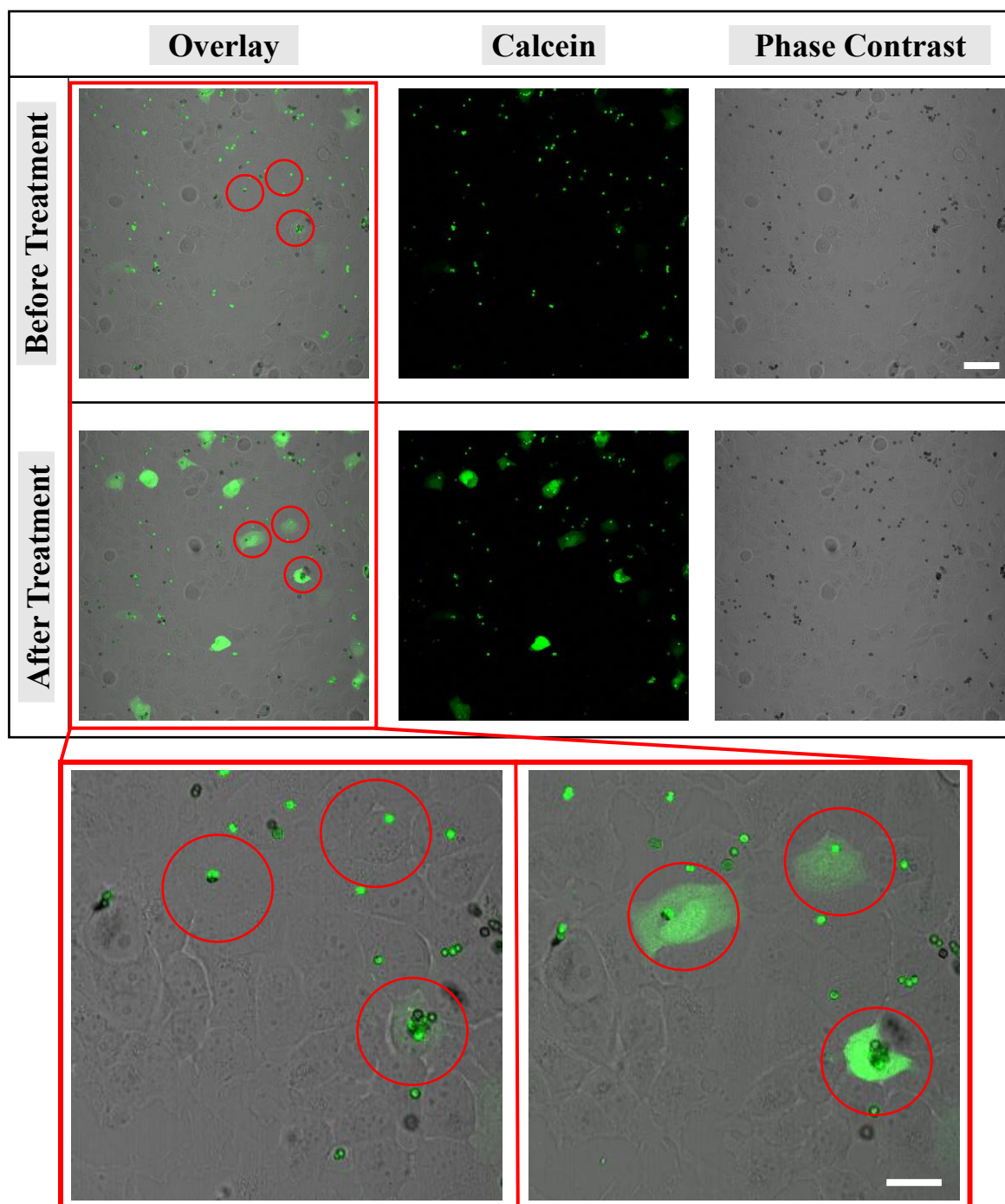


**Figure 18:** Successful release of dye from several capsules through magnetothermal heating. Multiple capsules (CS 01) were simultaneously opened inside MCF-7 cells by application of a magnetic field [ $H = 15.5 \text{ kA/m}$ ,  $f = 300 \text{ kHz}$ ] for 1 h. The overlay images are shown enlarged in the red box below. Therein, the situation before treatment is shown on the left while the image from after irradiation is presented on the right. **Scales: 50  $\mu\text{m}$**

Both HeLa (200k per dish) and MCF-7 (300k per dish) cells were exposed to all four capsules at a rate of two per cell overnight. The release was evaluated by record of specific grid positions inside each dish before and after field application. Irradiation was set to a specific time period ( $t_{\text{HeLa}} = 45 \text{ min}$ ,  $t_{\text{MCF-7}} = 1 \text{ h}$ ). Field amplitude ( $H = 15.5 \text{ kA/m}$ ) and frequency ( $f = 300 \text{ kHz}$ ) were identical for all trials. Multiple examples for successful release were recorded during these tests. Some examples recorded for capsule CS 01 in MCF-7 cells are presented in figure 18: By comparison of the phase contrast images before and after treatment, insights into cell viability are possible. As no changes in for instance cell conformation or cell number are noticeable, viability can be considered unaffected. However, the green fluorescence intensity explicitly changed with field application. For several capsules, field treatment effectuates an increase in expanse of the green calcein signal from a confined situation inside the capsules towards additional space. This fluorescence spread is directly related to a magnetically triggered release: Under absence of an AMF the capsules were stable and no transfer of dye through the shell was possible. As soon as the field was turned on, diffusion was restored. The overlay images provide information about the exact space occupied by fluorescence at any time. It is clearly identifiable, that calcein diffused from the capsules into the surrounding cells and completely colored them as soon as irradiation took place. As a side-effect of cytosol occupation, an increase in fluorescence intensity can be observed. Cells with successful opening appear brighter as the capsules, which carried all the corresponding fluorophore beforehand. This phenomenon can be explained by self-quenching at high dye concentrations inside the capsules. For disrupted capsules the space and volume occupied by dye increased while concentration decreased. As a consequence, quenching ceased and the intensity ascended. The red box in figure 18 provides enlarged overlay images of the same cells for a better visibility. Three specific capsules with fruitful release (red circles) are presented with higher magnification. Especially the fluorescence spread from capsule into the cell cytosol is clearly noticeable after field application. At the same time, no damage on the cells is determined. Admittedly, several capsules inside neighboring cells do not deliver their cargo, despite the same field applied. Complete release across all capsules irradiated remains unattained. Overall, release was observed inside both HeLa and MCF-7 cells for all four capsule types. These results once more confirm the possibility of capsule opening by magnetism inside living matter. However, the results were not consistent. During repetition of the experiment identical capsule types exhibited different release ratios. Sometimes no capsule opened at all. Else, the release was locally strangely high but completely absent on different grid positions. Thus, despite better NPs, exact reproducibility remained unmatched.

### 4.3.5 Longer/Multiple Irradiation

To this point, the duration of field treatment to the cells and capsules was capped at a maximum of one hour. Impact of longer irradiation time was not tested. To investigate the effects of prolonged field presence, two approaches were tried: The first approach dealt with significantly extended permanent illumination over a duration of 4 h. The second one consisted of multiple treatments for a total duration of 3 h, with several checkup breaks in the meantime (after 0.5h, 1h and 2h of total time). Especially the second approach was designed for a more detailed evaluation of the time influence. By observation of the cells at multiple time spots the determination of a specific duration with improved release should be enabled in case of its existence. A one-time assessment after 4 h, on the contrary, just allows for comparison of opening ratios with the original duration of 1 h. This principle doesn't give information about specific time points in-between. Apart from the time all other parameters were kept similar to the typical trials for both approaches. These include cell number, dish type, field strength and frequency, capsule-to-cell ratio (2:1), and position inside the field. Resulting outcome was analyzed by fluorescence microscopy with the available LSM 880. For the sample which was constantly irradiated for 4 h no mentionable improvements or changes were noticed. Release ratio was still of low percentage while cell health was kept equally fine. This suggests that longer, continuous placement of the magneto-responsive carriers inside the same AMF does not favor a boost in opening. Capsules without any release after one hour are most-likely to not show any disruption if farther irradiated by the same field. While these results are not gratifying, this leastways represents a benefit in terms of maintaining cell health: Even if the applied fields don't affect viability, long stays outside the incubator would, due to strong discrepancies of environmental conditions in comparison to the culturing conditions. An interesting observation was, however, made for the samples treated multiple times. Some capsules that remained stable at early check-ups did surprisingly open at later stages. One example for such a case is shown in figure 19. While still unreleased after one run, the cargo did occupy the surrounding cell with the second step and remained detectable with further time (green square). So, release was not present after 30 minutes but took place during the next half hour until recording after 1 h of total irradiation. While longer continuous field contact was eliminated as a source for better opening beforehand, this specific release requires a different explanation. This capsule might have already suffered some damage during the first application. And with secondary (and longer) field contact the damage was intensified and diffusion restored. But due to absence of such cases in the non-stop long-time trials other reasons are more plausible.

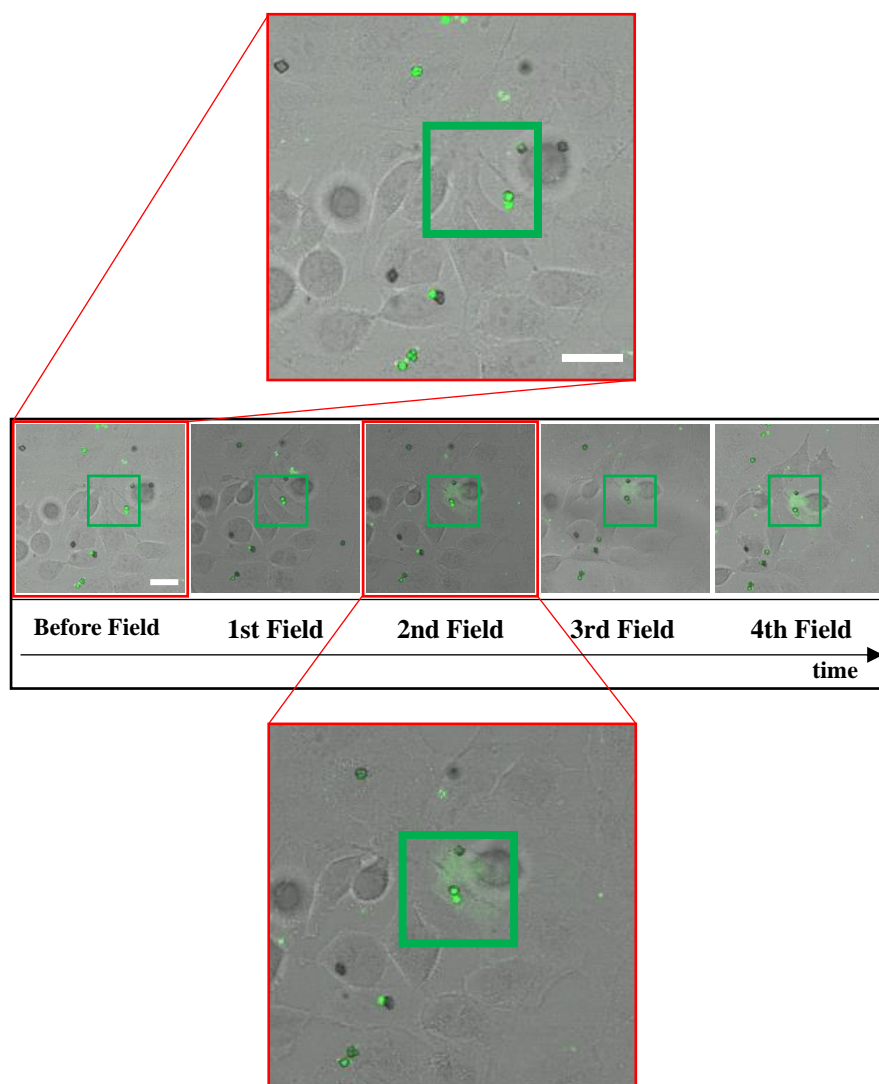


**Figure 19: Observation of capsule opening during multiple field applications.** To evaluate the influence of longer application time the system of capsule and cell was irradiated for a total time of 3 h with three checking breaks after 0.5 h, 1 h and 2 h of the total time. Indeed, some capsules did only show opening after multiple field runs. One example, where release appeared during the second run, is shown here. **Scale: 20  $\mu\text{m}$**

One big difference lied in the movement of the sample towards the microscope inbetween runs. External influences (and contamination) were no longer excludable. But because of the minimal number of cases similar to the presented one and no drop in cell viability this cause is unlikely. Small differences in positioning on the coil set between runs could have been another consequence. The used fields were not 100% homogenous and deviations across the coil sets were not precludable. If the dish position was changed between consecutive runs there are odds of field divergences. Capsules that had contact to lower field parts initially could have moved to stronger field areas. Even slight increases might have sufficed to induce the desired amount of heat needed to burst carriers open. Especially if they were already cracked slightly. The

collected data does not allow for confirmation of this thesis but field variations are more favorable than longer irradiation. Hence, for future tests the AMF duration was not increased.

#### 4.3.6 Release Evaluation by Flow Cytometry

The main disadvantage of the previous tests was the number of cells checked during one run. Even though observation under repeated fluorescence microscopy offered a direct look on the cells, recording several positions did cost a lot of time and the total number of cells was limited. Moreover, the opening and release had to be evaluated manually by picking out specific cells and comparing them across the treatment. Flow cytometry (FCM), on the contrary, allows for automatic analysis of several thousand cells in a small time period. It just requires a really big amount of cell-capsule systems. For that, HeLa cells were incubated with loaded capsules inside an Eppendorf tube (eppi) or Falcon tube (falcon) overnight under constant rotation. In this way uptake was induced due to continuous contact of cells with carriers moving around them. By decrease of residual air bubble amount inside the tubes damaging side effects due to shear forces were minimized. Shortly before examination, the system was then taken out and transferred to the magnetic field apparatus. A strong field ( $H = 29 \text{ kA/m}$ ,  $f = 487 \text{ kHz}$ ) was applied for a specific time span. Initially, capsules and cells were incubated at a ratio of 1:1. Irradiation was carried out for 10 min with a short shaking break at half-time. Directly after field shutdown, the cells were moved to the cytometer and tested for strong fluorescence due to release from capsules. Usually, several thousand cells were tested during one FCM run, whereas prior tests included only hundreds. The analyzation process is shown in figure 20: At first, cell debris and free capsules (*cf.* figure 20-A) were gated out. These organic waste rests from dead cells are located in density regimes with low forward- and side-scattered area (*cf.* figure 20-B) which helps identify them easily. They are marked in the bottom left corner of the graphical display of side-scattered (SSC-A) versus forward-scattered area (FSC-A). From the remaining cells in this plot the majority (black ellipsis) was transferred to the second gating step. By comparing width (FSC-W) and area (FSC-A) of the forward-scattered signal conclusions regarding single and doublet cells can be drawn. Single cells, which represent the desired constitution, come along with significantly smaller width and area, which locates them in the regime closer to the y-axis (black rectangle). This rectangle represented the final population for analyzation. Cells were recorded until this population included  $\sim 10,000$  cells. The fluorescence intensity for these gated cells was recorded (*cf.* figure 20-C) and represented the crucial parameter for release.

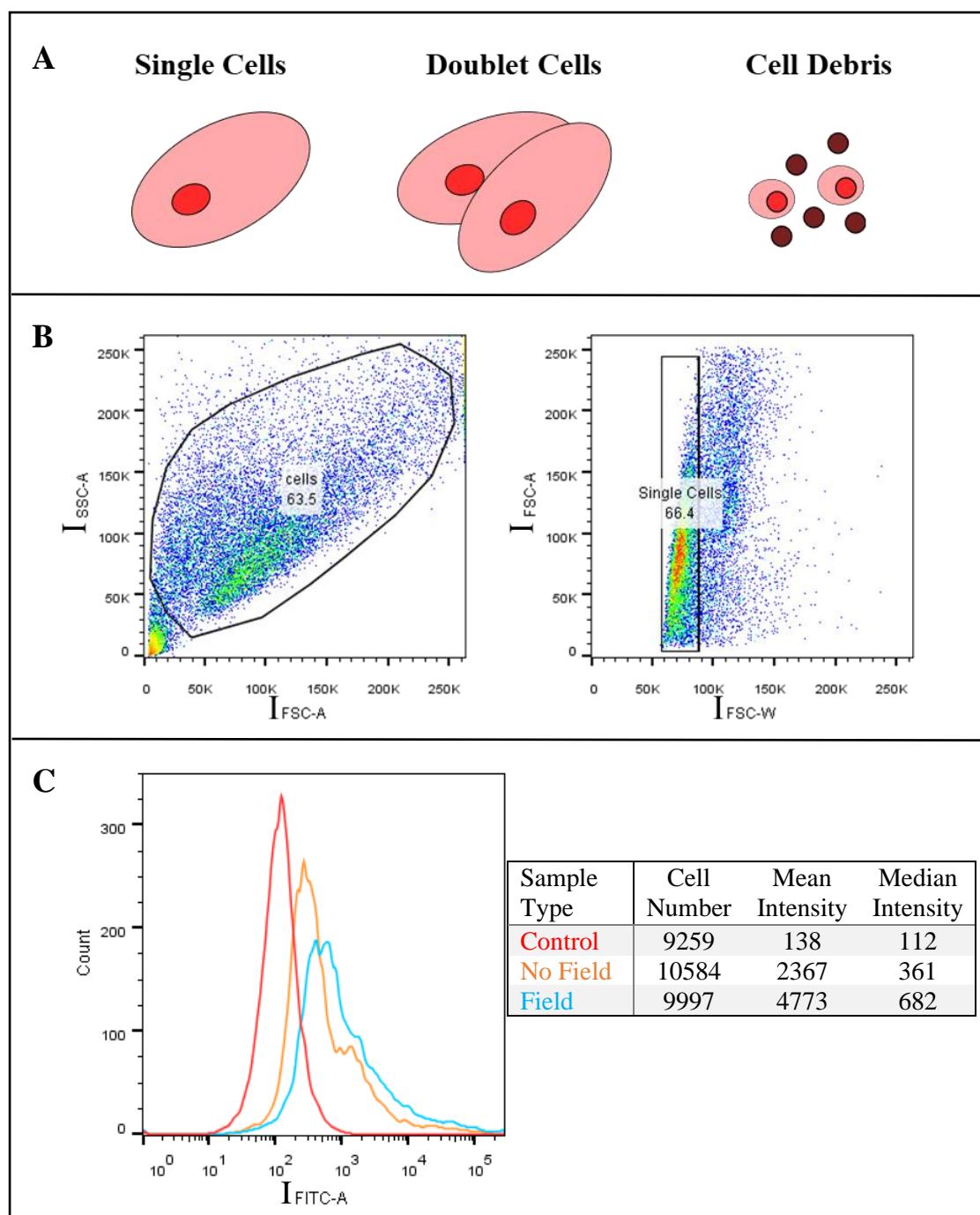


**Figure 20:**

**FCM gating process and data output for opening tests of capsule 02 in HeLa cells.** Several thousand cells were incubated with capsules and the release was analyzed by flow cytometry. **A:** Dead cells/cell trash (=debris) and doublet cells were initially divided from single cells. **B:** From the left intensity plot, showing area dependence between side and front-scattering, the debris data (bottom left corner) was gated out. Only the cells inside the black ellipsis were further treated. In the right plot (area vs. weight of front-scattered signal) the analyzed cells were reduced to single ones (black rectangle). **C:** Around 10,000 of such cells were analyzed after either being placed inside an AMF or not. Cells with neither capsules nor field represented the control. The corresponding fluorescence intensity was recorded. Cell number and intensity values are listed in the table. For the field sample the highest values were recorded which connects to dye release under AMF contact.

The fluorescence was compared for three different constitutions: Systems with and without previous field contact represented the main subject. Capsule-free cells were used as a control. Due to quenching effects at high concentrations, the fluorescence intensity is suppressed if the dye is confined inside the capsules. As soon as cargo release appears, confinement and quenching are stopped, which leads to an increase in fluorescence. Non-stable capsules with premature release strongly affect this comparison as the intensity increases equally. Nevertheless, leaching appears for both capsule-samples at similar rate which cancels out the effect. Based on previous outcome from fluorescence microscopy a total of five promising capsule types (CS 01 – 05, *cf.* chapter 4.2, table 2) was chosen for release tests using FCM. The new results, however, strongly varied between those different capsules. Some offered strong increase in fluorescence intensity after field irradiation whereas others didn't. Unfortunately, for capsule CS 01, which was working quite well in former tests and has been shown in earlier chapters with successful opening (*cf.* figure 18), no results could be recorded due to cell death. On the contrary, capsule CS 02 offered excellent release. Its fluorescence intensity significantly climbed inside the analyzed cells when irradiated magnetically. Its outcome is presented in the subfigure C of illustration 20: The red graph represents the control sample with pure cells. Some fluorescence, caused by the cells themselves, is present but the intensity is very low. In contrast, the two other graphs are shifted right on the horizontal axis to more intense regimes. The blue one corresponds to the field sample and the orange to the one without field contact. The shift of the orange peak is related to the pure presence of intact capsules with encapsulated fluorescent cargo. The higher values for the blue peak indicate that several capsules delivered their cargo into the cytosol and quenching disappeared. The comparison of mean and median intensity confirms this thesis as both values are doubled for the field sample. For the three other capsule types (*i.e.* CS 03 - 05) the shift differences between both test samples were nearly neglectable, which indicates that the release ratio was really low or even zero. Only capsule CS 03 had a slight increase under irradiation as well. To guarantee that the intensity increase shown for the field sample in figure 20 was not a one-time actuality, the experiment was repeated three times. For each try the same conditions were used for field, time and capsule to cell ratio. The results are shown in figure 21. The exact outcome under illumination was individual for each operation, but all four trials clearly showed a surge in fluorescence related to the field. The overall intensity-drop for later runs might be caused by the time shift between the tests and the corresponding loose in encapsulated calcein inside the capsules due to leaching. Moreover, capsules might have undergone photobleaching due to light contact. In addition, slight differences probably also result from discrepancies in the number of capsules present,

which was calculated on basis of 10  $\mu\text{L}$  solution and extrapolated. Variations in opening tendency in-between runs also rely on intrinsic stability differences between capsules from the same batch. Those arise from for instance variances in exact particle amount attached to the individual shell of each capsule, which influences the specific heat produced per capsule. The added tables, which include mean and median values, provide confirmation of magneto-responsive opening. For all runs at least one value of the field sample exceeds the other two conditions. Even though the rises are not as immense as for the first run, the trend remains.

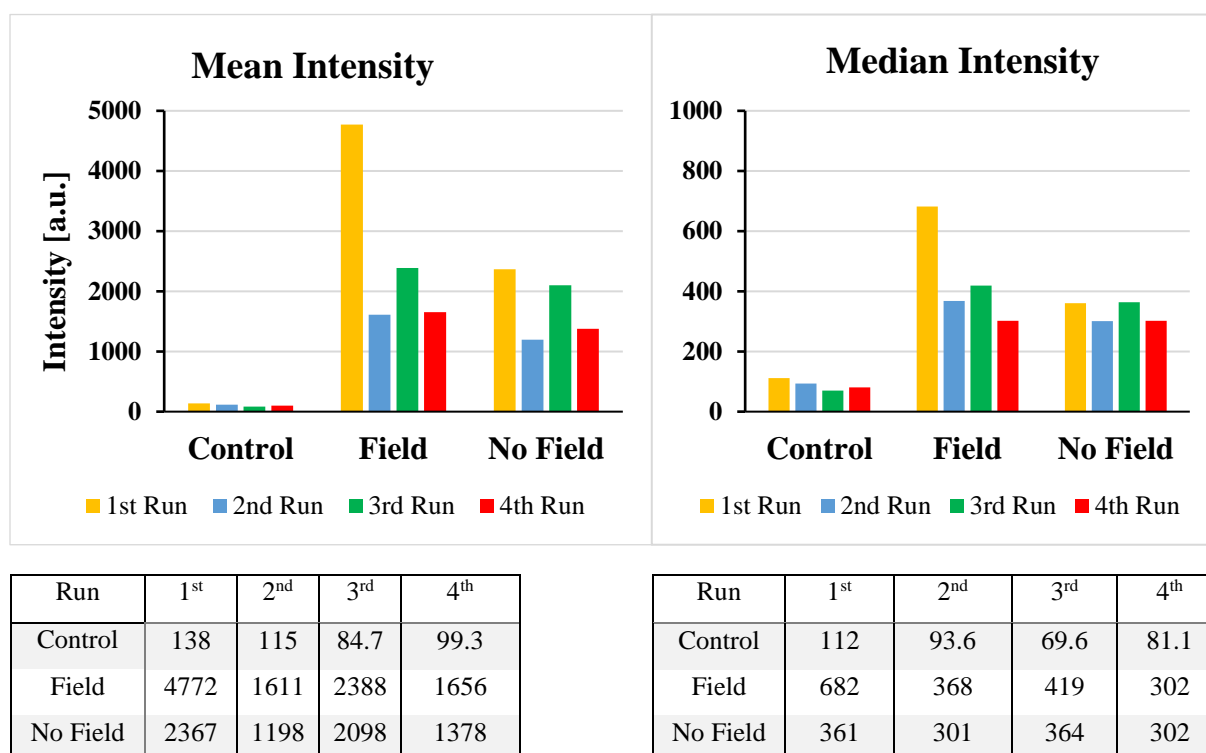


**Figure 21:** Intensity diagrams for repeated FCM measurements of capsule CS 02 in HeLa cells. Fluorescence was recorded for cells inside and outside the field. Capsule-free cells were used as control. Increased intensity for the field sample corresponds to successful release from capsules. Values are listed in the tables below.

In total, the entirety of this data provided an insight into opening behavior on a significantly larger scale. With several thousands of cells and capsules being analyzed quasi-simultaneously, the number exceeded previous observations immensely. While no exact ratio of disruption could be calculated from the intensity graphs, it could be stated that release occurred for a significant quantity of certain capsules. This suggests that delivery also appeared on locations not observed by fluorescence microscopy during previous trials which showed at least some release in total.

### 4.3.7 Summarized Outcome

Multiple approaches targeting release behavior had been carried out to this point. The detailed processes and results were presented in the previous chapters. This chapter is dedicated to provide an overall view of all results and issues. The following table 3 gives a short summary of all executed trials and compares the observed outcomes and issues.

**Table 3: Summary of all approaches executed during the opening trials.**

| <i>Approach</i>             | <i>Idea</i>   | <i>Outcome/Issues</i>   |
|-----------------------------|---|---|
| dye change                  | replacing heat shrinkage by dye too big to cross shell  | 0 % release, big dye size might require complete shell disruption                                   |
| CO <sub>2</sub> -generation | shell burst by simultaneous bubble generation           | 0 % release at low concentration, cell death at higher concentration                                |
| reduction to one NP-layer   | use of single particle-layer w/ immense IONP-number     | many free particles, drop in cell viability   |
| additional outer layer      | restoration of stability by additional polymer layer    | release lower than for original system but directly recorded, stability restored                    |
| high-SAR particles          | release-increase by addition of high-SAR NPs into shell | release recorded but not improved, reproducibility problematic                                      |
| longer/multiple irradiation | application of AMF for longer/multiple times            | no changes for longer duration, some additional releases w/ multiple runs                           |
| Flow cytometry              | use of FCM to increase number of analyzed cells         | analysis of ~10,000 cells per run, release also visible on bigger scale, no direct ratio calculable |
|                             |   |   |

## 4.4 Heating Evaluation

So far, several attempts to boost release and minimize leaching of the present magneto-responsive polymer capsules were worked out and evaluated. However, in neither case release values above 10 % were observed. This might be due to several intrinsic reasons: 1. the heating achieved by the best particles lied below the limiting boundaries; 2. the coating used caused a drop in heating which is too significant; 3. heat shrinkage or the coatings applied resulted in unavoidable stability - to name just a few. However, it could also be based on

external factors. Especially the alternating magnetic field which irradiates the sample bulks large. On the one hand it is limited to maximum strengths if used in biomedical application. In this way unintended side effects are indeed minimized but the maximal heating is also restricted. On the other hand, the fields do not always radiate uniformly through the sample. In the special case of the fields used here this factor has significant influence. Inside the calorimetry coil set, which was for instance used during the flow cytometry measurements, the homogeneity is given as 90 % across the sample.<sup>[d]</sup> For the planar coil set (PC<sup>90</sup>), the parameters strongly depend on sample size. As the small plates were always positioned in the center part, it can be expected that they were localized inside the region marked with 90 % homogeneity.<sup>[e]</sup> Both these values signalize that differentiation of AMF across the specimen is still present. Moreover, even the heating of the best particles underlies weakening effects when confined to a polymer shell instead of being “free” in solution. The thermal conductivity drops with polymer coating and MNPs in close contact undergo dipol-dipol interactions.<sup>12</sup> Both factors mitigate the maximal heat transfer onto the shell and impact its degradation.

With respect to these factors it was no longer focused on the release tendency itself. Quite the contrary, it was tried to pick out the heating behavior and evaluate its insufficiency to cause shell disruption on a larger scale. The easiest way of classification lies in comparison with a system working fine in terms of heating. Laser-induced opening, which shows excellent delivery characteristics, was chosen for comparison purposes. Both strategies acquire heating mechanisms to disrupt the capsule wall and release the cargo. But magneto-responsive tests seems to lack success in release, whereas photothermal opening has optimal yield. At baseline it was thought about techniques to measure temperature synchronous with laser or field irradiation. Infrared cameras represent an instrument to record temperature distribution across a big area over time. By positioning the camera directly above the dish, examination of the whole collection of seeded cells before, during and after field contact was intended. Ideally, temperature peaks induced by particle heating inside the capsule shell would then appear as hot points across the sample due to significantly higher degrees at capsule sites in comparison to surrounding areas. Practically, the D5 series, which has been used for generation of the AMF, included an IR-camera (Optris Xi 400) as accessory. The connected setup can be viewed in illustration 22. While the dish containing the sample could be positioned in the center of the coil set, the infrared camera was aligned exactly above it due to the flexible arm. In this way, AMF-irradiation and temperature recording could be carried out at the same time.

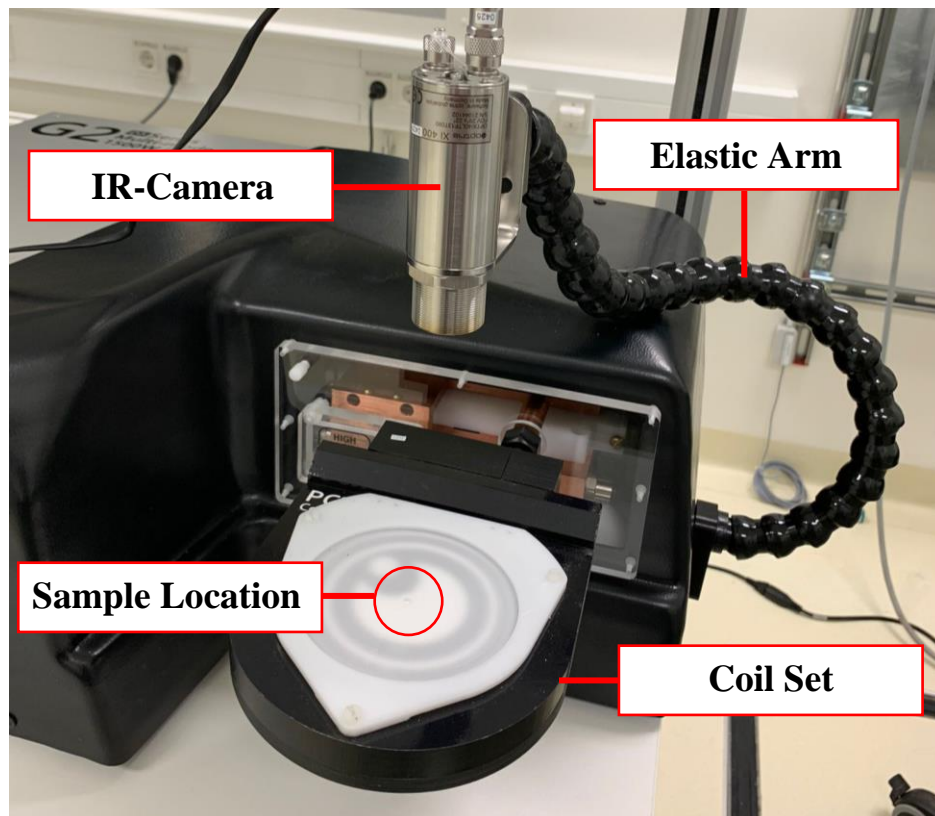


**Figure 22:** **Set-Up for IR measurements inside dishes.** With availability of an IR-camera the measurement of temperature during field application at the planar coil set was enabled. Camera alignment vertically above the sample dish allowed for observation of the whole sample volume while magnetically irradiated.

To confirm accordance of output and real temperature, known objects were recorded first. Typical human body temperature is around 37 °C. Recording body parts should, therefore, display temperatures in a close range around this mean value. The record of a human hand can be seen in the left part of image 23. While the background shows cold degrees between 13.5 °C and room temperature, the temperature trend across the hot regimes ranges between ~30 °C to 38 °C. The cold values arise from the water cooled (but shut-off) coil set below the hand, while the higher T-values comply with the expected values for the body part itself. The small differences across the palm suit the presence of temperature irregularities across the body. Another trial included measurement of water temperature inside a circular dish by infrared imaging and comparison with the output received from an inserted thermometer. The IR-camera gives 46.2 °C at the specific location which is exactly identical with the output on the thermometer screen show in the top right corner. The slight shadow visible inside the dish comes from the inserted needle of the temperature sensor. In both observed cases infrared imaging delivered excellent values. These results validated the calibration of the camera temperature scale and affirmed its sensitivity.

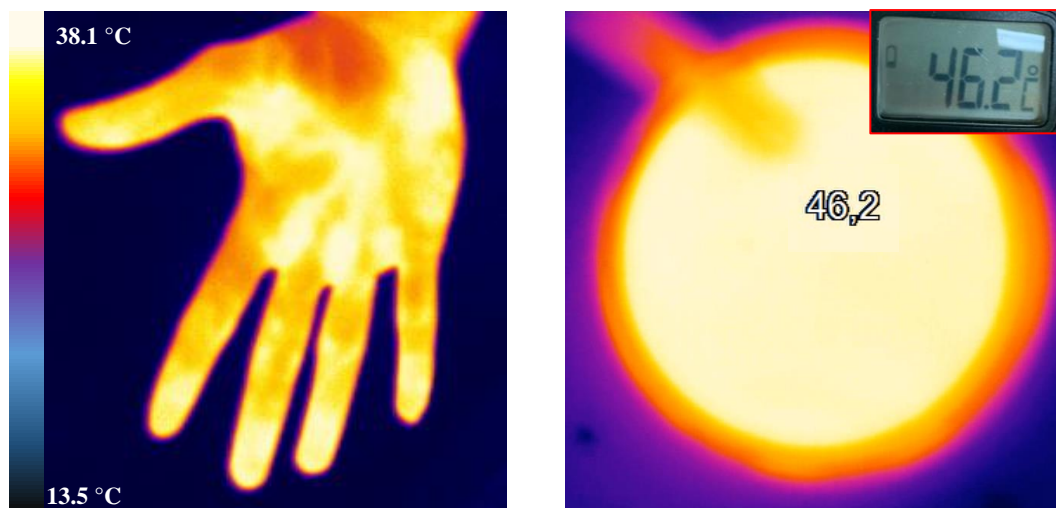


**Figure 23:** Infrared images of a human hand (left) and hot water (right). To evaluate the temperature scale of the IR camera, objects with known temperature were analyzed. The shown hand (left) clearly confirms the correct scale as the body part delivers values around the expected 37 °C while the background is significantly cooler. Same accordance was observed for water (right) when compared to an inserted thermometer.

With verification of the measurement scale, examination of particles and capsules was initialized. In theory, both pure particles and particle-containing capsules should induce temperature rise when magnetically irradiated. This process should be visible under record of infrared radiation due to an increase in solution temperature. For the particles this process has already been confirmed inside the calorimetry coil set during SAR tests, where the values were calculated from  $\Delta T$ . However, the used field parameters for the maximum values ( $f = 487$  kHz,  $H = 29$  kA/m) significantly exceeded the conditions used for cell tests ( $f = 300$  kHz,  $H = 15.5$  kA/m). And the trend was only received from an inserted fiber without direct visibility. For first visible comparisons between the heating behavior of free NPs and their capsule-bound counterpart, both types were added to respective  $\mu$ -dishes. The strong heating sample #77 was chosen as free NPs. Its concentration was set as 32.56 nM ( $\cong 1.5$  mg iron/mL), which complied with the concentration used for SAR evaluation. 1 mL of solution was added to the dish. CS 04 was chosen as the examined capsule type. The whole batch, containing around 66 million capsules dissolved in 2 mL water, was added to the second dish. This capsule was chosen due to high amounts of particle #77 in its shell. It must be mentioned that the total amount of tested free particles exceeds the number present in the shell of the tested capsules. During capsule synthesis a total of 1 mg particles was added. This corresponds to around 66% of the amount inside the nanoparticle dish. A lower real amount of IONPs across all shells is,

however, very likely. Some particles might not have bound to the polymers and been washed away during preparation. The capsule  $\mu$ -dish was, therefore, expected to show lower heating than the one filled with pure NPs.

Initially, both dishes were put under field treatment for 5 min. For that, each sample was placed on top of the planar coil set at the previously mentioned cell test conditions. The original plan was to record only the dish interior without any surrounding area. This procedure was immediately discarded after the first run. Therein, the camera started to get magnetized oneself, due to close contact to the field, and nearly got wrecked. From the second run on, the camera was always kept at least 15 cm apart from the coil set. As a side effect, the recorded area increased. The outcome of the second trial is illustrated below (*cf.* figure 24). It shows the temperature course across the recorded area during magnetic irradiation for both specimens. The value  $T_{\emptyset}$  displays the average temperature inside the marked rectangle named *area 1*. It allows for direct comparison of discrepancies over time. For the pure particles the initial  $T_{\emptyset}$ -value at field activation ( $t = 0$  s) is given as 24.4 °C. It remains nearly constant until 150 s runtime and slightly increases to 24.6 °C at field shut-down ( $t = 300$ s). A similar course is present for the capsules, but the T-values are slightly different. They are given as 24.4 °C ( $t = 0$  s), 24.1 °C ( $t = 150$  s) and 24.4 °C ( $t = 300$  s). So, neither the pure particles nor the capsules generated a clear temperature increase of the surrounding water. In both cases the solution temperature remained nearly constant over time. This issue gives a first hint that strong heating might be hindered anyhow. This could be related to the field parameters and their restriction by the biological limit, which was nearly maxed out. If no visible impact on solution temperature appears in the record of highly-concentrated free NPs, the capsule shells, consisting of significantly less particle number, are highly expected to have even less visible effect at these field conditions. To specifically check for influence of field parameters, similar studies were carried inside a stronger field above the biological limit. This was possible due to delivery of a PC70 planar coil set, which allowed for higher  $H$ -values at a frequency of  $f = 300$  kHz. The field was set as  $H = 300$  Gauss ( $\approx 24$  kA/m). During temperature imaging, the capsule solvent showed a small increase of 1.5 °C whereas the solvent of the free particles heated up for a total of around 6 °C. Even though the rise is not as strong as seen for SAR measurements, where  $\Delta T$  sometimes reached several tens of degree, an increase exists. This effect is significantly lower for capsule-inserted particles. Similar phenomena have been observed during other research projects with magnetic nanoparticles as well.<sup>127-129</sup> The most promising explanation is founded on the immobilization and interaction effect the particles are going through. Typical evaluations of particle heating are carried out in their default aqueous environment.<sup>22,27,129</sup> This matches the

SAR-calculation carried out in the present study: Particles were suspended in water at a specific concentration and the temperature increase was measured to recalculate the corresponding values. Moreover, many underlying theoretical models – like the linear response theory - consider each particle as a free, individual heat source without any interaction to surrounding NPs.<sup>129,130</sup> This assumption, indeed, approximately matches reality for specific cases like MNPs with long stabilizing ligands minimizing long-range magnetic forces.<sup>129,130</sup> But for the majority of cases the particles show interparticle interaction which strongly changes their heating behavior from theory. Observation of interacting particles shows formation of diverse structures and forms including rings and chains.<sup>129,131,132</sup> Such behavior was also present for multiple IONP batches used in this study (*cf.* Appendix). Especially the batches #77 and #80, which represented two of the best heaters, tended to form long chains of NPs in close contact. Alteration of these intrinsic factors strongly varies the resulting heating procedure. During SAR measurements, no external influence on this interaction took place. But with insertion into the capsule shell multiple factors undergo changes. This for instance includes possible chain breaks during attachment of individual particles onto the polymer layers. In this way the magnetic anisotropy of the system and thus the heating behavior is changed drastically.<sup>129,133</sup> In addition, the particle immobilization by means of electrostatic forces significantly reduces the degrees of freedom<sup>129</sup> and might prevent Brownian relaxation.<sup>127,128,130,134</sup> The latter mechanism, thereby, describes a rotation of the whole MNP to align its magnetic moment parallel to the external field (*cf.* chapter 1.3). Significant drops in heating are the consequence.<sup>127,134</sup> This effect can represent regression up to several percent, as observed for example inside hydrogels where 35 % of SAR were lost due to hindrance of Brownian relaxation.<sup>127</sup> Based on these results, influence of particle amount per capsule, as it was for instance targeted in chapter 4.3.3.2, is also unlikely to play an equally-drastic role. The heating will definitely change with variation of particle number per capsule. But to achieve an increase as strong as caused by field raise, the number of additionally-linked NPs would need to be extremely high. This most probably exceeds the maximum quantity linkable to the shell. Once the limit is reached additional particles end up unbound in surrounding medium. By that, they no longer locally affect shell stability during heating but start to show unwanted influence on cell viability (*cf.* chapter 4.3.3.2).

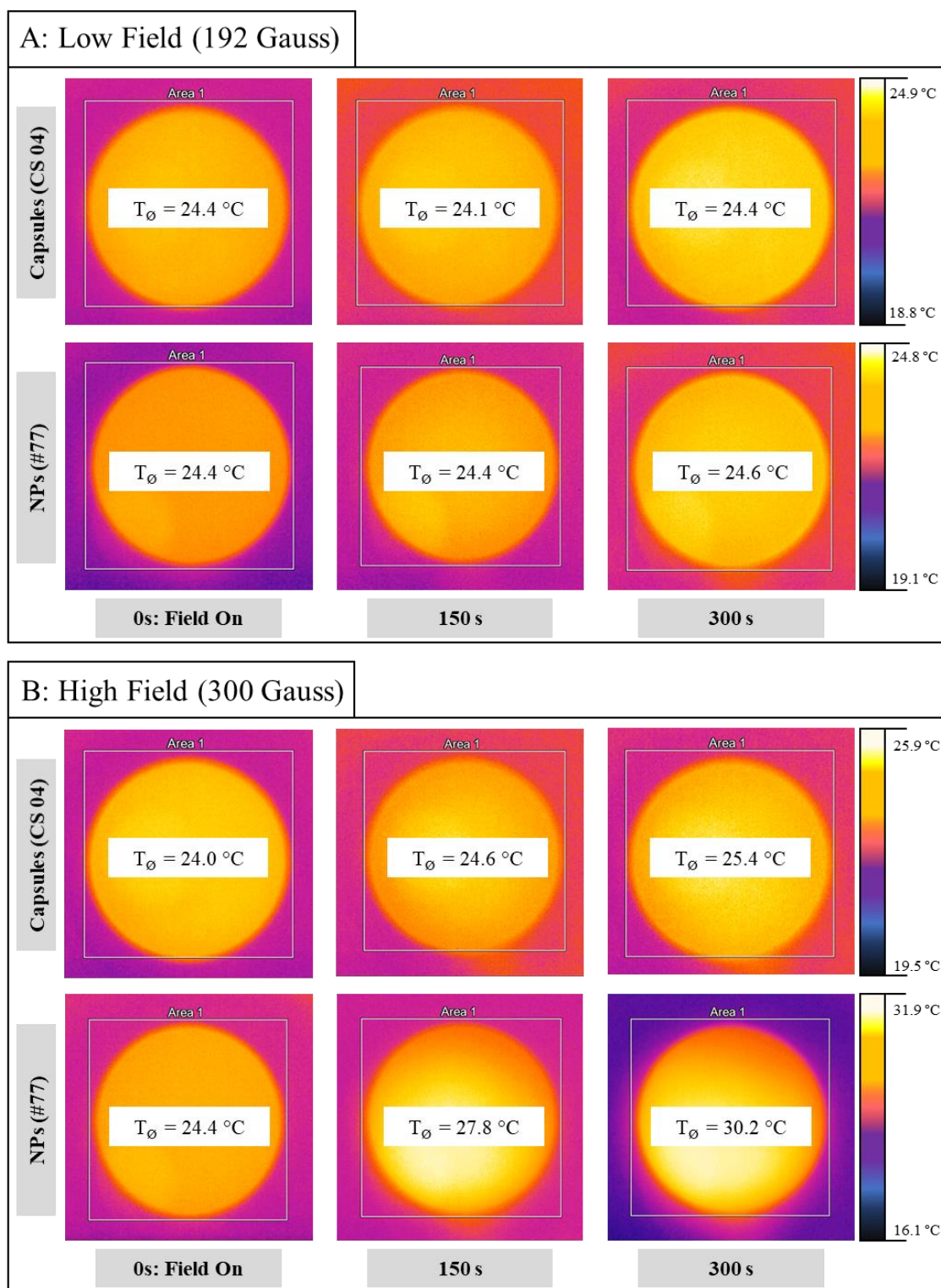


**Figure 24:** Infrared images of pure particles and capsules during magnetic heating. Both pure particles (#77) and capsules (CS 04) were irradiated by an AMF and their heating behavior was mapped by infrared detection across the dish. Two fields at a frequency of 300 kHz were used: 192 Gauss (A) and 300 Gauss (B). Especially the NPs exhibited significant heat signatures when irradiated with the high field.

Previous investigations were only focusing on the temperature course of the particle/capsule-system in water without visible connection to the release. It was clearly pointed out that particles are hindered in heat mediation by immobilization and field restriction. Nevertheless, cargo delivery might still take place for reduced heating. To clarify the actual impact, similar examination needed to be done with focus on cargo movement. Even limited heating might suffice to disrupt the capsule shell and induce cargo liberation. In such a case, secondary reasons caused by cell uptake would constitute the crucial preventers for visibility of *in vitro* release. To review this option, one million loaded capsules were suspended in MilliQ-water. Due to encapsulated calcein, all PEMCs offered a fluorescence signal around the emission peak ( $\lambda_{em} = 514 \text{ nm}$ ). For intact capsules, the dye remained confined inside the cavity of the PEMCs and did not color the surrounding water. But with capsule disruption the cargo was allowed to diffuse into the medium. Analysis of the supernatant, therefore, enabled direct insight into the amount of calcein released. For this purpose, the supernatant emission of the same capsules was measured at three consecutive conditions: 1) before application of any field, 2) after 10 min at 300 kHz and 192 Gauss (=15.5 kA/m, low field), 3) after additional 10 min at 300 kHz and 300 Gauss (=24 kA/m, high field). The resulting emission data is shown in figure 25.

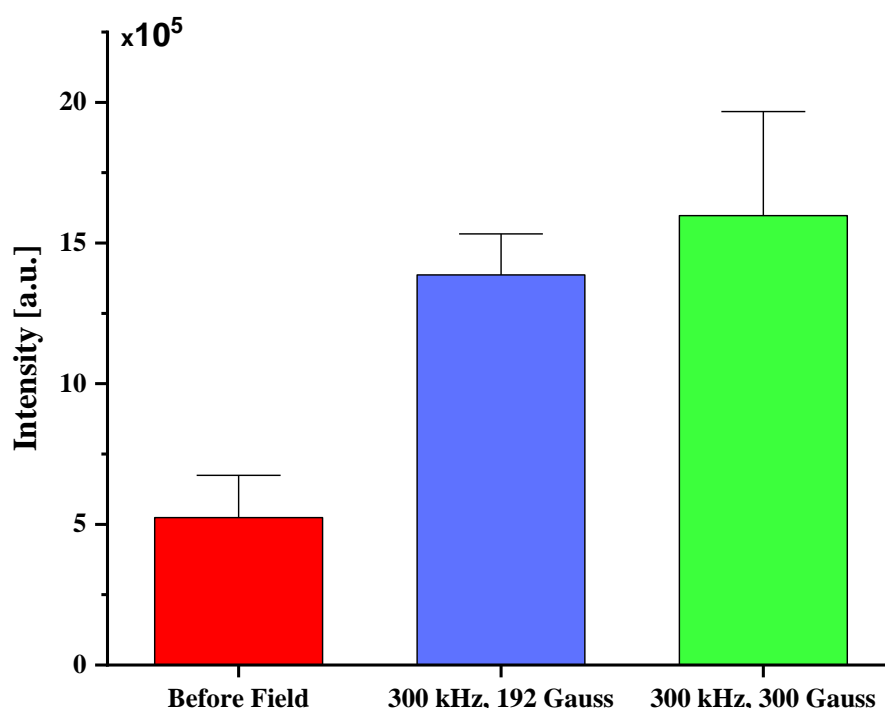


**Figure 25:** **Fluorescence intensity of supernatant taken from the same sample at three consecutive conditions.** One million capsules were dissolved in water and the fluorescence of the supernatant was measured at three time points: 1) before any field, 2) after 10 min inside low field (300 kHz, 192 Gauss), 3) after additional 10min in high field (300 kHz, 300 Gauss).

The three bars are related to the intensity of emitted light at  $\lambda_{em} = 514$  nm after irradiation at  $\lambda_{ex} = 493$  nm. For completely stable carriers, the first bar would equal zero. None of the calcein would diffuse into the surrounding water and still encapsulated dye be removed together with the capsules before analysis. Presence of leaching from some damaged or instable capsule would, however, not be excluded. Hence, some cargo ended up inside the supernatant and caused fluorescence, which explains the small bar before field. The actual peculiarity lies in the two other bars. In relation to the reduced heating capability it was expected to observe at most a minor opening of capsules, especially for the low field. The data, however, shows a strong increase in supernatant intensity, which represents a field-induced cargo movement out of the capsule. The intensity shows a 4-fold rise after field, which approves disruption of multiple capsules during AMF contact. Moreover, this increase already appeared after low field contact and didn't show a subsequent major leap after additional application of the higher field (condition 3). The small rise between the two field states is related to opening of additional capsules during high field irradiation. In this specific case, the heating suppression might have played a critical role by hindering the release during low field. But its proportion of the release entirety is immaterial in comparison to the initial peak between conditions 1) and 2). This clearly contradicts the assumption of heating-related prevention of release inside cells. Already the weaker field was capable of inducing enough particle heat to induce disruption for a large number of capsules. Even immobilization and/or interaction effects on heating seem to not significantly impede the ability. The corresponding behavior at extremely high fields could not be tested here because of technical limitations. Any higher field would anyway exceed the limits for bio-application and be unemployable to cells without damage. As a consequence, other processes, appearing as soon as the capsules are taken up into by cells, must be the protruding reason for release damping.

In all probability, the escape from endosomes/lysosomes represents a decisive factor. After endocytosis, which describes the mechanism of macromolecule transport through the cell membrane,<sup>135</sup> body-foreign substances get in touch with endosomal networks were they fuse with endosomes.<sup>135,136</sup> Based on the network response, which is specific for different molecules, the carriers are sorted and their final destiny is regulated.<sup>135,136</sup> Materials that are selected for degradation are then very likely to be moved towards lysosomes.<sup>135,136</sup> In terms of the polymer capsules the cells response is unlikely to be any different from degradation as no component is suitable for recycling. Therefore, their final location is expected to be late endosomes/lysosomes. Due to their stability, they survive the acidic environment but remain encapsulated by the lysosomal membrane. This means that release from capsules into the

cytosol is aggravated. The cargo then not only needs to surmount the polymer shell but also the membrane around it (*cf.* figure 26).<sup>78,122,137</sup> Since membrane-impermeant cargo dyes were used, this process requires additional damage to the lysosome, which can only arise from the capsule and in specific from the internalized magnetic particles. In this context, the release issues observed during *in vitro* but not during water screening receive a plausible explanation. While particle irradiation delivered comparable amounts of heat in both cases, the power was possibly strong enough to damage many capsules but not their surrounding lysosomal membranes. Consequently, the capsule opening ratio would have technically been satisfactory but concealed by secondary factors.<sup>78,122</sup> Similar concerns were also met during the development of photothermal heating. However, choice of particular particles and lasers helped overcome the topic quite easily.<sup>55,78</sup> For magnetothermal heating, relevance of endosomal/lysosomal escape remains unexamined. Discrepancies in heating strength under either laser or magnetic field exposure at individual standard conditions could help enlighten troubles with magnetothermal release in cells. A significantly lower temperature increase for the magnetic treatment would favor the assumption of unaffected surrounding membranes and corresponding entrapment.

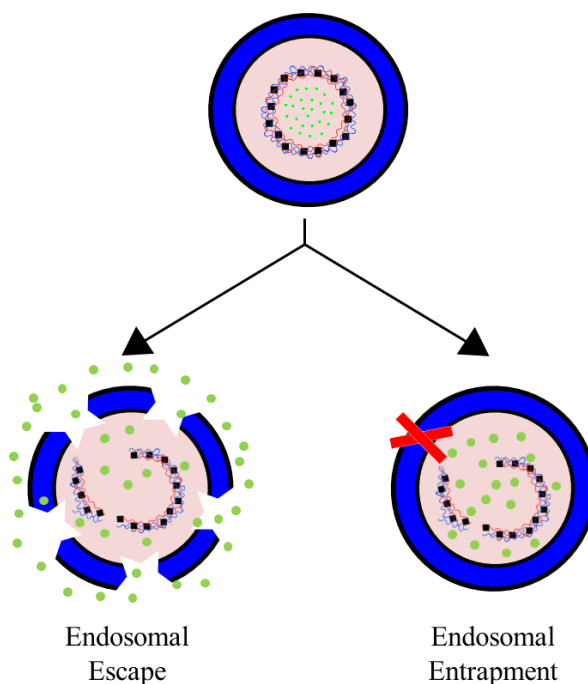


**Figure 26:**

**Endosomal Escape vs. Entrapment.** Capsules ending up in endosomes require a mechanism which allows the cargo to surpass or escape the surrounding membrane. Otherwise the cargo stays entrapped inside the vesicle after opening. Modified from [137].

To clarify this conjecture, the present magnetic system was compared with an excellently working photothermal equivalent. Comparison was performed through detection of sample temperature by means of resulting emitted infrared light during treatment. Examination was no longer carried out in separate attached cells but transferred to three-dimensional spheroids of significantly bigger lateral dimensions. These cell accumulations range around 300 – 500  $\mu\text{m}$  in diameter. This size even allows for direct recognition by eye and was expected to highly improve the image quality of the infrared detector. Single cells would have been too small to resolute. This was especially important for the magnetic part, where short distances between detector and sample were no option due to field damage to the camera. In addition, individual cells usually contained a maximum of two capsules. As these carriers represent the only heat source, temperature peaks would be confined to very small and hard to record areas. In contrast, spheroids comprise of thousands of bundled cells and capsules. When irradiated, the heat of multiple carriers in close contact would add up and appear as a big and bright spot on the detector. Comparison of heat produced by both types of 3D-systems, *i.e.* with either magnetic or plasmonic capsules and under influence of the corresponding trigger, was expected to enlighten differences. Capsules were added during spheroid growth to ensure even distribution of carriers, and thus nanoparticles, across the cell clump. Both kinds of systems were then run at typical conditions. For magnetic tests this included a field strength of  $H = 15.5 \text{ kA/m}$  ( $\cong 192 \text{ Gauss}$ ) as the low field condition and  $H = 24 \text{ kA/m}$  ( $\cong 300 \text{ Gauss}$ ) as high field. Both were operated at a frequency of  $f = 300 \text{ kHz}$ . Irradiation took place for  $t = 15 \text{ min}$  at the PC70 coil set. The time point named ‘max field’ was chosen as the final seconds. The laser tests were run with a green laser ( $\lambda_{\text{ex}} = 532 \text{ nm}$ ). The sample was irradiated from below for a few seconds. Both spheroid types were incubated in cell medium inside individual dishes at similar number. Attachment did not take place. Figure 27 presents the results of the simile. The infrared images in the two upper rows represent data from laser tests. The uppermost line displays the behavior of the dish filled with plasmonic spheroids. They are interspersed with GNR-functionalized polymer capsules at a capsule-to-cell ratio of two. The corresponding nanorods showed a major absorption peak at 940 nm but a secondary maximum located around 510 nm (*cf.* Appendix), enabling use of the green laser. Capsule structure was set as (PSS/PAH)<sub>2</sub>/GNRs/PAH/PSS, the amount of added rods was adjusted to 0.084 mg (1 mL solution of 0.084 mg/mL). All spheroids were located in the area marked with the red circle. The laser was aligned at the center of the accumulation. Initial laser power was set as  $10 \pm 1.5 \text{ mW}$ , which represented the lower limit for visibility of a laser spot. During all trials the shutter was kept close until this power was reached. Laser power was then gradually increased to a maximum value of  $31.5 \pm 1.5 \text{ mW}$ . The left heat

map always represents the situation without any trigger. In the top row, it represents the status for a closed shutter. The whole dish interior appears in uniform temperature of circa 21 °C, being slightly colder than the surrounding background. For the maximum power situation (heat map on right side), the highest laser strength was applied to the spheroids. On the contrary to the shuttered condition, a clear heat spot ( $T = 22.5$  °C) appeared at the illumination spot, which originated from the GNRs inside the capsules. Each rod reacted onto the illumination and induced some heat. The entirety of thermal energy across the spheroids appeared as signature in the infrared record. To confirm the heating interrelation with the GNRs, secondary examinations were carried out with sheer medium. With removal of spheroids all GNRs sources were removed concurrently. As a consequence, no particles and, therefore, no heat mediators were present. This control was treated in an exactly identical way to the spheroid sample. The results are shown in the second row of figure 27. The infrared images recorded at shuttered condition are nearly identical for sample (first row) and control (second row). However, no heat signatures appeared in the circle when the control was illuminated. The dish showed no reaction on the laser light. This validates the spheroids (and in detail the GNRs) as the origin of the heat in the first row, as their removal was the only change between both conditions. Moreover, it confirms the visibility of temperature variations during irradiation for a system working excellently in terms of release. Tests executed with an AMF are shown in the rows three and four. While the bottommost images are linked to the high field condition ( $H = 300$  Gauss), the third row depicts the lower field ( $H = 192$  Gauss) results. As irradiated area for the magnetic field condition exceeded the dimensions of the laser spot, spheroids did not need to be squeezed into a small part of the dish. That's why no identical red circle can be found in the figure. The AMF allowed for irradiation of spheroids across the complete dish simultaneously. Trials with magnetic spheroids squeezed together were still carried out but aren't shown here due to identical outcome. Similar to the laser experiment, the left infrared image always shows the time point without sample irradiation. At this condition, heat signatures must be missing. The other record (right map) was taken during the final seconds of irradiation under presence of the corresponding maximum field strength. The analyzed system consisted of MCF-7 cells interspersed with capsule CS 02 at a ratio of 2:1. The incorporated IONPs (#45) acted as heat sources. For sufficient energy conversion, the sum of heat would make the whole spheroids appear as heat spots in the infrared shot. However, magnetothermal heating was neither visible for the low nor for the high field condition. All four IR-images in the rows three and four look alike inside the dish area and not a single heat spot was observed. So, none of the iron-based spheroids faced a similar temperature increase as the GNR-spheroids during their stimulation.

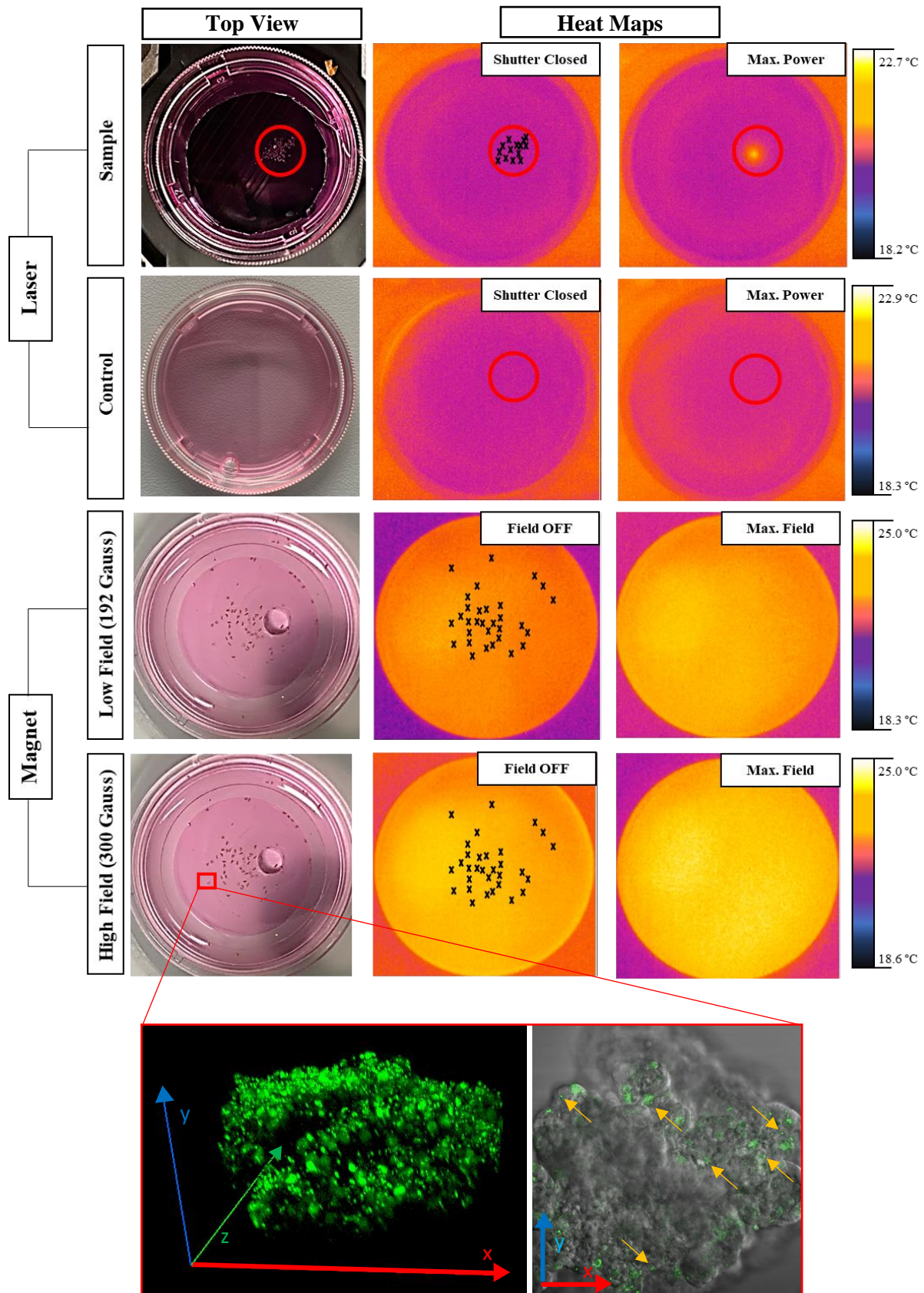


**Figure 27:** Temperature shots for spheroids under either laser or AMF-irradiation. Heating behavior was compared for gold-based and iron-based spheroids in their typical trigger conditions. While laser irradiation induces clear heat signatures, magnetic field influence does not.

This underlines the supposition of big differences in heating being present, when comparing lasers and magnetic fields in triggering purposes. In addition, it supports the possibility that endosomal/lysosomal escape has impact on insufficient magnetothermal *in vitro* opening. While laser-illumination on plasmonic nanoparticles results in hyperthermia strong enough to damage both capsule shell and surrounding organelle simultaneously, AMF treatment on magnetic nanoparticles may suffice to disrupt the polymer carrier but not the membranes around. Consequently, no cargo movement into the cytosol happens. Another explanation could be reduction or absence of capsules in the iron spheroids. But a view inside one of the magneto-responsive spheroids, which is provided in the final part of figure 27, refutes this option. The 3D-snap on the left side shows green color arising from the encapsulated dye. It is only present in capsules or, in case of leaching or release, the cytosol. As calcein represents a cell impermeable dye, transfer from cell to cell is not possible. The presence of color all over the structure attests the distribution of capsules across the complete spheroid. One cutting plane of the spheroid is additionally presented next to the complete spheroid. At close look, multiple individual capsules - some being marked by orange arrows - are noticeable. Consequently, the absent visibility of temperature increase can only be related to reduced heating capability of the capsules and the inserted MNPs, respectively. Based on the fact that even the strongest heaters among the MNPs showed significantly worse energy conversion than typical PNPs, achievement of higher release ratios under biologically applicable conditions became increasingly challenging.

Still questionable was, however, if non-applicable conditions would improve the outcome. Especially the number of particles factually required for a first appearance of significant heating was uncertain. In terms of capsule functionalization, the maximum particle number for attachment is restricted by the carrier surface area. For free particles, however, fewer limits are set. Like that, uptake into cells is majorly restricted by toxicity. Meanwhile, dissolution in water offers limits at higher levels as nothing but saturation has to be taken in concern. To work out the effect of free IONPs, differently concentrated suspensions of batch #77 were measured inside an ibidi 8-well plate under two circumstances: 1) dissolved in water and 2) after uptake by cells. While the water samples were just restricted by the highest available concentration, immensely high concentrations could not be applied to cells due to certain cell death. Therefore, the highest concentration added to cells was 666  $\mu\text{g}/\text{mL}$  (= 14.47 nM), while pure NPs were even tested at 5 mg/mL (=108,6 nM) seeding. The exact concentrations for the cell samples can be observed in table 4. It also presents the amount of iron present in cells after 24 h incubation. For comparison, the mean amount of iron per capsule is also shown.

**Table 4: Concentration list for particle exposure (#77) to MCF-7 cells.**

| Sample<br>Size: $26.48 \pm 1.92$ nm, $M_w = 46034.4$ kDa |          | Cell Number<br>after 24h incubation | Amount per Cell or<br>Capsule (pg) |
|--|----------|-------------------------------------|------------------------------------|
| 0 $\mu\text{g/mL}$                                       | 0 nM     | 31875                               | 1                                  |
| 100 $\mu\text{g/mL}$                                     | 2.17 nM  | 35625                               | 283.98                             |
| 250 $\mu\text{g/mL}$                                     | 5.43 nM  | 33750                               | 544.25                             |
| 500 $\mu\text{g/mL}$                                     | 10.86 nM | 20625                               | 939.07                             |
| 666 $\mu\text{g/mL}$                                     | 14.47 nM | 18750                               | 3248.3                             |
| Capsule  |          | /                                   | 38.36                              |

All samples were filled into individual wells inside an 8-well ibidi plate. The whole plate was irradiated at the high field condition:  $H = 24$  kA/m (= 300 Gauss) with a frequency of  $f = 300$  kHz. The time point of comparison was set to the final seconds of treatment to minimize possible teething problems (*i.e.* around 15 min after start). In terms of the water-dissolved particles, two wells were left as control (= 0 mg/mL). All other wells were filled with IONP-solution at different concentrations: 1) 5 mg/mL, 2) 3 mg/mL, 3) 1 mg/mL, 4) 0.5 mg/mL, 5) 0.3 mg/mL and 6) 0.1 mg/mL. The mean temperature at initial time was measured as around 23.0 °C across the whole plate. During the irradiation process the whole plate heated up. This majorly resulted from the two specimens of highest concentration which were located in the upper left corner of the ibidi well. They showed a brilliant temperature increase of around 6 °C over time (*cf.* figure 28, maximum field condition). Weak but present increase was, however, also recorded for the control samples. This most-likely results from artefacts due to close contact to the two strong heat sources nearby. During previous trials, particle-free samples never showed any significant temperature change due to heating over time. Similar effect can also be observed for the sample with 0.1 mg/mL. It seems like, with 1.2 °C increase, it did induce more heat than both 0.3 mg/mL and 0.5 mg/mL. But the real heating is probably concealed by stray light. A more probable behavior is present for the two aforementioned samples 4) and 5), which are most distant to the brilliant wells. Their temperature increased up to a maximum of  $\Delta T = 0.7$  °C. Finally, mediocre heating was recorded for the sample containing 1 mg/mL. While effect of artefacts cannot be excluded, a  $\Delta T$  of 2.5 °C exceeds all less-concentrated wells, which implies an additional impact of actual heating. Slight increases for lower concentrations, however, cannot be blackballed. They might have been suppressed by the working principle of the whole system: Not only does the infrared camera permanently

rearrange its temperature scale which hampers the record of narrow differences under concurrent presence of huge ones. But in addition, the field producing coil is permanently water-cooled which also affects the sample itself due to direct contact. The overall visible T-change might, therefore, be lower than the real one inside the sample chamber because of counteraction between NP-heating and system-cooling. Despite all the issues, it can be concluded that intense heating becomes visible for free particles dissolved in water once the concentration is high enough. This also fits reports about magnetic hyperthermia where pure IONPs were used to induce destructive amounts of field under field irradiation.<sup>138,139</sup>

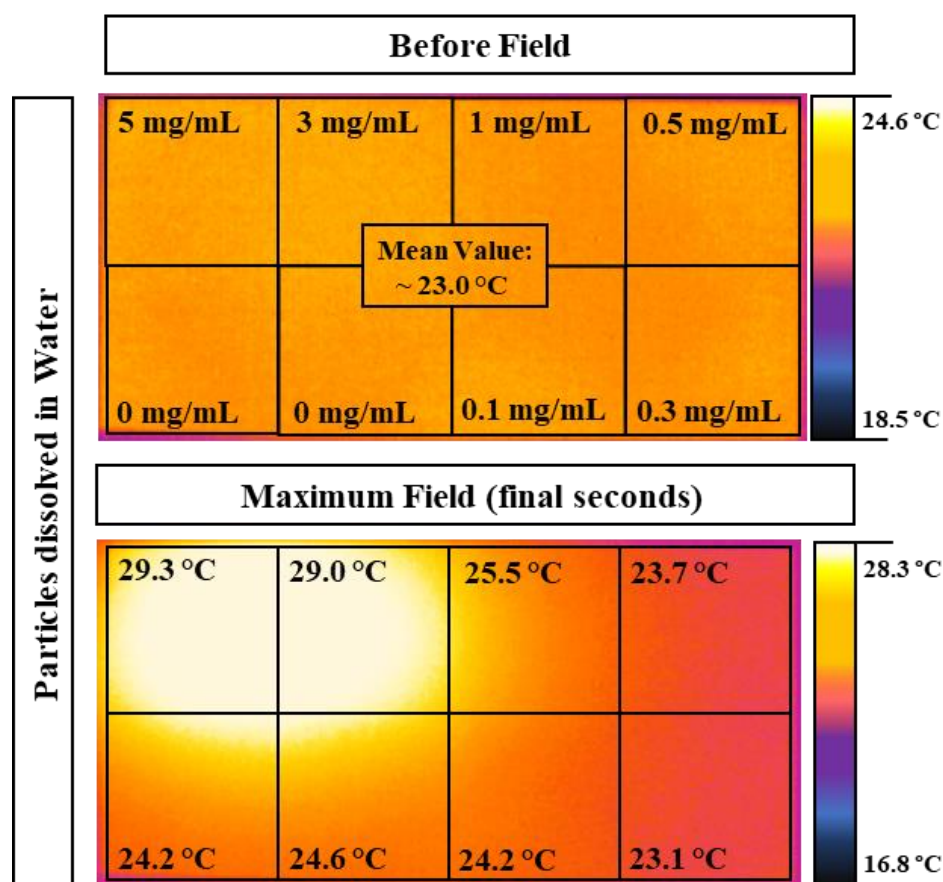


**Figure 28:** Heating behavior for differently concentrated free particles in water under AMF contact. Six different solutions of IONP #77 were examined in terms of heating when irradiated with the high field condition. Especially for the two most-concentrated samples intense heating was visible (top left corner).

In a similar manner the cell samples were analyzed subsequently. For that, 20,000 MCF-7 cells were incubated per well inside an 8-well ibidi plate and the particles were added for uptake after one day of attachment time. Two identical plates were prepared from which one was used

for uptake and particle-per-cell determination. The other one was for heating analysis. On the third day, the current cell number was recorded for one plate whereas the other system was transferred to the heating set-up. The count in cell number was necessary because of changes from the initial seeding number due to impact of particle toxicity and cell proliferation. In fact, the spread comprised more than 10.000 cells between the different conditions. The final cell count delivered the following numbers: 666  $\mu\text{g/mL} \triangleq 18,750$  cells; 500  $\mu\text{g/mL} \triangleq 20,625$  cells; 250  $\mu\text{g/mL} \triangleq 33,750$  cells; 100  $\mu\text{g/mL} \triangleq 35,625$  cells and 0  $\mu\text{g/mL} \triangleq 31,875$  cells. This was related to damage induced by presence of several particles per cell. Under use of ICP-MS the seeding concentration was recalculated to particle amount per cell after uptake. The results delivered for instance around 284 pg/cell when incubated with 100  $\mu\text{g/mL}$  and 939 pg/cell for 500  $\mu\text{g/mL}$ . The complete list is shown in table 4 above. Results related to the most-concentrated cell sample are, however, to be considered with care as the amount per cell clearly transcended the trend for the other cell samples. It showed an absurd high amount of 3.25 ng/cell which did most probably arise from cleaning issues going along with record of free NPs in the supernatant. For comparison: the amount per individual capsule is equivalent to 38.4 pg/capsule. For typical trials, two capsules were added per cell. This adds up to around 77 pg per cell. The cells in the reliable ibidi wells, therefore, contained particle amounts of up to 12-fold to typical release trials. The corresponding heating outcome is presented in figure 29. Based on the previously observed heat transfer between wells, control and strongest concentration were separated with maximum distance from top left to bottom right well. Before field application the whole plate was of uniform temperature with mean value of around  $T = 23.9$  °C. An identical snapshot was taken during the final seconds of irradiation with the high field ( $H = 300$  Gauss,  $f = 300$  kHz). On the contrary to the beginning, all wells showed different temperatures at this time point. However, all temperature changes were negative, meaning that cell medium cooled down during the experiment. As mentioned before, the whole system is water cooled to avoid damage to the coil set. Water temperature thereby drops down to a minimum of  $T = 4$  °C. This process significantly affects the sample as well. For the control,  $\Delta T$  equals  $-0.8$  °C. So almost one degree was lost during AMF treatment if no heat source is available. Similar behavior was present for the lowest seeding concentration ( $= 100$   $\mu\text{g/mL}$  or 2.17 nM) were  $\Delta T = -0.9$  °C. Consequently, 284 pg iron per cell are not sufficient to induce any detectable change in heating compared to the control. As this amount nearly equals the amount attached to a sum of four capsules, it can be considered that doubling the capsule number per cell would also not induce visible heat hazes. Even for seeding with particle concentration of 5.43 nM ( $=250$   $\mu\text{g/mL}$ ), which caused 544 pg iron per cell, the temperature dropped more than

half of a degree. This amount already corresponds to 14 capsules per cell and still didn't enable any detectable heating. Eventually, seeding with 500  $\mu\text{g/mL}$ , or 10.86 nM respectively, showed some response: Even though no increase in temperature was detected, the temperature remained nearly constant over time. As the control, however, showed a clear drop, some heating must have been present for this sample to keep the temperature stable. At really careful look onto the magnified images, shown at the bottom of figure 29, slight color differences can be spotted between the control and this well. It can be considered that 939 pg of iron per cell have finally surpassed the visibility limit of heat signatures.

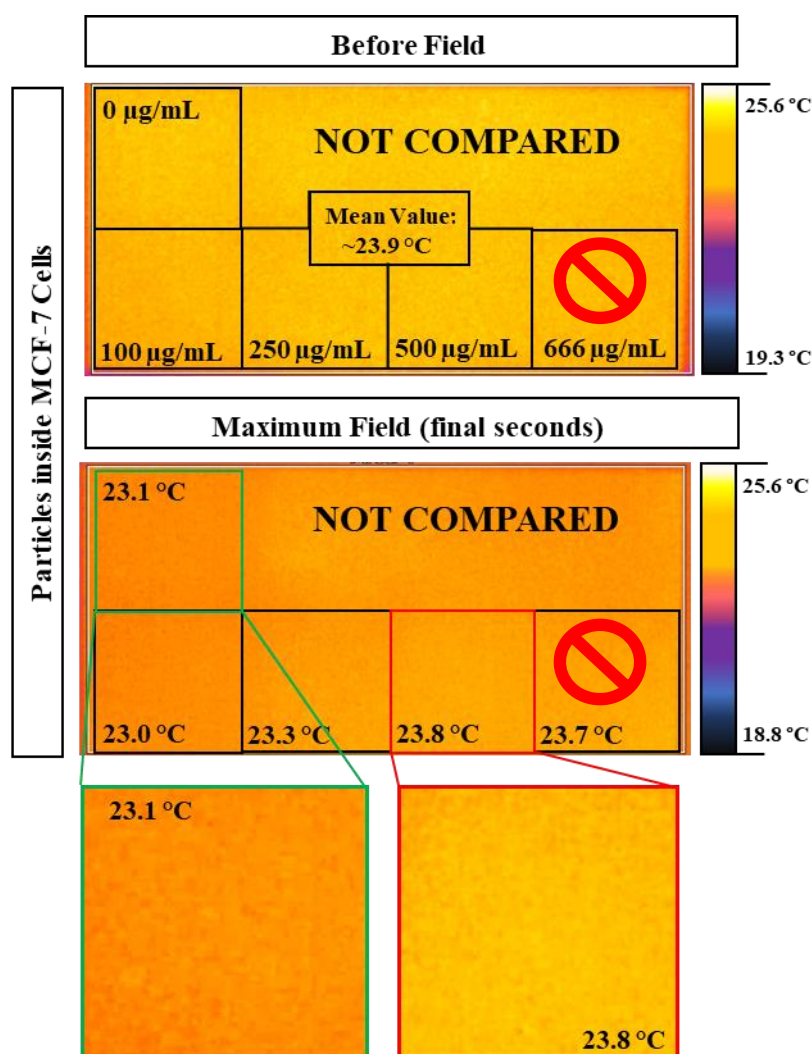


**Figure 29:**

**Heating behavior for different amounts of particles inside MCF-7 cells under AMF contact.** MCF-7 cells were exposed to differently concentrated solutions of IONP #77. After removal of free NPs, the individual wells were examined in terms of heating under magnetic irradiation. For seeding with 500  $\mu\text{g/mL}$  some heating was detected. The highest concentration showed irregularities and was disqualified.

Achieving this amount by capsule uptake would, however, require 24.5 capsules per cell. This is equivalent to a 12-fold increase in comparison to all prior conditions used for release evaluation. Nevertheless, heating of encapsulated MNPs definitely took place. To directly detect it, an ensemble of nearly 20k cells with around 939 pg per cell was crucial. Otherwise, counterplay with system cooling as well as additional factors did conceal the actual process. This represents a slightly reduced behavior in comparison to the free particles in water, for which an identical seeding concentration showed a little temperature increase over time. However, probably not all particles did get taken up during cell exposure and some were washed away afterwards. Consequently, the number of particles inside the entirety of cells was lower than in the water solution and the heating accordingly, too. Moreover, aggregation tendency of particles when entering the cells in comparison to freely moving particles might have also played a role. Thus, cell uptake was reported to lower SAR by Etheridge *et al.*<sup>140</sup>

### 4.5 Final Insights

Presence of significant discrepancies in energy conversion between magnetic and plasmonic heat-mediators was evidenced by the previous chapter. This tendency was especially present for particles applied to capsules to act as the trigger sources for opening. Not even the strongest heaters among the iron oxide particles, providing SAR values of more than 1000 W/g, allowed for visible heating when inserted into the capsule shell and spread across tumor spheroids. On the contrary, gold-based spheroids with identical capsule-to-cell ratio (2:1) showed a clear heat spot when treated plasmonically. Each of the corresponding capsules contained 29.81 pg gold. And this despite a higher amount of heat source per magnetoresponsive capsule, which was calculated as 38.36 pg of iron each. Indeed, very high numbers of free magnetic particles also showed noticeable energy conversion, but the required conditions were not usable for bioapplication. Moreover, the appropriate amount of 24.5 capsules, which would be required per cell to equal the amount of heat source, corresponded to a 12-fold increase to every former condition. Not considering other factors, this directly appears critical just by looking at capsule and cell volume. Such a high number of capsules would occupy a considerable part of the complete cytosol of a cell. Even though 20 capsules per cell didn't seem to impact viability (*cf.* chapter 4.2), such a high ratio is not practicable. Moreover, on basis of these findings, it remained very realistic that endosomal/lysosomal entrapment represented the crucial barrier preventing better release ratios. The huge heating discrepancies between plasmonic and magnetic systems were also reflected during the opening process. Even though heating took place inside the shell of the iron-based capsules and diffusion might have been restored with

field contact, the surrounding membranes did most-likely not undergo the same disruption. As a consequence, cargo wandering into the cytosol remained absent during the release investigations. To support the assumption of endosomal/lysosomal entrapment, MCF-7 cells were once again exposed to capsules from type CS02 at a ratio of two-per-cell. Exposure took place after one day of attachment time and lasted overnight. After washing to remove free capsules, the system was subjected to two fluorescence markers. Each type was dedicated to a specific compartment: Hoechst 3352 was added to stain the nucleus, whereas LysoTracker Red DND-99 was used to colorize acidic organelles like the late endosomes and lysosomes. In addition, the fluorescence caused by encapsulated calcein was collected as a third fluorescence signal. Blue nucleus staining was applied to facilitate cell focusing and to ensure capsule localization inside cells. Besides, it supported the statement of capsules not being able to enter the nucleus. Colocalization of both other signals was required to guarantee capsule positioning inside the organelles. As capsules can only enter the cytosol when endocytosed and encapsulated by endosomes, every intracellular green calcein signal must overlay with red signal from the acidic compartment. An example for such a condition is shown in figure 30.

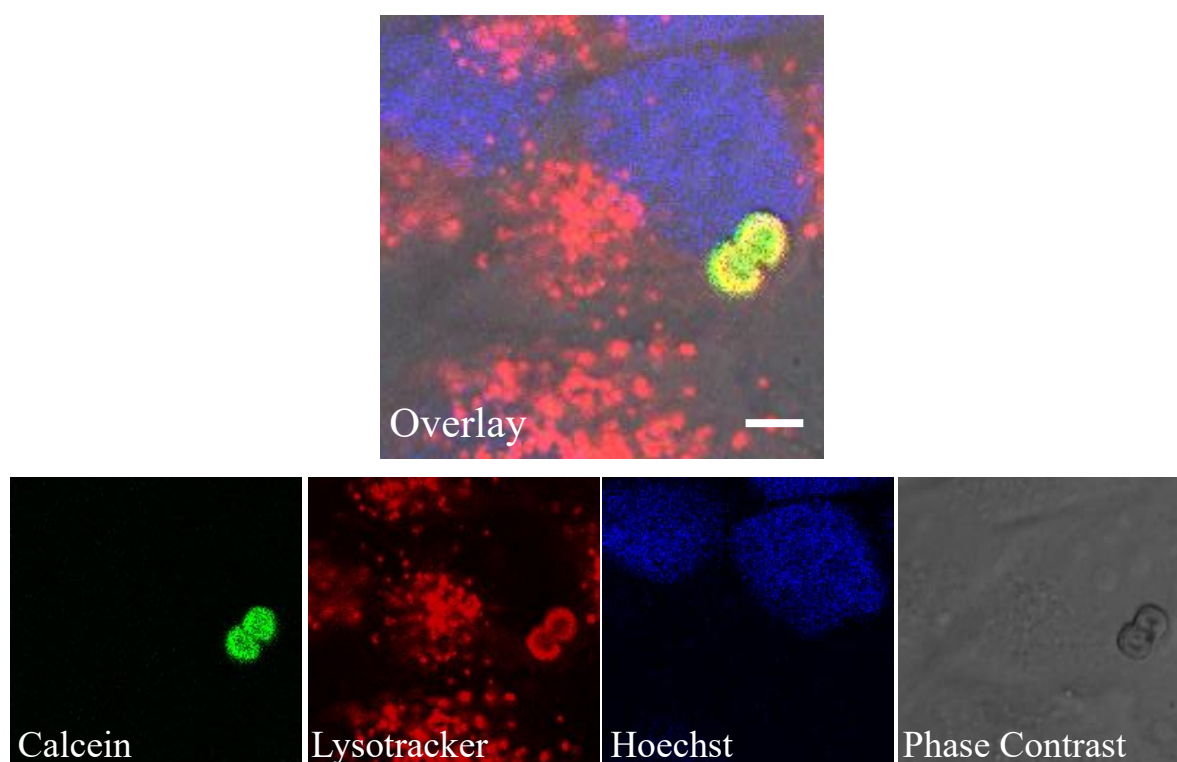


**Figure 30:** **Fluorescence marking and colocalization of different dyes to analyze capsule location.** MCF-7 cells were exposed to calcein-loaded capsules and treated with nucleus-staining Hoechst 3352 plus organelle-staining LysoTracker Red DND-99 to analyze the exact capsule location. Data from individual channels is shown below the overlay image. **Scale: 5  $\mu$ m**

Two capsules are located really close by the blue nucleus. Comparison of signal from the Hoechst channel (blue) with calcein or transmission data confirmed the location outside it. In addition, green and red fluorescence highly overlay at the capsule locations and appear as yellow in sum. LysoTracker is only present in acidic compartments and emits light at a wavelength around  $\lambda_{em} = 590$  nm when excited at  $\lambda_{ex} = 577$  nm. On the contrary, calcein shows emission at  $\lambda_{em} = 514$  nm. Data from both channels can, therefore, not be related to artefacts like crosstalk. This clearly secures presence of the carriers at endosomal or lysosomal sites and insures the existence of a secondary membrane around the capsules. Additional red signal belongs to other acidic compartments across the cytosol. With that, it only needed to be confirmed that the overlay does not undergo changes during field application. To check for that, the cells were treated with the low field condition ( $f = 300$  kHz,  $H = 192$  Gauss) for one hour and imaged again. Low field was chosen in accordance with the conditions used for all previous release trials. The cell shown in figure 30 is presented in figure 31 for both time points. The left side represents the situation before field contact whereas the condition after field is shown on the right. The signal related to the Hoechst is congruent for both moments so the nuclei didn't move or change form. Slight intensity reduction is up to the time span between both shots. The red fluorescence underwent significant changes across the whole cell. This belongs to movement of the organelles across the cytosol, which is an expected progress over time. The red signal connected to the two analyzed compartments, however, doesn't show a major change. It just slightly varies in intensity while form and location remained the same. Accordingly, heating related to energy conversion by the encapsulated capsules and particles did not damage the endo-/lysosomal membrane. For the calcein signal, however, a slight change is visible. Especially the lower capsule lost intensity and the fluorescence isn't as confined as before. Quite the contrary, the signal seems softened and more pixelated. This could be an allusion for release of cargo from the carrier into the acidic compartment and thus the confirmation of endo-/lysosomal entrapment. With diffusion into the surrounding compartment, the cargo would occupy more space which could be the explanation for a more softened signal. With similarity of form and size between lysosomes and carriers it is, certainly, hard to examine whether delivery took place or not. Such a behavior was not resolvable by this imaging process. Nevertheless, localization inside endo- and lysosomes has been confirmed and their stability during field contact despite capsule presence been proven. With that, the assumption of endosomal entrapment remains the most-probable explanation for absence of high release ratios during magnetothermal treatment.

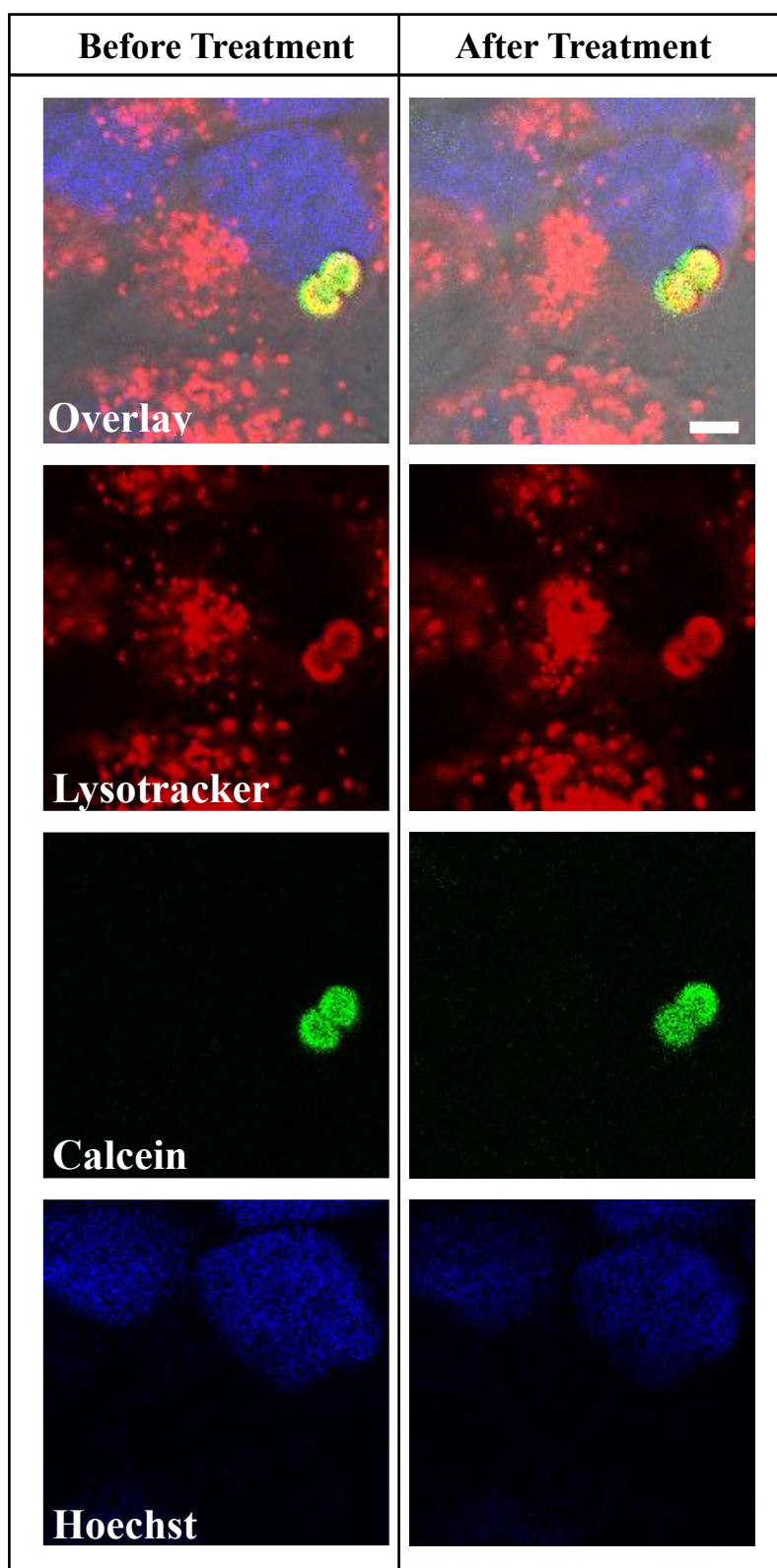


**Figure 31:**

**Comparison of fluorescence-marked MCF-7 cells before and after AMF treatment.** MCF-7 cells were exposed to capsules and treated with two fluorescence markers to identify the exact capsule location. Imaging took place before and after field treatment at the low field condition. Endosomal structures remained intact, which benefits assumptions on 1 entrapment. **Scale: 5  $\mu$ m**

In detail, several issues affecting extensive cargo release were identified during the heating evaluation. Limited number of particles per capsule and endo-/lysosomal entrapment are two examples. Additional problems arised from the biological limit of the external alternating field. It restricted the field properties to a regime of downsized heating to avoid damage to tissue by induced eddy currents.<sup>129</sup> As a result, heating of the limited number of particles was further hampered. In addition, the structure of the capsule system itself represents a noteworthy challenge. Functionalization with particles is highly required to achieve interaction with the AMF. For that matter, the particles need to be positioned in a stable environment inside the shell to directly manipulate it during heating. This is accomplished by engulfment in between two polymer layers. This process, however, strongly immobilizes the particles and diminishes their relaxation. IONPs can be subject to superferromagnetism for small distances between individual particles.<sup>131,141</sup> This process describes interaction between multiple particles due to the magnetic properties and leads to formation of superordinate structures. Such structures exhibit for instance higher  $M_s$  values, which also impacts the heating capability.<sup>142</sup> Breaking up these structures significantly changes the heating behavior. Such a process takes place if IONPs are linked to the capsule shell. Once internalized between two polymer layers the formation of structures becomes suppressed and the heating ability drops. In this way even the best-converting particles suffer significant heating reduction. Without techniques increasing the production of thermal energy or minimizing damage at higher fields the identified problems with cargo delivery in cells will most-likely remain. Under the current circumstances, interplay between all limiting factors impedes competitiveness of the given magnetothermal system with comparable trigger mechanisms for *in vitro* applications.

## 5 Summary and Conclusion

*"A conclusion is the place where  
you got tired of thinking."*

*Martin H. Fischer*

This project included the whole process of development, improvement, evaluation and assessment of excellent magneto-responsive carrier systems to be used as transporters for cargo delivery inside living cancer cells. While already developed for multiple other approaches, reports about usability of polymeric multilayer capsules for controlled release under exposure of magnetic fields were marginal beforehand, especially *in vitro*. Initially, focus was put on improvement of the magnetic properties of the accessible nanoparticles to gain outstanding heat mediators. Choice of the most promising material, selection of an ideal synthesis route and subsequent tuning of the water-transfer coating represented the most crucial tasks. One specific, iron-oxide based particle type thereby stood out significantly, showing extremely high SAR values in the regime above 1000 W/g. These values, however, tended to change dramatically with applied coating. PMA-ND was chosen for further use despite its weakening effect on heating due to outstanding solubility in water. Other ligands delivered higher heating values but went along with notable solubility issues. Capsules were formed from non-biodegradable polymers, functionalized by addition of these magnetic iron-oxide particles into their shell and loaded with green-fluorescent dye. The final carriers showed colloidal stability and brilliant loading efficiency while maintaining the magnetic properties of the particles. Classical capsule structure was set as (PAH/PSS)<sub>2</sub>/[PAH/NPs]<sub>x</sub>/PAH/PSS, with different amount of particle layers to change the heating capability and heat-shrinkage to seal the shell. Resulting release ratios moved around low percentage. Therefore, multiple trials to improve the opening were carried out: Removal of heat shrinkage to make capsules less robust, replacement of the encapsulated dye, and addition of disintegrating substances to boost shell disruption represented the most important ones. Not all approaches provided stable carriers and some even caused damage to the cells. For intact representatives, however, many still remained undamaged and each release ratio ranged at low percentages. Hence, it was aimed at working out the issues and obstacles inhibiting higher ratios. Under observation of the local temperature level through infrared imaging, evaluation of actual particle heating behavior at the shell site inside cells was targeted. In a first evaluation, clear differences between free and encapsulated particles were noticed. Both systems suffered at low field conditions ( $H = 192$  Gauss), but in addition

encapsulation caused a significant reduction in temperature increase during irradiation with the high field ( $H = 300$  Gauss). This effect was linked to break up of structure-forming superferromagnetism once the particles are inserted into the shells. Due to the fact that heating was not completely absent for capsules it was subsequently examined if free capsules showed cargo delivery, which would transfer the difficulties towards cell uptake. Indeed, clear delivery was recorded for both field conditions. Therefore, endo-/lysosomal entrapment was assumed as the new hurdle hindering the diffusion into cell cytosol. For a more detailed insight, the magnetothermal system was compared to laser-based opening, for which heating suffices to break both carrier and surrounding organelles. Under typical conditions, photothermal treatment of capsule-spreaded spheroids showed a clear heat signature. Similar outcome was missing for magnetothermal treatment of similar spheroids. So, clear discrepancies in actual amount of heat produced during irradiation were recorded. MNPs were not able to show similarly strong energy conversion as plasmonic particles when irradiated at a power close to the limit for biomedical application. Even at conditions above the limit, no drastic improvements were observed. However, for an ensemble of 20,000 cells, each containing 939 pg iron, some heating was finally recorded. This equals the amount of iron present in a collection of 24.5 capsules. The fact that such a high number was required to see any effect favored the entrapment theory inside endo-/lysosomes. To confirm the capsule localization in such structures after uptake, cells were marked with different dyes and the exact location was examined. Carrier engulfment by acidic compartments was confirmed and remaining entrapment after application of a biologically applicable field supported.

In conclusion, the *in vitro* usability of magnetoresponsive polyelectrolyte capsules has been examined comprehensively. Multiple approaches were tested but none offered outstanding release opportunities. Explicit heating issues were worked out when compared to excellently working photothermal opening. It can, therefore, be stated that the present system doesn't represent a credible contender to similar other triggers to date.

## II. Side Project: Deep-Tissue Viability Probing by Photothermal Cargo Delivery

### 6 Objective/Motivation

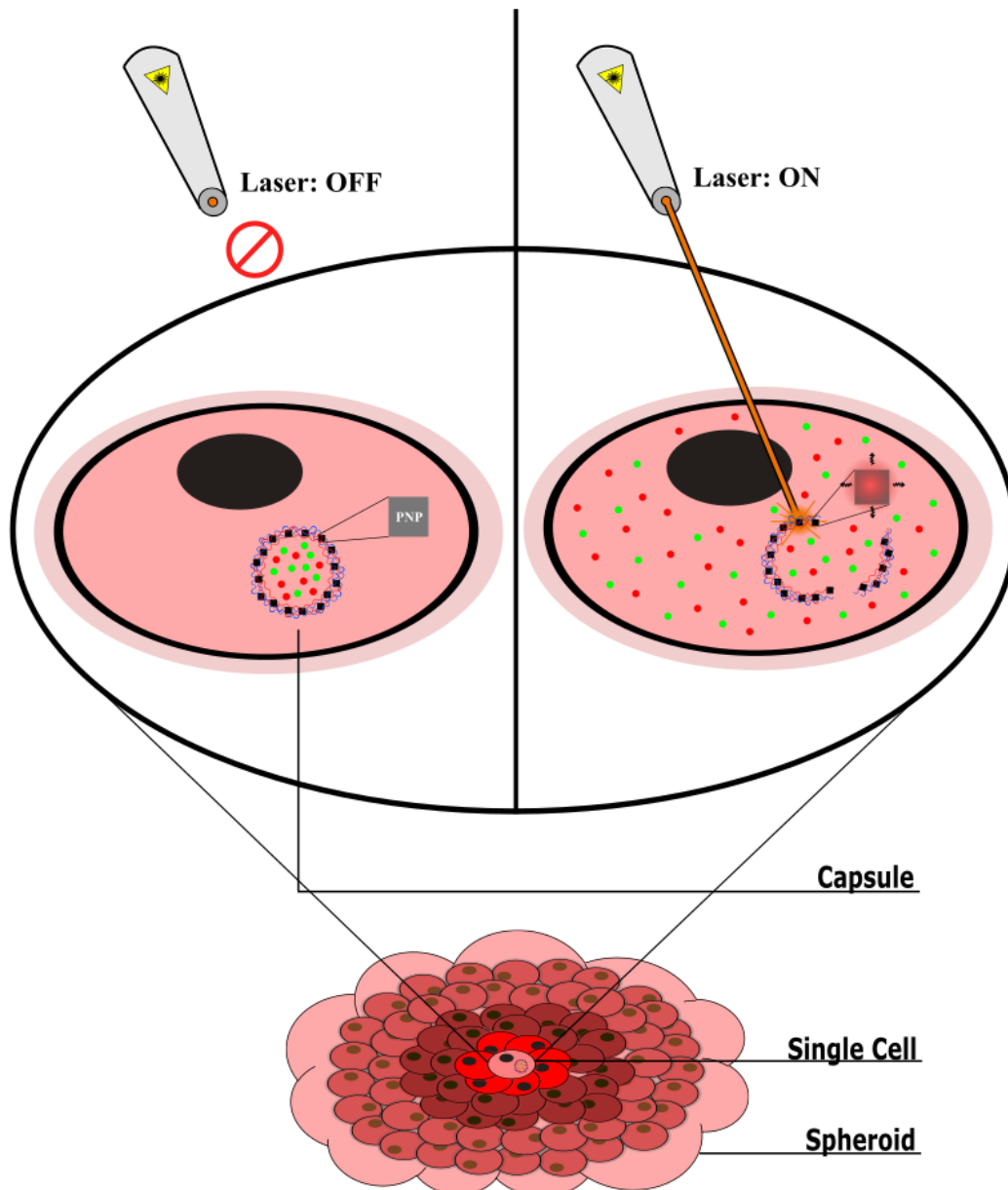


**Figure 32:**

**Sketched idea of deep-level photothermal capsule opening in spheroids.** By illumination of single capsules, which are located in the cytosol of cells, the release of cargo into the cytoplasm is triggered. Cell location in the centre of spheroids transfers the principle to deep tissue level. Use of dyes capable to exhibit live/dead-staining allows for contemporaneous information gain about cell health. Consequently, an on-demand viability test deep inside tissue is achieved.

Laser-induced disruption of polymer capsules to induce cargo release represents a reliable exertion in 2D cell systems.<sup>143</sup> Transfer to thicker and three-dimensional environments, however, goes along with challenges regarding absorption and laser penetration depth.<sup>12</sup> Therefore, the objective of the featured project was the opening of individual capsules located behind multiple cell layers inside the center of a spheroid. By encapsulation of two separate dyes with different color and cell permeability, the cells should be tested regarding viability by a live/dead-staining approach concurrently. The idea is sketched in figure 31. All trials are supposed to take place in the center part of the spheroid as indicated by the presence of a capsule inside the cell in the very middle. For a situation without illumination, the capsule remains completely intact and both dyes stay confined to its cavity. Once the laser is turned on, the heat arising from the inserted plasmonic nanoparticles induces shell damage and allows for cargo migration into the cytosol of the specific cell. The resulting color then gives information about the cell health as their presence changes betwixt healthy and unhealthy conditions due to membrane damage. Consequently, the intended system represents an on-demand analysis tool for cell health at deep tissue level.

The first step of the present work was dedicated to fine-tuning of the carriers. Previously observed issues with gold-based PNPs forced a change to other heat-mediators.<sup>144</sup> Subsequently, the presence of carriers at the spheroid center part had to be ensured. Different attempts were executed to confirm their location. Finally, specific cells were chosen for opening trials of capsules. The laser was focused on capsules inside their cytosol and the cargo spread was recorded.

## 7 Materials, Synthesis and Methods

Materials, substances and synthesis routes already mentioned in the first project (*cf.* chapter 3) are not listed in detail again. Especially the IONPs and capsules were prepared identically or existing batches were continuously used.

### 7.1 Synthesis and Tuning of Plasmonic Nanoparticles

#### 7.1.1 Gold Nanorods

Gold nanorods (GNRs) used here were taken from already prepared batches which had been synthesized previously by S. Hecht in accordance to an established protocol.<sup>145</sup>

#### 7.1.2 Iron Oxide Nanoparticles

Iron oxide nanoparticles were synthesized by the same route<sup>23</sup> as presented in the main project (*cf.* chapter 3.3.1), but the added amount of Fe(acac)<sub>3</sub> was changed to 0.848 g (2.3 mmol), which caused a mean diameter of  $19.1 \pm 1.08$  nm (batch #49). Afterwards, the NPs went through ligand exchange to achieve water solubility. The water transfer ligand was DMSA (*cf.* chapter 3.4.2).

### 7.2 Capsule Synthesis and Loading

Polyelectrolyte capsules were assembled by alternate deposition of PSS and PAH around a CaCO<sub>3</sub> core. Between addition of the fourth and the fifth polymer layer nanoparticles (either gold or iron) could be attached for functionalization. The resulting composition was (PSS/PAH)<sub>2</sub>/NPs/PAH/PSS. After core dissolution through EDTA and several washing steps to remove residual acid, the hollow carriers were postloaded with dye. Typically, 1 mL dye solution (calcein: 3 mg/mL, PI: 5 mg/mL) was added to the capsules for 1 h without disturbing and the system was subsequently heat-shrunked at 70-75 °C for 90 minutes. Finally, the supernatant was cleaned from dye traces during multiple washing runs. Loading of photosensitizer (*i.e.* chlorine e6) was achieved by addition of sensitizer dissolved in DMSO (10 mg/mL) to DMSO-prewashed capsules (no NPs) for 1 h and subsequent washing with water for several times.

## 7.3 Preparation and Tuning of Cell Spheroids

### 7.3.1 2-layered Spheroids

To induce the formation of spheroids containing two independent layers, a slightly modified approach was used: After inversion of the petri dish lid and incubation for one day the spheroids were not collected but another 20  $\mu\text{L}$  of solution were added to the drops. These droplets were taken from a freshly prepared solution which contained cells and methyl cellulose. However, these cells were marked with a red dye (CellTracker Deep Red) beforehand. For that, the cells were seeded inside a 6-well plate the day before and incubated overnight. Then, the cells were washed with PBS once. 1.5 mL serum-free cell medium were added together with 1-1.5  $\mu\text{L}$  dye before incubation for 30 minutes. Another washing step was applied and the cells were detached using trypsin. After centrifugation at 300 rcf for 5 minutes the cells were resuspended in FBS-containing cell culture medium and 350,000 cells were taken out for further use.

## 7.4 Photothermal Capsule Opening

Cells and capsules were initially imaged by a scanning laser under use of the Argon laser line at  $\lambda_{\text{scan}} = 488 \text{ nm}$ . Laser-based bleaching on capsules was subsequently carried out by illumination of single capsules with a two-photon laser at  $\lambda_{\text{bleach}} \approx 800 \text{ nm}$ . Laser power was typically set to 10 % for deep-level tests which equals a power of  $P_{\text{Laser}} = 283 \text{ mW}$ . The specific time of bleaching changed with the illuminated area but was mainly adjusted around a total of  $t = 1 \text{ s}$ .

## 7.5 Testing Viability using PI and Calcein

To evaluate cell viability, propidium iodide and calcein were used here. The cell-impermeable calcein represents the positive probe showing fluorescence only if cells are healthy. It offers long retention time and stays entrapped inside the cells as long as they are not damaged. The red fluorescence related to PI is not connected to cell health which leads to an autonomous appearance. Once it enters a cell it binds to nucleic acids which boosts the fluorescence and remains independent from the membrane condition. Polyelectrolyte capsules were used to encapsulate both dyes at the same time. In this way the dyes could enter the cells but remained entrapped inside the carriers. To induce a subsequent release, photothermal heating was applied to single capsules which restored diffusion from the carrier into the surrounding cytosol. For healthy cells the green and red fluorescence superimposed to a yellow output signal across the whole cell. For dead cells, on the contrary, only red was measurable. In this way the condition could be evaluated for every cell individually.

## 8 Results

Based on polymer capsules and the corresponding opening under use of a near-infrared laser it was planned to release fluorescent cargo in center parts of tumor spheroids to enable deep-level viability testing. This would represent an on-demand check for cell health, which could be extended by interconnection with a damage source to directly visualize cell harm at occurrence. Initially, capsules fine-tuning towards stability and efficiency was targeted. Then, spheroid adjustment for good visibility was destined. Lastly, recording of actual opening was purposed.

### 8.1 Capsule Fine-Tuning

The initial object of focus were the loaded capsules. Typically, gold nanoparticles (AuNPs or GNPs) are used as the corresponding opening trigger inside the shell due to their photothermal heating under laser irradiation. However, it was observed that usability of GNPs and gold nanorods (GNRs) is limited if imaged with the 2-photon laser ( $\lambda \approx 770$  nm,  $P = 28.64$  mW) due to an immense increase of laser power in comparison to the one photon process ( $\lambda \approx 488$  nm). Many capsules ended up cracked just by observation which boosted the unintended premature release significantly.<sup>144</sup> A big opportunity, however, came from IONPs similar to the ones used in the first project. Their ability to produce heat not only under AMF contact but also under laser irradiation made them promising candidates. And the drop in heat production during the latter process in comparison to AuNPs helped reducing the leaching tendency. Even under sample scanning with the 770 nm-laser at an intensity of  $P = 40.096$  mW no opening was recorded.<sup>144</sup> For further investigation only iron-oxide based capsules were used. Their exact shell structure was fixed to  $(\text{PSS/PAH})_2/\text{Fe}_3\text{O}_4@\text{DMSA/PAH/PSS}$ . As indicated, one layer of DMSA-coated IONPs was used as the trigger system. For that, 1.5 mL particle solution ( $c_{\text{iron}} = 0.25$  mg/mL,  $c_{\text{MNP}} = 14.5$  nM) were added during shell preparation to all capsules. Under use of ICP-MS the exact amount of iron per capsule was calculated to  $1.54 \cdot 10^{-10}$  mg.

### 8.2 Capsule-Pervaded Spheroids

In the beginning, it was necessary to confirm the possibility to prepare spheroids completely pervaded with capsules. For that, multiple spheroids were prepared by a customized hanging-drop synthesis route: in addition to cells and methyl cellulose capsules were added to the drops at a capsule-to-cell ratio of 2:1. For a typical experiment these capsules were loaded with both red (Propidium iodide) and green (calcein) dye beforehand. During observation of the resulting spheroids by fluorescence microscopy, capsule spread across the whole cell system was then

clearly visible due to their fluorescence. As several capsules showed a premature release into the surrounding cells, a record of the complete spheroid structure was facilitated. One 3D-image of a whole spheroid is shown below. Especially the green color is visible because of stronger intensity in comparison to red. The whole system has an extent of around 300 $\mu$ m at its longest side and consists of several thousands of cells.

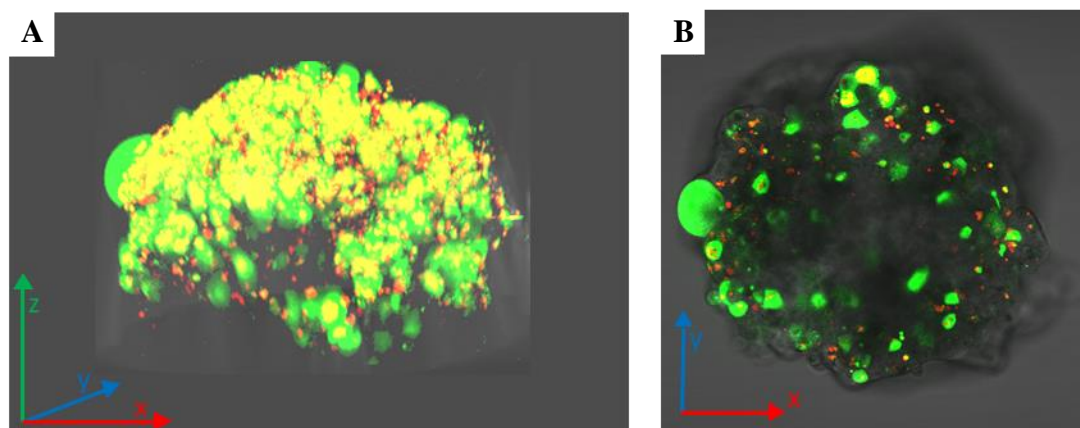


**Figure 33:** **Capsule-Pervaded Spheroid: Complete 3D-structure vs. one focus plane.** During spheroid growth capsules in the surrounding medium were incorporated into the tumor and completely pervaded it. Both a 3D look (A, left) and one slice in the z-direction (B, right) illustrate that.

Due to unequal growth of cells across the system, surface and size are not similar in every direction. Part B of image 33 does illustrate one specific focal plane in the center part of the structure. The orientation is exactly matching the 3D model but the direction of observation changed from front to top. Several capsules are present, which confirms capsule presence at deeper tissue parts and opens up the basis for examination of capsule opening at center depth. Improvements, however, are further required for the capsule stability and loading. Some capsules lacked one dye color and many were instable.

### 8.3 2-Layer Spheroids

During the previous tests the presence of capsules at all depths was confirmed. This represented an ideal result regarding the ability to completely pervade the spheroids but at the same time hindered the opening tests: as capsules were everywhere and only a single focal plane was observed at a time it was extremely hard to validate that the irradiated capsules were located at center parts. Therefore, it was thought of avoiding the availability of capsules in outer parts and confine them to the center. For that, spheroids made of two different layers were tried to prepare: For the inner part cells containing capsules were used. These capsules were loaded

with green dye only (*i.e.* CS 02, *cf.* table 2). The outer part was made of cells marked red beforehand. No capsules or other dyes were included. The idea was to first prepare the inner part and add the second layer afterwards to induce a growth on top. In this way the green signal should be confined to the center while red remains in outer and surface parts. The following figure 34 illustrates the outcome. The overall structure was comparable to the previously shown spheroids in shape and size. However, the red color was more powerful and intense for the 2-layered system due to the coloring of complete cells and not just capsules. In this way it was ensured that cells – if color was present - were easily identified. The green signal, which arised from the capsules, was more crowded in the inner part. This can be slightly observed in the focus plane image on the right, which shows one plane in the z-direction. Unfortunately, some capsules were also found in the outer part as well (*cf.* 3D image in figure 34). This might be caused by free capsules still present during the addition of the secondary cells. The new cells (red) then took up these free capsules which made them end up in outer parts as well. Removal before secondary uptake was not possible because a washing step might have also damaged the forming spheroids. In addition, the majority of the secondary cells did grow onto one side of the initial spheroid. Accordingly, the intended full wrapping was not achieved. It seems that simultaneous control over purification, localization and growth is hard to manage. Hence, the idea of two sperate layers was dismissed. The results, nevertheless, provide an additional guarantee for sufficient spread of capsules across the spheroids.

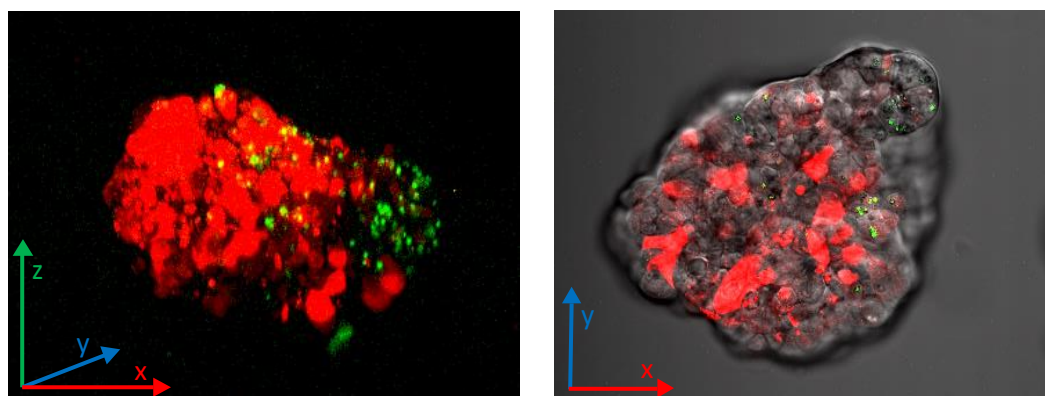


**Figure 34:** **2-layered spheroids: Complete 3D-structure vs. one focus plane.** By growth on secondary cells (red) on a preformed capsule-containing (green) spheroid it was tried to achieve a 2-layered spheroid. However, some capsules and some red cells ended up inside the opposite layer.

## 8.4 Capsule-Opening at Deep Levels

With availability of pervaded spheroids, the opening possibility and efficiency could be tested. Capsules at deep tissue levels were chosen as test objects due to reduced opening potential in comparison to their surface counterparts. For the first trial, the capsules were bleached with 10 % laser power ( $\lambda_{\text{bleach}} = 800 \text{ nm}$ ,  $P_{10\%} = 283 \text{ mW}$ ) for around one second. As the exact illumination area differed for every individual laser irradiation process, the energy was slightly different for each bleaching. In the opening process shown in figure 35 the delivered energy amount was equal to  $E = 285 \text{ mJ}$  (red circled capsule). This time series represents the first ever test run carried out at deeper tissue level. Shown are the phase contrast (top row) as well as the signals corresponding to the two dyes (*i.e.* red PI (second row) and green calcein (third row)). The bottom row represents an overlay of the three previous records. All data was recorded over time, starting from  $t = 0 \text{ s}$  and ending with the final picture (here: at  $t = 56.6 \text{ s}$ ). This procedure included a small period in time before the laser shot, the following irradiation process itself (here: at  $t = 5.05 \text{ s}$ ) and several shots after illumination to record early and late diffusion.

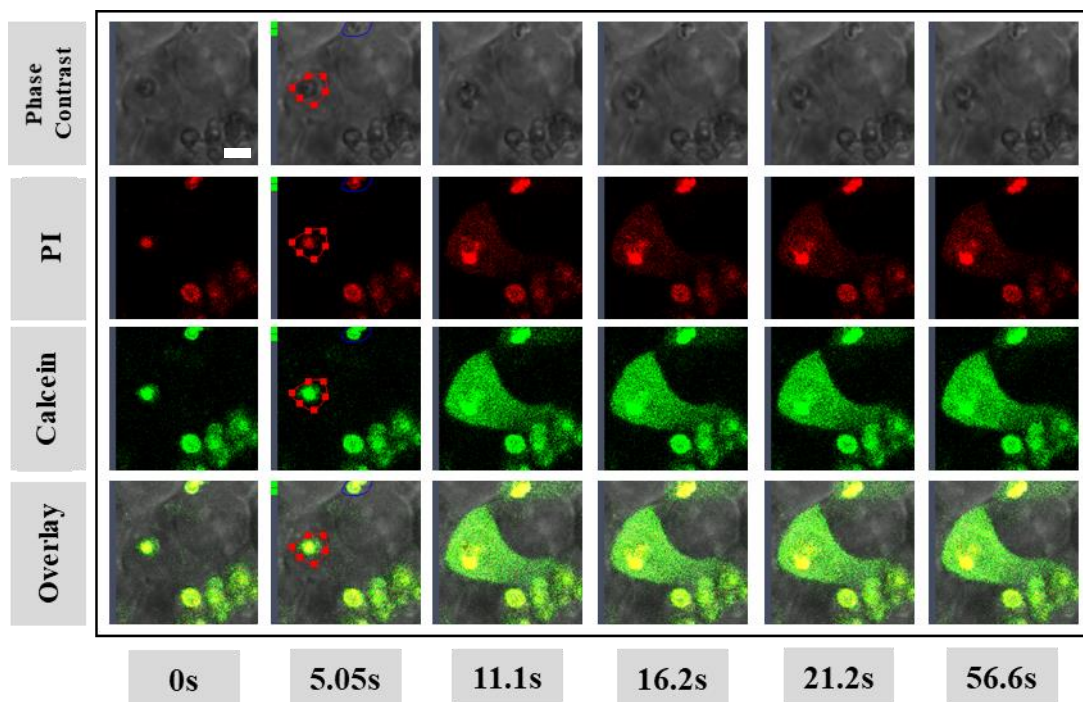


**Figure 35:** **First laser-induced opening of iron-based capsules at deep tissue level inside a MCF-7 spheroid.** During the initial opening trial at deep spheroid tissue level release of both encapsulated dyes was successfully achieved. Irradiated capsules contained IONPs as heat mediators.  
**Scale: 5  $\mu\text{m}$**

Corresponding to figure 35, both dyes show differences in both release behavior and final intensity during this initial run. Green color immediately occupied the whole cytosol with nearly

maximal intensity whereas red took slightly longer and showed less final intensity. The effect of drastic differences in diffusion speed fits the corresponding literature. PI has been classified as very slowly spreading, whereas calcein takes a place amongst very rapid examples.<sup>122</sup> The intensity differences are most likely related to discrepancies in encapsulated amounts of the two cargo substances.

Similar opening achievements were recorded for multiple positions in diversely shaped spheroids with various capsules. In every test, the laser was focused on individual targets to limit opening to a single capsule at a time. Resulting from that was typically a complete cargo delivery. Another example, connected to a different run, is shown below in figure 36. In addition to the time scale it also presents the overall spheroid shape and the capsule position inside. The shape image originates from one cut plane of the 3D-system's middle part.

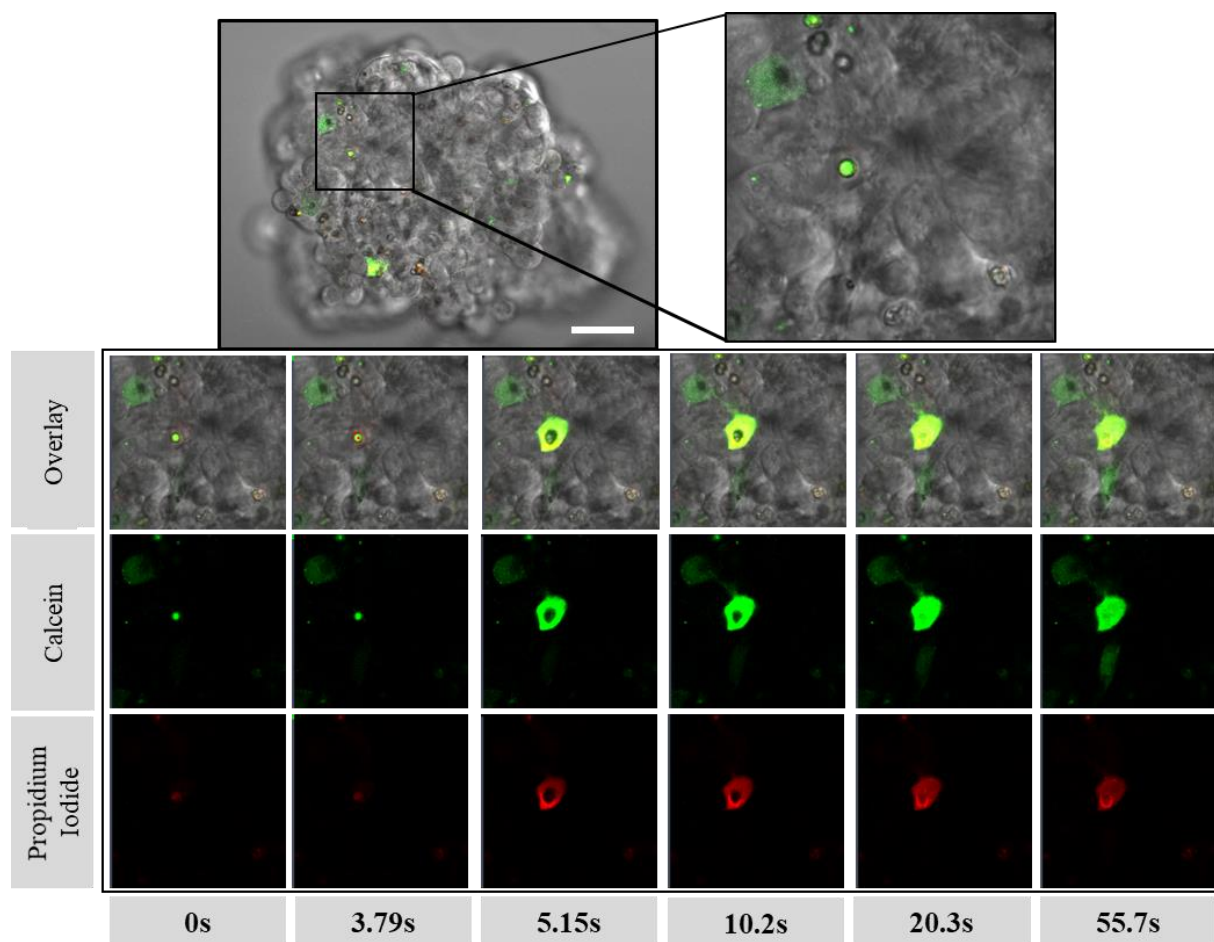


**Figure 36:** Deep tissue opening and the corresponding look into the spheroid. Multiple opening processes were run. In a typical measurement row the whole spheroid was imaged first. Then, a specific capsule was chosen and finally opened. All three steps are illustrated here. **Scale: 50 $\mu$ m**

The laser power was increased to  $P_{bleach} = 362.5$  mW for this specific run. Moreover, the irradiation area was slightly reduced to  $27.75 \mu\text{m}^2$  (example 1:  $32.18\mu\text{m}^2$ ) and the time immensely to 98 ms (example 1: 1.008 s). These changes caused an explicit drop in delivered energy to  $E = 35.525$  mJ, Despite the energy difference of around 200 mJ, capsule opening was still initiated. The cargo migration is clearly visible for both probes. After complete diffusion, the complete cell shape brightens up in yellow (green + red). In both presented cases, none of the colors was absent after liberation or decreased significantly with time. While PI binds to DNA and shows fluorescence for both dead and intact cells, calcein is capable to diffuse through damaged membranes of harmed cells. As a consequence, unhealthy cells loaded with both dyes would appear yellow immediately after cargo release but turn red over time due to disappearing calcein. Absence of color fade during both records allows for the claim that the whole imaging and trigger process occurred without noticeable negative effect on cell health. So, it has been accomplished to integrate capsules to the center part of a cell clump and initiate the delivery of their cargo behind micrometers of tissue without damage on the cells. In this way, a system for controlled initiation of deep level viability assays has been developed. It has to be mentioned, that both presented spheroids had similarly appearing surface and center structure, which suggests absence of hypoxia. However, it is well-known that tumors show cell death and hypoxic areas in the center after some time.<sup>146</sup> Certainly, the examined spheroids only had a short growth time (usually 2-3 days). Therefore, spheroids with growth time longer than a week were also tested. Likewise, no changes of the middle part were observed. This could be connected to two reasons: 1) MCF-7 spheroids require even longer times to form hypoxia and/or 2) the available spheroid size of  $300 \mu\text{m}$  falls below the size boundary for reduced oxygen diffusion.<sup>147</sup>

## 9 Summary/Outlook

The underlying concept of this secondary project consisted of the extension of light-triggered drug delivery. In detail, the two-dimensional principle of live/dead imaging with polymer capsules should be transferred onto 3D-spheroids. Under use of a laser, specific carriers located in the spheroids innermost part were chosen for disruption. Initially, set-up and capsules were tuned for this specific approach. Requirements included deep penetration depth of the light, successful but only on-demand opening and clear visibility of cell health. Choice of a NIR-laser for illumination, iron-oxide nanoparticles as heat sources and PI and calcein as staining reagents were the development outcome. In a following process, the localization and coverage of loaded PEMCs across the complete cell cluster, but especially in its center, was to be confirmed. The primary idea to form 2-layered spheroids with capsules just in the inner part, however, turned out to be troublesome. Nevertheless, presence of vehicles in their hub was observed for all tested single-layer spheroids. Final opening-trials under the formerly tuned conditions exhibited reliable liberation of freight at deep-tissue level during multiple runs. Thereby, by means of live/dead staining with the encapsulated fluorophores, no damage to the cells occupying the capsules was observed. In conclusion, the light-mediated cargo release was expanded onto 3D cell systems with simultaneous implementation of live/dead staining at deep tissue-level.

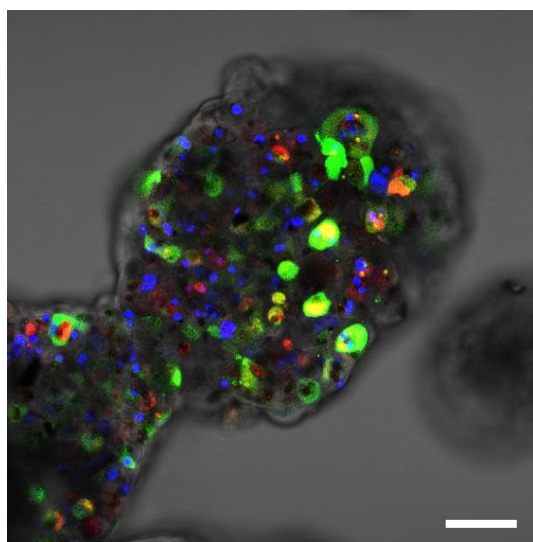


**Figure 37:**

**Outlook: Spheroid pervaded by two capsule types for damage and analysis simultaneously.** A spheroid was loaded with opposing capsules. Blue spheres represent Ce6 as cargo, which is a ROS inducing photosensitizer capable of damaging the cells. Red and green correspond to PI and calcein as live/dead-assay dyes. For a developed model, presence of both types in the same environment might allow for damage cause and subsequent evaluation in the same cell at deep tissue level.

**Scale: 50 $\mu$ m**

This principle could be carried forward as follows: Use of a local damage source could induce harm at a specific spot or cell inside the spheroid. Then, two-dyed capsules in close contact to the damage site, for instance in the same or neighboring cells, could be utilized to analyze the effect onto the living matter around. Not only would this represent a real-time tool for local health evaluation but it could also deliver information about communication between cells. In case of cell-to-cell transfer of damage, such outcome could be pointed out by opening of capsules in multiple surrounding cells. In fact, the execution of this idea has already been started allusively. Spheroids have been loaded with both the analysis-capsules and another capsule-type allowing for local damage. These secondary carriers were loaded with chlorine e6 (Ce6), a hydrophilic photosensitizer offering induction of reactive oxygen species (ROS) under illumination. Sufficient irradiation of such capsules should cause significant damage to the ambient cell due to massive ROS production. Figure 37 shows an example for a spheroid pervaded with both capsules. Blue spheres represent the damage source whereas red and green belong to still closed analysis tools or leached out dyes. Both variants are spread across the whole system. Execution of on-demand read out of induced damage has, however, not been fulfilled, yet. Trouble is caused by the factual damage from the ce6-capsules. Even though morphology changes showed up for seeded HeLa cells after illumination of Ce6, the live/dead assay delivered no decrease in viability. The interplay of both mechanisms, therefore, needs further investigation.

### III. Appendix

#### 10 Additional Tasks/Minor Projects

##### 10.1 Viability Assessment in MHS and CTLL-2 cells

The first minor project was focused on viability evaluation of two cell types when exposed to gold nanoparticles in their cell medium during incubation. Cell types included adherent animal macrophages gathered from mouse lung tissue (MHS) and non-adherent animal suspension T-cells gathered from mouse lymphocytes (CTLL-2). The overall idea of investigation was to examine viability over time against logarithmically increasing concentration of particles inside the medium. The maximum in exposure period was set to four days. Trials for cell health when co-incubated over time with particles were carried out inside 96-well plates with either 10,000 (MHS) or 40,000 (CTLL-2) cells per well. While the macrophages were allowed to attach for 24 h before NP addition, the suspended T-cells were immediately exposed to the particles. Concentration of gold inside the added solution ranged from a minimum of 0.1 pg/mL towards a maximum of 0.01 mg/mL. Based on the mean diameter of 4.1 nm ( $\sim M_w = 418$  kDa) the gold concentrations refer to particle concentrations in the regime from  $2.39 \times 10^{-7}$  nM to around 23,9 nM. In accordance with the contact duration, *i.e.* one, two, three or four days, four plates were seeded for each cell type. Each plate included all tested concentrations in triplets. In addition, control wells with pure medium took some of the remaining spaces. The mean of these control samples represented the 100 %-viability base value. Resazurin assays were acquired as comparison technique. The resulting viability results are shown below (figure A1). Therein, each graph corresponds to a specific time span of NP presence in the medium. Both cells showed strong resistance against damage arising from the particles at almost all concentrations. Especially for the MHS cells all viability points are located very close to the line showing full survivability. Small deviations are most-likely induced by slight discrepancies in real cell number per well. This shows brilliant viability of this macrophage type when in contact with significant amounts of gold nanoparticles even after four full days. Comparable behavior is present for the suspension cell. However, strong error bars indicate the significant influence of centrifugation on cell number. To change from medium to the assay substance, all cells had to be gathered by centrifugation. During the following collection from the pellet uneven numbers of cells might have been lost, which strongly affected data from different wells. As a consequence, some data points are noticeably above or below their predecessor. Clear spikes are present after 48 h exposure to the highest number and after 96 h exposure to medium

number of particles. At these conditions viability dropped up to almost 40 %. For all other conditions minimal damage occurred for both cell types when exposed to the gold particles. The fact that maximum concentration of particles did not damage the cells equally strong when exposed for longer than two days underlines the assumption of irregular initial cell number for this data point. Similarly, high concentrations didn't damage as much cells as the medium ones when exposed for 96 h. Accordingly, both spikes were most-likely caused by anything else but particle-related harm. As a whole, the trendlines follow the course of about 100 % viability for the majority of conditions. It can, therefore, be stated for both cell types that viability did not decrease when exposed to 4 nm gold nanoparticles for four days or shorter.

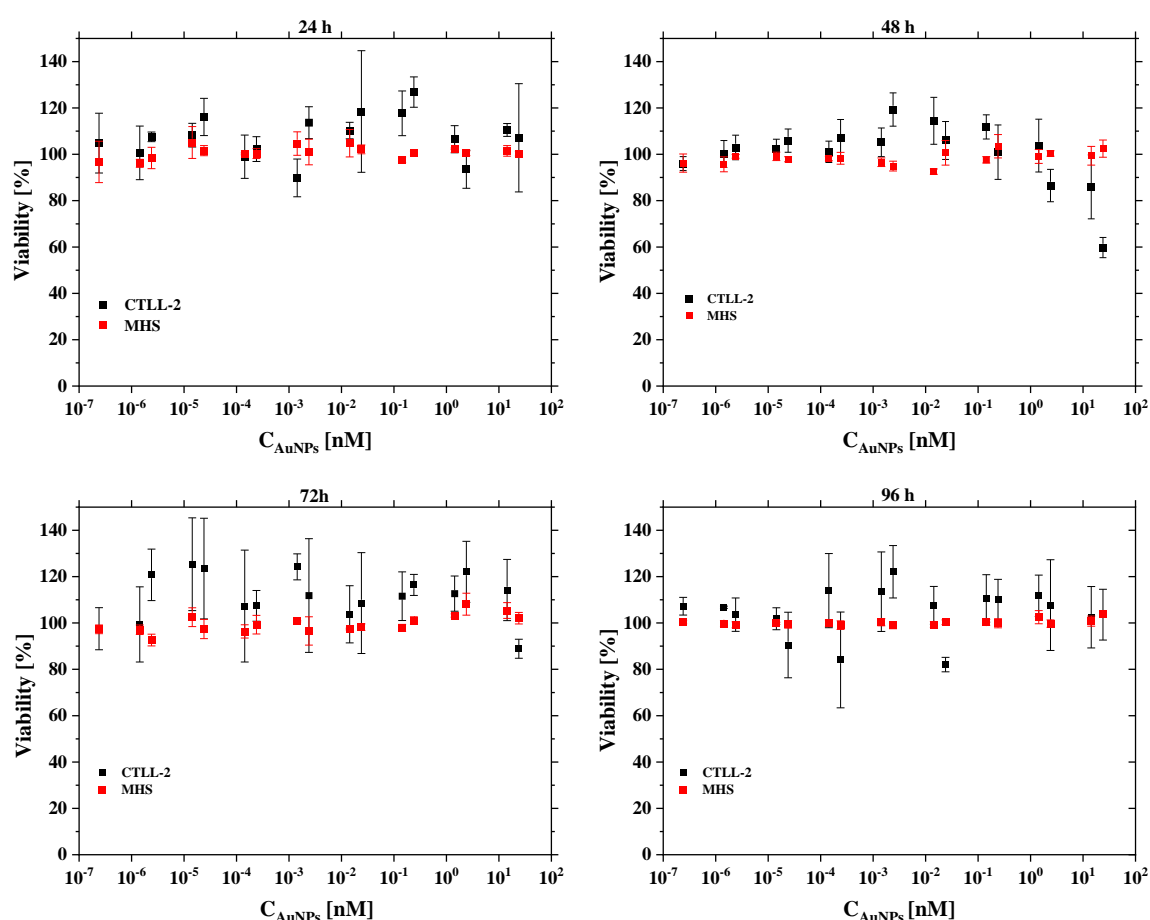


**Figure A1:**

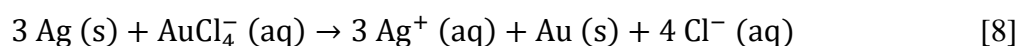
**Viability tests with MHS and CTLL-2 cells when exposed to AuNPs.**

Both cells were incubated with AuNPs at different concentration for 24 h (top left), 48 h (top right), 72 h (bottom left) or 96 h (bottom right) Viability checks were carried out after removal of free particles. Data points related to CTLL-2 cells show strong error bars caused by cell loss during medium exchange. However, no significant decrease in health was observed for any course and the majority of trendlines ranges at around 100 % viability.

## 10.2 Etching Au-Cages from Ag-Cube Templates

The second independent task was addressed to the preparation of gold nanocages (Au cages). Such cubic metal particles were intended as additional building units for the improvement of supramolecular organic frameworks (SOFs). The latter represent a porous 2D -or 3D-system similar to metal-organic frameworks (MOFs), whose components are interlinked by non-covalent interactions.<sup>148,149</sup> Introduction of cubic particles into the structure was expected to improve the order of the repeating units to form a highly uniform network.

In detail, Au cages were prepared and adjusted according to a fast route constructed by Skrabalak *et al.*<sup>150</sup> Briefly, silver templates were gained by a sulfide-mediated polyol method. Presence of poly(vinyl pyrrolidone) (PVP) and sodium sulfide thereby favored a cubic shape. In a subsequent galvanic replacement reaction, Ag cubes were transformed and etched to Au cages by addition of chloroauric acid. The affiliated reaction formula is listed below:



Initial production of silver cubes was carried out identical to the report for multiple batches. In many cases, silver did either precipitate or the color changes didn't occur. Similar outcome has been explained in the template by reasons like dirt on the stir bars, temperature discrepancies or absorbed water in the solvent. While dirt can be ruled out here due to very thorough cleaning with acetone and aqua regia, temperature did in fact permanently fluctuate around the desired 150 °C. As this behavior was caused by the heating plate, no impact could be made on it.

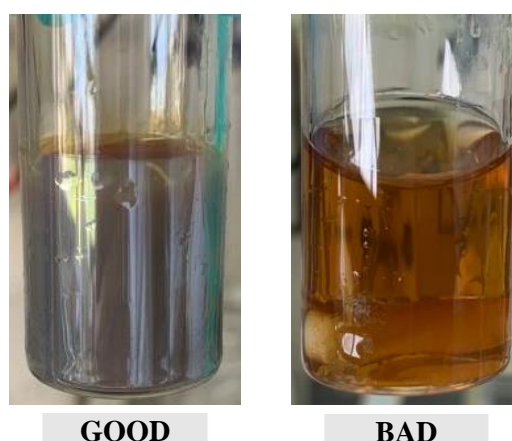


**Figure A2:** Comparison between good and bad outcome of Ag synthesis. Successful preparation of Ag cubes was indicated by a colour change towards ochre (left). In case of its absence, no cubes were achieved, and the batch was trashed (right).

In addition, the added ethylene glycol was not completely fresh so that trace amounts of water cannot be excluded completely. Long evaporation times with greater duration than the listed 60 min, which should further decrease H<sub>2</sub>O volume, did not increase the success rate significantly. On account of the obtainment of several decent Ag batches, it was, however, not worked on error coping. Prosperous syntheses were, according to literature, just identified by a solution color-change towards ochre going along with a red meniscus and silver plating. Figure A2 opposes both types of deliverables. While the ochre-colored solution on the left represents an optimal outcome, the yellow-colored one on the left doesn't. From the entirety of batches seven showed the desired color change towards ochre. Each cube batch was then characterized in terms of absorption as well as size and shape via UV/Vis spectroscopy and STEM, respectively. Despite their good color appearance, not all cubes turned out ideal during further analysis. Some batches showed irregular shape, others were not distributed monodisperse.

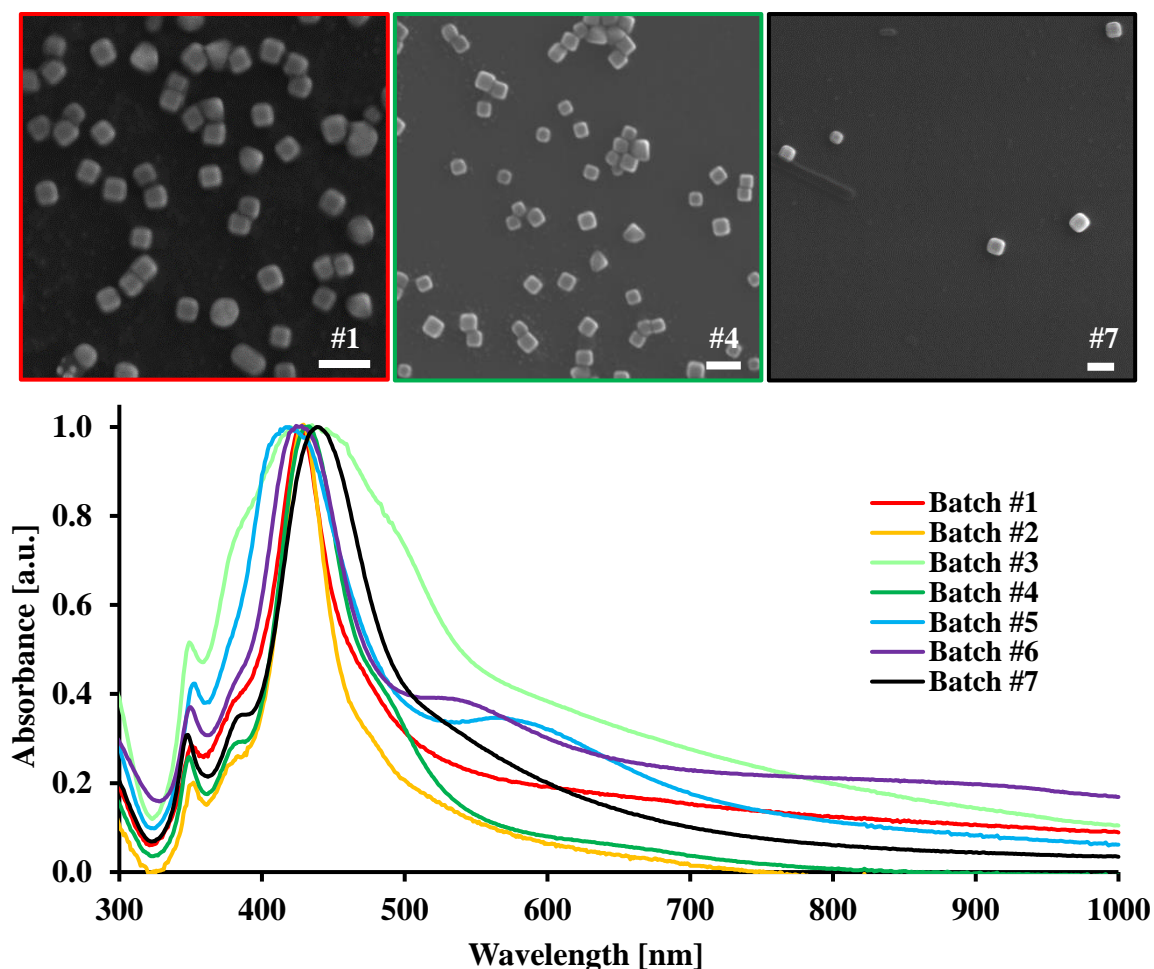


**Figure A3:** Characterization of silver batches by UV/Vis spectroscopy and STEM. All silver batches with ochre color were analyzed by UV/Vis first. Intended outcome included a sharp peak around 430 nm. Only the batches #1, #4 and #7 were considered good. Their corresponding STEM images (left to right) are shown above the spectra. **Scale: 100nm**

For a better clarity, the UV/Vis spectra of the seven batches are shown above (*cf.* figure A3). One parameter all spectra have in common is the peak location at about  $\lambda = 430 - 440$  nm, which overlaps with the results reported by Skrabalak *et al.*<sup>150</sup> Peak width and spectrum course, however, dramatically vary among the batches. Batch #3 (bright green) represents an example for a bad peak as it appears very broad and without sharp slopes. Batches #5 (blue) and #6 (purple) show an additional smaller peak at higher wavelengths, which is related to agglomerates. In contrast to that, batches #1 (red), #4 (dark green) and #7 (black) show ideal peak shape and only slightly differ in the exact wavelength of maximum absorption (*i.e.* #1: 427 nm, #4: 432 nm, #7: 439 nm). The corresponding TEM images for these cubes are shown in figure A3 as well. The main shape present are the desired cubes. As a consequence, these batches were considered successful and used for further etching with gold acid.



**Figure A4:** Comparison of failed Au-cage etching runs. During troubleshooting multiple etching runs didn't show desired color and spectrum. Bad colors included yellow, purple and dark blue.

The etching process turned out to be very challenging as added volumes of gold acid matching the literature template didn't result in suitable cages. Depending on the acid volume, the literature suggests an easy tunability to the desired cage size and solution color. However, individual adjustments had to be made to induce a sufficient etching process. Those concerned parameters like addition rate, concentration and volume of the acid but also concentration of PVP. Multiple runs with varying parameters were carried out to find a condition delivering similarly colored (light blue) cages with identical absorbance spectrum as published. Resulting solutions of different color can be seen in figure A4 which includes yellow, low-concentrated dark blue and purple but not the intended lighter and highly-concentrated blue. As a consequence, it was further tested to manipulate other parameters like the amount of added Ag-cube solution to increase the number of templates. In a final run, the expected color was finally observed and the corresponding spectrum matched the paper. For that, 500  $\mu$ L Ag-solution (batch #7), which represents 5-fold the reported volume, was added to a reaction vial together

with 5 mL of PVP solution ( $M_w \sim 40$  kDa, 26 mg/mL). The mixture was boiled for around 10 min at  $T = \sim 130$  °C. Then, 2mL of 0.444 mM gold acid were added dropwise at a rate of 498  $\mu\text{L}/\text{min}$  by a syringe pump. Achieved color and spectrum can be looked at in figure A5.

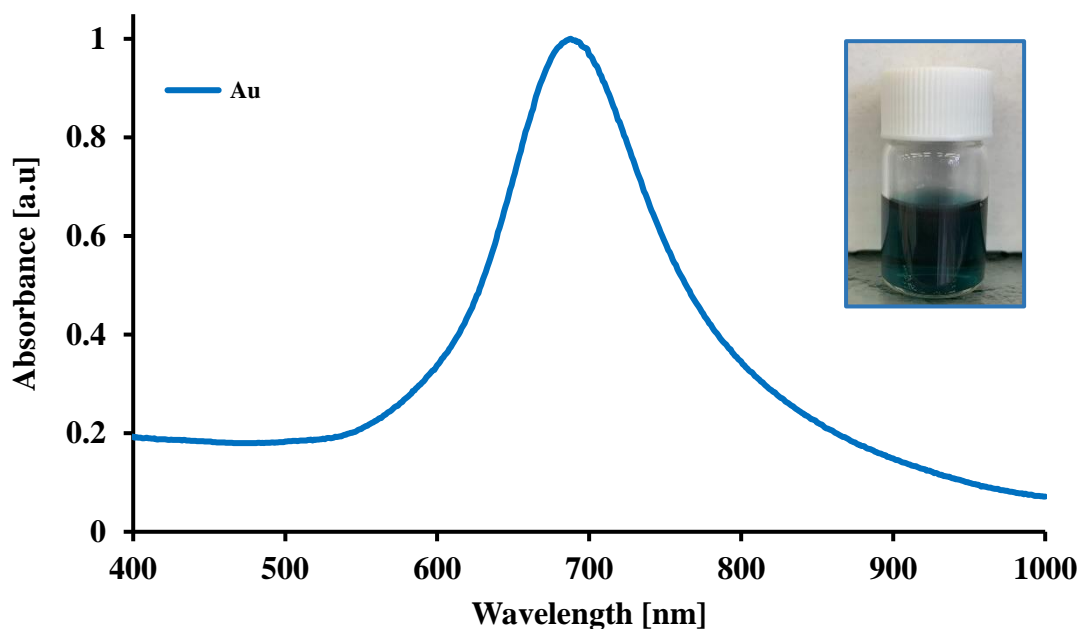


**Figure A5:** **Successful outcome of the etching process.** After several manque runs the final parameters delivered the intended color and the perfectly shaped spectrum at the desired wavelength ( $\lambda = 440$  nm).

The peak of the measured absorption spectrum is centered around the wavelength of  $\lambda = 440$  nm, which perfectly fits expectations. Moreover, it doesn't have any shoulders or secondary peaks across the evaluated regime being related to agglomerations or aggregations. In addition, the color appearance is the intended strong blue. Further investigation needs to take place to confirm the outcome but it can still be stated that significant progress was made to reproduce the reported synthesis route. Ideal parameters for a simple and fast preparation of the desired Ag cages at the available set-up have been found out.

## 11 Supporting Information

### 11.1 SAR values

In the process of particle tuning, multiple batches were synthesized and tested based on their capability to transform magnetic irradiation into heat. This behavior is characterized by the SAR value, which relates the output power to the mass of producing material. The complete library of batches strongly varied in the maximum value of the NPs. The majority ranged in the regime below 1000 W/g and several batches didn't even produce enough power to be measured. The entirety of batches with measurable SAR is shown in figure A6. Bars marked in red are linked to batches mentioned in the main project, which were used as magneto-responsive heat-mediators in capsule shells.

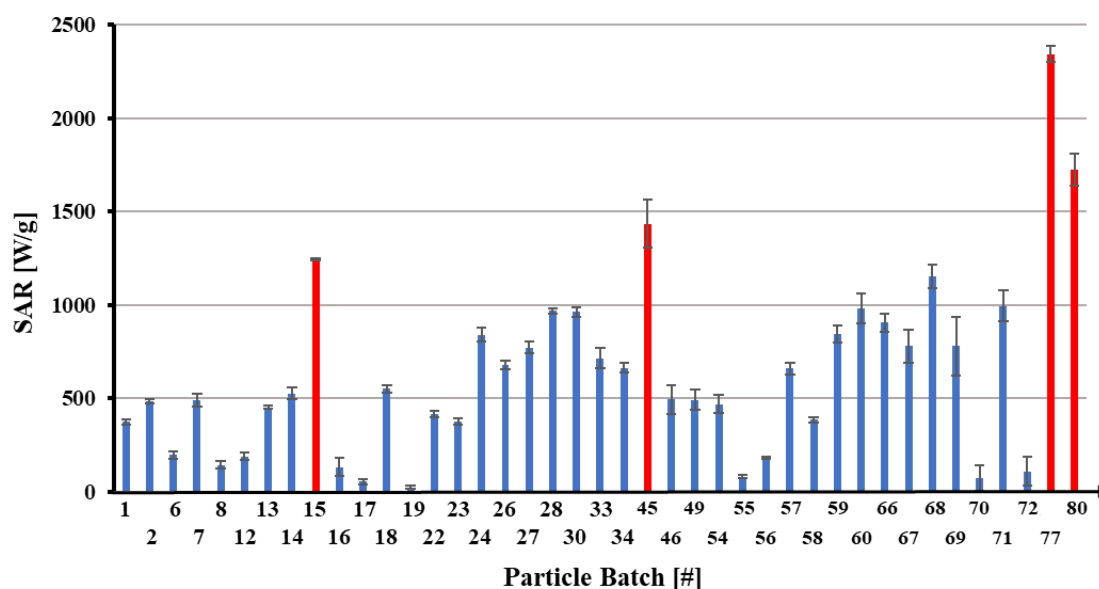


**Figure A6:** Summary of all measurable SAR values. Several batches of IONPs were synthesized and tested in terms of their heating capability. All values bigger than zero are presented here. Red bars are related to batches used for capsule functionalization in the main project.

### 11.2 Particle Chains

When dissolved in a liquid solvent, some particles tended to interact with close neighbors to form structures such as chains. Such a process was also observed for some library particle. Especially for the brilliant heaters from batch #77 and batch #80 this behavior was visible in the TEM images. Some particle structures for batch #77 are presented in figure A7. It shows the presence of long two-dimensional chains of individual IONPs. The scales refer to 100 nm.

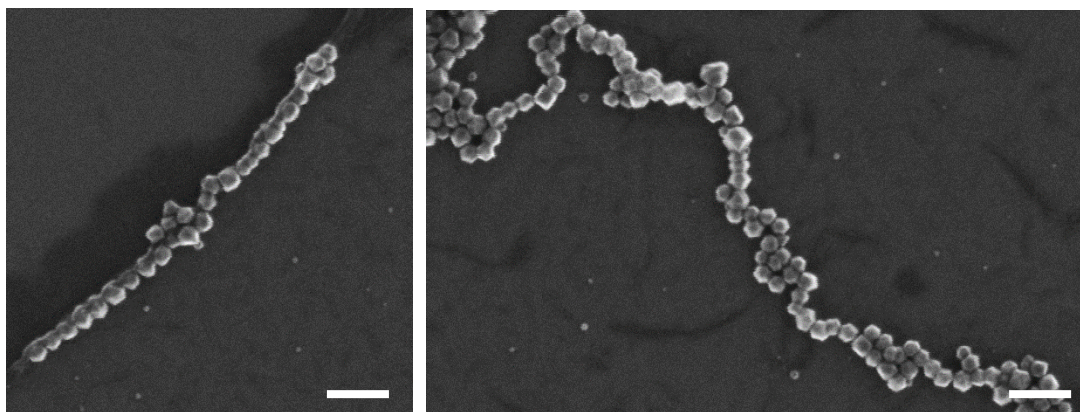


**Figure A7:** Presence of chains across TEM images from batch #77. Particles from batch #77 showed a favored formation of chain-like structures when observed by TEM. Scales: 100  $\mu\text{m}$

### 11.3 GNRs

To allow for interaction with laser light in terms of disruptive heating, some capsules were functionalized with GNRs. The corresponding absorbance spectrum with the major peak at  $\lambda = 940 \text{ nm}$  and a minor peak at  $\lambda = 511 \text{ nm}$  can be seen in figure A8. The minor peak enabled the use of the 514 nm laser-line of an Argon laser for illumination.

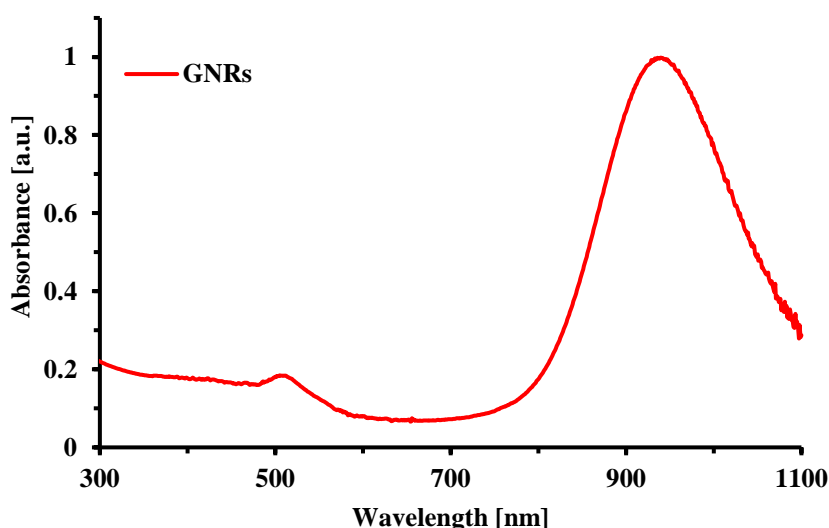


**Figure A8:** Absorbance spectrum of gold nanorods. The GNRs used as plasmonic heat mediators inside the capsules showed a major absorption peak at around 940 nm and a minor peak located around 511 nm. Correspondingly, the 514 nm Argon-laser line could be used for bleaching.

## 12 List of Hazardous Substances

**Table 5: List of chemicals and GHS classifications.**

| Substance                            | Signal word | GHS-symbols   | Hazard statements                       | Precautionary statements                             |
|--------------------------------------|-------------|---|---|--|
| Acetone                              | Danger      |    | 225, 319, 336, 373                      | 210, 240, 305+351+338, 403+233                       |
| Ammonium Bicarbonate                 | Warning     |    | 302                                     | 301+312+330  |
| Benzyl ether                         | Warning     |    | 317, 410                                | 261, 272, 273, 280, 302+352, 333+313                 |
| Biphenyl-4-carboxylic acid           | Warning     |    | 319                                     | 305+351+338  |
| Cadmium Acetate                      | Danger      |  | 302, 312, 332, 350, 410                 | 201, 261, 280, 302+352, 304+340, 312                 |
| Chloroauric Acid                     | Danger      |  | 290, 302, 314, 317, 373, 411            | 260, 273, 280, 303+361+353, 305+351+338, 314         |
| Chloroform                           | Danger      |  | 302, 331, 315, 319, 351, 361d, 336, 372 | 201, 273, 301+312+330, 302+352, 304+340+311, 308+313 |
| Diethylether                         | Danger      |  | 224, 302, 336                           | 210, 233, 240, 241, 301+312, 403+233                 |
| Dimercaptosuccinic acid              | Warning     |  | 315, 319, 335, 361                      | 302+352  |
| Dimethyldioctadecylamm onium bromide | Warning     |  | 315, 319, 335                           | 261, 310, 305+351+338,                               |

Appendix

|                                      |         |   |  |  |
|--------------------------------------|---------|---|--|--|
| (N,N-)<br>Dimethylformamide          | Danger  |    | 226, 312, 319,<br>332, 360               | 280, 308+313,<br>305+351+338,                            |
| Ethanol                              | Danger  |    | 225, 319                                 | 210, 280,<br>305+351+338                                 |
| Ethylenediamine-<br>tetraacetic acid | Warning |    | 319, 332, 373                            | 305+351+338  |
| Ethylene glycole                     | Warning |    | 302, 373                                 | 260, 264, 270,<br>301+312, 302,<br>314, 330, 501         |
| Fluorescein-5-<br>isothiocyanate     | Danger  |    | 302+332, 315,<br>317, 319, 334,<br>335   | 261, 272, 280,<br>284, 302+352,<br>333+313               |
| (n-) Hexane                          | Danger  |   | 225, 304, 361f,<br>373, 315, 336,<br>411 | 210, 240, 273,<br>301+310, 331,<br>302+352,<br>403+235   |
| Iron (III) acetylacetonate           | Warning |  | 302, 319                                 | 305+351+338  |
| Iron Chloride                        | Danger  |  | 290, 302, 315,<br>318                    | 280, 310,<br>305+351+338,                                |
| Iron pentacarbonyl                   | Danger  |  | 225, 300, 310,<br>330, 372               | 210, 280,<br>302+352, 310,<br>330, 304+340               |
| Octadecene                           | Danger  |  | 304, 413                                 | 301+310, 331   |
| Oleylamine                           | Danger  |  | 302, 304, 314,<br>335, 373, 410          | 260, 280,<br>303+361+353,<br>304+340+310,<br>305+351+338 |
| Polyethylenimine,<br>branched        | Warning |  | 302, 314, 317,<br>319, 411               | 273, 280,<br>305+351+338                                 |
| Propidium Iodide                     | Warning |  | 315, 319, 335,<br>341,                   | 261,<br>305+351+338                                      |

|                      |        |  |  |  |
|----------------------|--------|--|--|--|
| Silver Nitrate       | Danger |  | 272, 314, 410                                | 210, 220, 260,<br>280, 370+378,<br>305+351+338,<br>308+310                       |
| Sodium Borate Buffer | Danger |  | 360FD  | 201, 280,<br>308+313   |
| Sodium Hydroxide     | Danger |  | 290, 314                                     | 280, 308+310,<br>301+330+331,<br>305+351+338,                                    |
| Sodium Sulfide       | Danger |  | 290, 301, 311,<br>314, 400                   | 280, 310,<br>301+330+331,<br>303+361+353,<br>305+351+338,                        |
| Tetrahydrofuran      | Danger |  | 225, 302, 319,<br>335, 351                   | 210, 280,<br>301+312+330,<br>305+351+338,<br>370+378,<br>403+235                 |
| Triethylamine        | Danger |  | 225, 302,<br>311+331, 314,<br>335            | 210, 280,<br>301+330+331,<br>303+361+353,<br>304+340+311,<br>305+351+338<br>+310 |
| Toluene              | Danger |  | 225, 361d,<br>304, 373, 315,<br>336          | 210, 240,<br>301+310+330,<br>302+352+314,<br>403+233                             |
| Trioctylamine        | Danger |  | 315, 319, 335,<br>360, 372, 400,<br>410, 411 | 273, 302+352,<br>305+351+338   |

**Table 6: List of all cells used.**

| <b>Cell Classification</b> | <b>Organism</b> | <b>Tissue</b>  | <b>Phenotype</b> | <b>Type</b>           |
|----------------------------|-----------------|----------------|------------------|-----------------------|
| MCF-7                      | Human           | Breast         | Adherent         | Epithelial Cells      |
| HeLa                       | Human           | Cervix, Uterus | Adherent         | Epithelial Cells      |
| MHS                        | Mouse           | Lung           | Adherent         | Macrophage            |
| CTLL-2                     | Mouse           | Lymphocyte     | Suspension       | Cytotoxic T cell line |

---

## References

1. Langer, R. New methods of drug delivery. *Science* **249**, 1527-1533 (1990).
2. Chen, W., Cheng, C.-A. & Zink, J.I. Spatial, temporal, and dose control of drug delivery using noninvasive magnetic stimulation. *ACS nano* **13**, 1292-1308 (2019).
3. Dash, S., Murthy, P.N., Nath, L. & Chowdhury, P. Kinetic modeling on drug release from controlled drug delivery systems. *Acta Pol Pharm* **67**, 217-223 (2010).
4. Skirtach, A.G., Antipov, A.A., Shchukin, D.G. & Sukhorukov, G.B. Remote activation of capsules containing Ag nanoparticles and IR dye by laser light. *Langmuir* **20**, 6988-6992 (2004).
5. Radt, B., Smith, T.A. & Caruso, F. Optically addressable nanostructured capsules. *Advanced Materials* **16**, 2184-2189 (2004).
6. Angelatos, A.S., Radt, B. & Caruso, F. Light-responsive polyelectrolyte/gold nanoparticle microcapsules. *The Journal of Physical Chemistry B* **109**, 3071-3076 (2005).
7. Ochs, M., *et al.* Light-Addressable Capsules as Caged Compound Matrix for Controlled Triggering of Cytosolic Reactions. *Angewandte Chemie International Edition* **52**, 695-699 (2013).
8. Katagiri, K., Nakamura, M. & Koumoto, K. Magneto-responsive smart capsules formed with polyelectrolytes, lipid bilayers and magnetic nanoparticles. *ACS applied materials & interfaces* **2**, 768-773 (2010).
9. Lu, Z., *et al.* Magnetic switch of permeability for polyelectrolyte microcapsules embedded with Co@ Au nanoparticles. *Langmuir* **21**, 2042-2050 (2005).
10. Hu, S.-H., Tsai, C.-H., Liao, C.-F., Liu, D.-M. & Chen, S.-Y. Controlled rupture of magnetic polyelectrolyte microcapsules for drug delivery. *Langmuir* **24**, 11811-11818 (2008).
11. Yoo, J.-W., Irvine, D.J., Discher, D.E. & Mitragotri, S. Bio-inspired, bioengineered and biomimetic drug delivery carriers. *Nature reviews Drug discovery* **10**, 521-535 (2011).
12. Carregal-Romero, S., *et al.* Magnetically triggered release of molecular cargo from iron oxide nanoparticle loaded microcapsules. *Nanoscale* **7**, 570-576 (2015).
13. Loretta, L., *et al.* LbL multilayer capsules: recent progress and future outlook for their use in life sciences. *Nanoscale* **2**, 458-467 (2010).
14. Tiwari, G., *et al.* Drug delivery systems: An updated review. *International journal of pharmaceutical investigation* **2**, 2 (2012).
15. Sukhorukov, G.B., *et al.* Nanoengineered polymer capsules: tools for detection, controlled delivery, and site-specific manipulation. *Small* **1**, 194-200 (2005).
16. De Koker, S., *et al.* Polymeric multilayer capsules delivering biotherapeutics. *Advanced drug delivery reviews* **63**, 748-761 (2011).
17. Muñoz Javier, A., *et al.* Uptake of colloidal polyelectrolyte-coated particles and polyelectrolyte multilayer capsules by living cells. *Advanced materials* **20**, 4281-4287 (2008).
18. De Cock, L.J., *et al.* Polymeric multilayer capsules in drug delivery. *Angewandte Chemie International Edition* **49**, 6954-6973 (2010).
19. Esser-Kahn, A.P., Odom, S.A., Sottos, N.R., White, S.R. & Moore, J.S. Triggered release from polymer capsules. *Macromolecules* **44**, 5539-5553 (2011).
20. Figuerola, A., Di Corato, R., Manna, L. & Pellegrino, T. From iron oxide nanoparticles towards advanced iron-based inorganic materials designed for biomedical applications. *Pharmacological Research* **62**, 126-143 (2010).
21. Guardia, P., *et al.* One pot synthesis of monodisperse water soluble iron oxide nanocrystals with high values of the specific absorption rate. *Journal of Materials Chemistry B* **2**, 4426-4434 (2014).
22. Guardia, P., *et al.* Water-soluble iron oxide nanocubes with high values of specific absorption rate for cancer cell hyperthermia treatment. *ACS nano* **6**, 3080-3091 (2012).
23. Kim, D., *et al.* Synthesis of uniform ferrimagnetic magnetite nanocubes. *Journal of the American Chemical Society* **131**, 454-455 (2009).
24. Moon, S.H., *et al.* Ultrathin interface regime of core-shell magnetic nanoparticles for effective magnetism tailoring. *Nano letters* **17**, 800-804 (2017).

25. He, S., *et al.* Maximizing specific loss power for magnetic hyperthermia by hard–soft mixed ferrites. *Small* **14**, 1800135 (2018).
26. Noh, S.-h., *et al.* Nanoscale magnetism control via surface and exchange anisotropy for optimized ferrimagnetic hysteresis. *Nano letters* **12**, 3716-3721 (2012).
27. Tong, S., Quinto, C.A., Zhang, L., Mohindra, P. & Bao, G. Size-dependent heating of magnetic iron oxide nanoparticles. *ACS nano* **11**, 6808-6816 (2017).
28. Pankhurst, Q.A., Connolly, J., Jones, S. & Dobson, J. Applications of magnetic nanoparticles in biomedicine. *Journal of physics D: Applied physics* **36**, R167 (2003).
29. Tran, N. & Webster, T.J. Magnetic nanoparticles: biomedical applications and challenges. *Journal of Materials Chemistry* **20**, 8760-8767 (2010).
30. Gao, J., Gu, H. & Xu, B. Multifunctional magnetic nanoparticles: design, synthesis, and biomedical applications. *Accounts of chemical research* **42**, 1097-1107 (2009).
31. Wu, W., He, Q. & Jiang, C. Magnetic iron oxide nanoparticles: synthesis and surface functionalization strategies. *Nanoscale research letters* **3**, 397 (2008).
32. Akbarzadeh, A., Samiei, M. & Davaran, S. Magnetic nanoparticles: preparation, physical properties, and applications in biomedicine. *Nanoscale research letters* **7**, 144 (2012).
33. Kudr, J., *et al.* Magnetic nanoparticles: From design and synthesis to real world applications. *Nanomaterials* **7**, 243 (2017).
34. Bean, C. & Livingston, u.D. Superparamagnetism. *Journal of Applied Physics* **30**, S120-S129 (1959).
35. Gittleman, J., Abeles, B. & Bozowski, S. Superparamagnetism and relaxation effects in granular Ni-Si O 2 and Ni-Al 2 O 3 films. *Physical review B* **9**, 3891 (1974).
36. Kolhatkar, A., Jamison, A., Litvinov, D., Willson, R. & Lee, T. Tuning the magnetic properties of nanoparticles. *International journal of molecular sciences* **14**, 15977-16009 (2013).
37. Hao, R., *et al.* Synthesis, functionalization, and biomedical applications of multifunctional magnetic nanoparticles. *Advanced materials* **22**, 2729-2742 (2010).
38. Gupta, A.K. & Gupta, M. Synthesis and surface engineering of iron oxide nanoparticles for biomedical applications. *Biomaterials* **26**, 3995-4021 (2005).
39. Pankhurst, Q., Thanh, N., Jones, S. & Dobson, J. Progress in applications of magnetic nanoparticles in biomedicine. *Journal of Physics D: Applied Physics* **42**, 224001 (2009).
40. Tibbe, A.G., *et al.* Optical tracking and detection of immunomagnetically selected and aligned cells. *Nature biotechnology* **17**, 1210-1213 (1999).
41. Kularatne, B., *et al.* Monitoring tumour cells in the peripheral blood of small cell lung cancer patients. *Cytometry: The Journal of the International Society for Analytical Cytology* **50**, 160-167 (2002).
42. Van der Zee, J. Heating the patient: a promising approach? *Annals of oncology* **13**, 1173-1184 (2002).
43. Laurent, S., *et al.* Magnetic iron oxide nanoparticles: synthesis, stabilization, vectorization, physicochemical characterizations, and biological applications. *Chemical reviews* **108**, 2064-2110 (2008).
44. Qiao, R., Yang, C. & Gao, M. Superparamagnetic iron oxide nanoparticles: from preparations to in vivo MRI applications. *Journal of Materials Chemistry* **19**, 6274-6293 (2009).
45. Sun, S., *et al.* Monodisperse mfe<sub>2</sub>o<sub>4</sub> (m= fe, co, mn) nanoparticles. *Journal of the American Chemical Society* **126**, 273-279 (2004).
46. Xu, Y., Qin, Y., Palchoudhury, S. & Bao, Y. Water-soluble iron oxide nanoparticles with high stability and selective surface functionality. *Langmuir* **27**, 8990-8997 (2011).
47. Colombo, M., *et al.* Biological applications of magnetic nanoparticles. *Chemical Society Reviews* **41**, 4306-4334 (2012).
48. Khlebtsov, N.G. & Dykman, L.A. Optical properties and biomedical applications of plasmonic nanoparticles. *Journal of Quantitative Spectroscopy and Radiative Transfer* **111**, 1-35 (2010).
49. Xia, Y. & Halas, N.J. Shape-controlled synthesis and surface plasmonic properties of metallic nanostructures. *MRS bulletin* **30**, 338-348 (2005).
50. Huang, X. & El-Sayed, M.A. Plasmonic photo-thermal therapy (PPTT). *Alexandria journal of medicine* **47**, 1-9 (2011).

51. Olesiak-Banska, J., Waszkielewicz, M., Obstarczyk, P. & Samoc, M. Two-photon absorption and photoluminescence of colloidal gold nanoparticles and nanoclusters. *Chemical Society Reviews* **48**, 4087-4117 (2019).
52. Lu, X., Rycenga, M., Skrabalak, S.E., Wiley, B. & Xia, Y. Chemical synthesis of novel plasmonic nanoparticles. *Annual review of physical chemistry* **60**, 167-192 (2009).
53. Xia, Y. & Campbell, D.J. Plasmons: why should we care? *Journal of chemical education* **84**, 91 (2007).
54. Jiang, K., Smith, D.A. & Pinchuk, A. Size-dependent photothermal conversion efficiencies of plasmonically heated gold nanoparticles. *The Journal of Physical Chemistry C* **117**, 27073-27080 (2013).
55. Munoz Javier, A., *et al.* Photoactivated release of cargo from the cavity of polyelectrolyte capsules to the cytosol of cells. *Langmuir* **24**, 12517-12520 (2008).
56. Carregal-Romero, S., *et al.* NIR-light triggered delivery of macromolecules into the cytosol. *Journal of controlled release* **159**, 120-127 (2012).
57. Louis, C. & Pluchery, O. *Gold Nanoparticles For Physics, Chemistry And Biology*, (World Scientific Publishing Company, Singapore, SINGAPORE, 2012).
58. Huang, X. & El-Sayed, M.A. Gold nanoparticles: Optical properties and implementations in cancer diagnosis and photothermal therapy. *Journal of advanced research* **1**, 13-28 (2010).
59. Sperling, R.A., Gil, P.R., Zhang, F., Zanella, M. & Parak, W.J. Biological applications of gold nanoparticles. *Chemical Society Reviews* **37**, 1896-1908 (2008).
60. Dreaden, E.C., Alkilany, A.M., Huang, X., Murphy, C.J. & El-Sayed, M.A. The golden age: gold nanoparticles for biomedicine. *Chemical Society Reviews* **41**, 2740-2779 (2012).
61. Huang, X., Jain, P.K., El-Sayed, I.H. & El-Sayed, M.A. Plasmonic photothermal therapy (PPTT) using gold nanoparticles. *Lasers in medical science* **23**, 217 (2008).
62. Noh, S.-h., Moon, S.H., Shin, T.-H., Lim, Y. & Cheon, J. Recent advances of magneto-thermal capabilities of nanoparticles: From design principles to biomedical applications. *Nano Today* **13**, 61-76 (2017).
63. Deatsch, A.E. & Evans, B.A. Heating efficiency in magnetic nanoparticle hyperthermia. *Journal of Magnetism and Magnetic Materials* **354**, 163-172 (2014).
64. Perigo, E.A., *et al.* Fundamentals and advances in magnetic hyperthermia. *Applied Physics Reviews* **2**, 041302 (2015).
65. Kekalo, K., Baker, I., Meyers, R. & Shyong, J. Magnetic Nanoparticles with High Specific Absorption Rate at Low Alternating Magnetic Field. *Nano Life* **5**, 1550002 (2015).
66. Yu, Y., Williams, J.D. & Willets, K.A. Quantifying photothermal heating at plasmonic nanoparticles by scanning electrochemical microscopy. *Faraday discussions* **210**, 29-39 (2018).
67. Tee, S.Y., *et al.* Introduction to Photothermal Nanomaterials. (2022).
68. Baffou, G. & Quidant, R. Thermoplasmonics. in *World Scientific Handbook of Metamaterials and Plasmonics: Volume 4: Recent Progress in the Field of Nanoplasmonics* 379-407 (World Scientific, 2018).
69. Jaque, D., *et al.* Nanoparticles for photothermal therapies. *nanoscale* **6**, 9494-9530 (2014).
70. Becker, A.L., Johnston, A.P. & Caruso, F. Layer-by-layer-assembled capsules and films for therapeutic delivery. *Small* **6**(2010).
71. Antipov, A.A. & Sukhorukov, G.B. Polyelectrolyte multilayer capsules as vehicles with tunable permeability. *Advances in colloid and interface science* **111**, 49-61 (2004).
72. De Geest, B.G., Sukhorukov, G.B. & Möhwald, H. The pros and cons of polyelectrolyte capsules in drug delivery. *Expert Opinion on Drug Delivery* **6**, 613-624 (2009).
73. Petrov, A.I., Volodkin, D.V. & Sukhorukov, G.B. Protein—calcium carbonate coprecipitation: a tool for protein encapsulation. *Biotechnology progress* **21**, 918-925 (2005).
74. Matsusaki, M. & Akashi, M. Functional multilayered capsules for targeting and local drug delivery. *Expert opinion on drug delivery* **6**, 1207-1217 (2009).
75. De Geest, B.G., *et al.* Intracellularly degradable polyelectrolyte microcapsules. *Advanced materials* **18**, 1005-1009 (2006).
76. Duval, K., *et al.* Modeling physiological events in 2D vs. 3D cell culture. *Physiology* **32**, 266-277 (2017).

77. Kapałczyńska, M., *et al.* 2D and 3D cell cultures—a comparison of different types of cancer cell cultures. *Archives of medical science: AMS* **14**, 910 (2018).
78. Zhu, D., *et al.* Remotely controlled opening of delivery vehicles and release of cargo by external triggers. *Advanced drug delivery reviews* (2018).
79. Sharma, S.V., Haber, D.A. & Settleman, J. Cell line-based platforms to evaluate the therapeutic efficacy of candidate anticancer agents. *Nature reviews cancer* **10**, 241 (2010).
80. Goodspeed, A., Heiser, L.M., Gray, J.W. & Costello, J.C. Tumor-derived cell lines as molecular models of cancer pharmacogenomics. *Molecular Cancer Research* **14**, 3-13 (2016).
81. Breslin, S. & O'Driscoll, L. Three-dimensional cell culture: the missing link in drug discovery. *Drug discovery today* **18**, 240-249 (2013).
82. Zebli, B., Susha, A.S., Sukhorukov, G.B., Rogach, A.L. & Parak, W.J. Magnetic targeting and cellular uptake of polymer microcapsules simultaneously functionalized with magnetic and luminescent nanocrystals. *Langmuir* **21**, 4262-4265 (2005).
83. Kastl, L., *et al.* Multiple internalization pathways of polyelectrolyte multilayer capsules into mammalian cells. *ACS nano* **7**, 6605-6618 (2013).
84. De Duve, C. & Wattiaux, R. Functions of lysosomes. *Annual review of physiology* **28**, 435-492 (1966).
85. Bates, R.C., Edwards, N.S. & Yates, J.D. Spheroids and cell survival. *Critical reviews in oncology/hematology* **36**, 61-74 (2000).
86. Bewicke-Copley, F., *et al.* Extracellular vesicles released following heat stress induce bystander effect in unstressed populations. *Journal of extracellular vesicles* **6**, 1340746 (2017).
87. Belhadj Slimen, I., *et al.* Reactive oxygen species, heat stress and oxidative-induced mitochondrial damage. A review. *International journal of hyperthermia* **30**, 513-523 (2014).
88. Zhu, D., Feng, L., Feliu, N., Guse, A.H. & Parak, W.J. Stimulation of Local Cytosolic Calcium Release by Photothermal Heating for Studying Intra-and Intercellular Calcium Waves. *Advanced Materials (Deerfield Beach, Fla.)*, e2008261-e2008261 (2021).
89. Paracelsus, T. Die dritte Defension wegen des Schreibens der neuen Rezepte. *Septem Defensiones* **1538**, 508-513 (1965).
90. Riss, T.L., *et al.* Cell viability assays. in *Assay Guidance Manual [Internet]* (Eli Lilly & Company and the National Center for Advancing Translational Sciences, 2016).
91. Bratosin, D., Mitrofan, L., Palii, C., Estaquier, J. & Montreuil, J. Novel fluorescence assay using calcein-AM for the determination of human erythrocyte viability and aging. *Cytometry Part A: the journal of the International Society for Analytical Cytology* **66**, 78-84 (2005).
92. Kaneshiro, E.S., Wyder, M.A., Wu, Y.-P. & Cushion, M.T. Reliability of calcein acetoxymethyl ester and ethidium homodimer or propidium iodide for viability assessment of microbes. *Journal of microbiological methods* **17**, 1-16 (1993).
93. Lichtman, J.W. & Conchello, J.-A. Fluorescence microscopy. *Nature methods* **2**, 910-919 (2005).
94. Halhuber, K.-J. & König, K. Modern laser scanning microscopy in biology, biotechnology and medicine. *Annals of Anatomy-Anatomischer Anzeiger* **185**, 1-20 (2003).
95. Alford, W.J., VanderNeut, R.D. & Zaleckas, V.J. Laser scanning microscopy. *Proceedings of the IEEE* **70**, 641-651 (1982).
96. Ploem, J.S. Laser scanning fluorescence microscopy. *Applied optics* **26**, 3226-3231 (1987).
97. Paddock, S.W. Confocal laser scanning microscopy. *Biotechniques* **27**, 992-1004 (1999).
98. Benninger, R.K. & Piston, D.W. Two-photon excitation microscopy for the study of living cells and tissues. *Current protocols in cell biology* **59**, 4.11. 11-14.11. 24 (2013).
99. Drobizhev, M., Makarov, N.S., Tillo, S.E., Hughes, T.E. & Rebane, A. Two-photon absorption properties of fluorescent proteins. *Nature methods* **8**, 393-399 (2011).
100. Helmchen, F. & Denk, W. Deep tissue two-photon microscopy. *Nature methods* **2**, 932-940 (2005).
101. Wang, W., *et al.* Design of a multi-dopamine-modified polymer ligand optimally suited for interfacing magnetic nanoparticles with biological systems. *Langmuir* **30**, 6197-6208 (2014).
102. Chen, Z., *et al.* Preparation and characterization of water-soluble monodisperse magnetic iron oxide nanoparticles via surface double-exchange with DMSA. *Colloids and Surfaces A: Physicochemical and Engineering Aspects* **316**, 210-216 (2008).

103. Aposhian, H.V. DMSA and DMPS-water soluble antidotes for heavy metal poisoning. *Annual Review of Pharmacology and Toxicology* **23**, 193-215 (1983).
104. Song, L., Gu, N. & Zhang, Y. A moderate method for preparation DMSA coated Fe<sub>3</sub>O<sub>4</sub> nanoparticles. in *IOP Conference Series: Materials Science and Engineering*, Vol. 164 012026 (IOP Publishing, 2017).
105. Ahmadpoor, F., Masood, A., Feliu, N., Parak, W.J. & Shojaosadati, S.A. The Effect of Surface Coating of Iron Oxide Nanoparticles on Magnetic Resonance Imaging Relaxivity. *Frontiers in Nanotechnology* **3**, 13 (2021).
106. Pardo, A., *et al.* Cubic Anisotropic Co-and Zn-Substituted Ferrite Nanoparticles as Multimodal Magnetic Agents. *ACS Applied Materials & Interfaces* **12**, 9017-9031 (2020).
107. Zhang, W., *et al.* Optimization of the formation of embedded multicellular spheroids of MCF-7 cells: How to reliably produce a biomimetic 3D model. *Analytical biochemistry* **515**, 47-54 (2016).
108. Nack, L.M. Master Thesis, University of Hamburg (2019).
109. Park, J., *et al.* Ultra-large-scale syntheses of monodisperse nanocrystals. *Nature materials* **3**, 891 (2004).
110. Chen, R., *et al.* High-performance ferrite nanoparticles through nonaqueous redox phase tuning. *Nano letters* **16**, 1345-1351 (2016).
111. Iacovita, C., *et al.* Polyethylene glycol-mediated synthesis of cubic iron oxide nanoparticles with high heating power. *Nanoscale research letters* **10**, 391 (2015).
112. Li, Q., *et al.* Correlation between particle size/domain structure and magnetic properties of highly crystalline Fe<sub>3</sub>O<sub>4</sub> nanoparticles. *Scientific reports* **7**, 1-7 (2017).
113. Kita, E., *et al.* Heating characteristics of ferromagnetic iron oxide nanoparticles for magnetic hyperthermia. *Journal of Applied Physics* **107**, 09B321 (2010).
114. Park, Y.I., *et al.* Transformation of hydrophobic iron oxide nanoparticles to hydrophilic and biocompatible maghemite nanocrystals for use as highly efficient MRI contrast agent. *Journal of Materials Chemistry* **21**, 11472-11477 (2011).
115. Wang, M., Peng, M.-L., Cheng, W., Cui, Y.-L. & Chen, C. A novel approach for transferring oleic acid capped iron oxide nanoparticles to water phase. *Journal of nanoscience and nanotechnology* **11**, 3688-3691 (2011).
116. Bødker, F., Mørup, S. & Linderoth, S. Surface effects in metallic iron nanoparticles. *Physical review letters* **72**, 282 (1994).
117. Daniel, P., *et al.* The surface chemistry of iron oxide nanocrystals: Surface reduction of  $\gamma$ -Fe<sub>2</sub>O<sub>3</sub> to Fe<sub>3</sub>O<sub>4</sub> by redox-active catechol surface ligands. *Journal of Materials Chemistry C* **6**, 326-333 (2018).
118. Palma, S.I., *et al.* Effects of phase transfer ligands on monodisperse iron oxide magnetic nanoparticles. *Journal of colloid and interface science* **437**, 147-155 (2015).
119. Song, M., *et al.* Influence of morphology and surface exchange reaction on magnetic properties of monodisperse magnetite nanoparticles. *Colloids and Surfaces A: Physicochemical and Engineering Aspects* **408**, 114-121 (2012).
120. Mody, V.V., Singh, A. & Wesley, B. Basics of magnetic nanoparticles for their application in the field of magnetic fluid hyperthermia. *European Journal of Nanomedicine* **5**, 11-21 (2013).
121. Maldonado-Camargo, L., Unni, M. & Rinaldi, C. Magnetic characterization of iron oxide nanoparticles for biomedical applications. in *Biomedical Nanotechnology* 47-71 (Springer, 2017).
122. Brkovic, N., *et al.* Quantitative Assessment of Endosomal Escape of Various Endocytosed Polymer-Encapsulated Molecular Cargos upon Photothermal Heating. *Small* **16**, 2003639 (2020).
123. Domenici, F., *et al.* Differential effects on membrane permeability and viability of human keratinocyte cells undergoing very low intensity megasonic fields. *Scientific reports* **7**, 1-10 (2017).
124. Chen, K.-J., *et al.* A thermoresponsive bubble-generating liposomal system for triggering localized extracellular drug delivery. *ACS nano* **7**, 438-446 (2012).
125. Holleman, A. Lehrbuch der Anorganischen Chemie/Holleman-Wiberg. *de Gruyter, Berlin* **101**, 1118 (1995).

126. Chung, M.F., *et al.* A liposomal system capable of generating CO<sub>2</sub> bubbles to induce transient cavitation, lysosomal rupturing, and cell necrosis. *Angewandte Chemie International Edition* **51**, 10089-10093 (2012).
127. Engelmann, U.M., *et al.* Heating efficiency of magnetic nanoparticles decreases with gradual immobilization in hydrogels. *Journal of Magnetism and Magnetic Materials* **471**, 486-494 (2019).
128. Glöckl, G., *et al.* The effect of field parameters, nanoparticle properties and immobilization on the specific heating power in magnetic particle hyperthermia. *Journal of Physics: Condensed Matter* **18**, S2935 (2006).
129. Dennis, C.L. & Ivkov, R. Physics of heat generation using magnetic nanoparticles for hyperthermia. *International Journal of Hyperthermia* **29**, 715-729 (2013).
130. Branquinho, L.C., *et al.* Effect of magnetic dipolar interactions on nanoparticle heating efficiency: Implications for cancer hyperthermia. *Scientific reports* **3**, 1-11 (2013).
131. Mørup, S. Superferromagnetic nanostructures. *Hyperfine Interactions* **90**, 171-185 (1994).
132. Abenojar, E.C., Wickramasinghe, S., Bas-Concepcion, J. & Samia, A.C.S. Structural effects on the magnetic hyperthermia properties of iron oxide nanoparticles. *Progress in Natural Science: Materials International* **26**, 440-448 (2016).
133. Dennis, C., *et al.* The influence of collective behavior on the magnetic and heating properties of iron oxide nanoparticles. *Journal of Applied Physics* **103**, 07A319 (2008).
134. Dutz, S., Kettering, M., Hilger, I., Müller, R. & Zeisberger, M. Magnetic multicore nanoparticles for hyperthermia—influence of particle immobilization in tumour tissue on magnetic properties. *Nanotechnology* **22**, 265102 (2011).
135. Elkin, S.R., Lakoduk, A.M. & Schmid, S.L. Endocytic pathways and endosomal trafficking: a primer. *Wiener Medizinische Wochenschrift* **166**, 196-204 (2016).
136. Scott, C.C., Vacca, F. & Gruenberg, J. Endosome maturation, transport and functions. in *Seminars in cell & developmental biology*, Vol. 31 2-10 (Elsevier, 2014).
137. Smith, S.A., Selby, L.I., Johnston, A.P. & Such, G.K. The endosomal escape of nanoparticles: toward more efficient cellular delivery. *Bioconjugate chemistry* **30**, 263-272 (2018).
138. Martinez-Boubeta, C., *et al.* Learning from nature to improve the heat generation of iron-oxide nanoparticles for magnetic hyperthermia applications. *Scientific reports* **3**, 1652 (2013).
139. Laurent, S., Dutz, S., Häfeli, U.O. & Mahmoudi, M. Magnetic fluid hyperthermia: focus on superparamagnetic iron oxide nanoparticles. *Advances in colloid and interface science* **166**, 8-23 (2011).
140. Etheridge, M.L., *et al.* Accounting for biological aggregation in heating and imaging of magnetic nanoparticles. *Technology* **2**, 214-228 (2014).
141. Bedanta, S. & Kleemann, W. Supermagnetism. *Journal of Physics D: Applied Physics* **42**, 013001 (2008).
142. Mohapatra, J., Xing, M. & Liu, J.P. Inductive thermal effect of ferrite magnetic nanoparticles. *Materials* **12**, 3208 (2019).
143. Skirtach, A.G., *et al.* Laser-induced release of encapsulated materials inside living cells. *Angewandte Chemie International Edition* **45**, 4612-4617 (2006).
144. Hecht, S. Universität Hamburg (2020).
145. Ye, X., Zheng, C., Chen, J., Gao, Y. & Murray, C.B. Using binary surfactant mixtures to simultaneously improve the dimensional tunability and monodispersity in the seeded growth of gold nanorods. *Nano letters* **13**, 765-771 (2013).
146. Coleman, C.N. Hypoxia in tumors: a paradigm for the approach to biochemical and physiologic heterogeneity. *JNCI: Journal of the National Cancer Institute* **80**, 310-317 (1988).
147. Nunes, A.S., Barros, A.S., Costa, E.C., Moreira, A.F. & Correia, I.J. 3D tumor spheroids as in vitro models to mimic in vivo human solid tumors resistance to therapeutic drugs. *Biotechnology and bioengineering* **116**, 206-226 (2019).
148. Tian, J., Chen, L., Zhang, D.-W., Liu, Y. & Li, Z.-T. Supramolecular organic frameworks: engineering periodicity in water through host–guest chemistry. *Chemical Communications* **52**, 6351-6362 (2016).
149. Li, Y., *et al.* Shape-Controllable and Fluorescent Supramolecular Organic Frameworks Through Aqueous Host–Guest Complexation. *Angewandte Chemie* **130**, 737-741 (2018).

- 
150. Skrabalak, S.E., Au, L., Li, X. & Xia, Y. Facile synthesis of Ag nanocubes and Au nanocages. *Nature protocols* **2**, 2182-2190 (2007).
- [a] Wild CP, Weiderpass E, Stewart BW, editors (2020). World Cancer Report: Cancer Research for Cancer Prevention. Lyon, France: International Agency for Research on Cancer. Available from: <http://publications.iarc.fr/586>. Licence: CC BY-NC-ND 3.0 IGO.
- [b] Some of these results and the corresponding data were collected as part of a supervised thesis: N. Dageförde, Optimization of induced heating of magnetic nanoparticles towards magnetothermal release from endocytosed carrier particles, University of Hamburg, 2020.
- [c] modified from SMART Servier Medical Art, licensed under a Creative Common Attribution 3.0 Unported License. Available from: <https://smart.servier.com/>
- [d] nB NanoScale Biomagnetics, Calorimetry CoilSet User's Manual, 2020.
- [e] nB NanoScale Biomagnetics, Planar CoilSet User's Manual, 2020.

## Acknowledgements

All der Schweiß, der Fleiß und die Tränen waren eine Investition, die sich nun bezahlbar macht. Mit diesen letzten Worten kommen etliche Jahre an harter Arbeit und immensem Willen zu einem besonderen Ende. Doch dies wäre ohne die unermüdliche Unterstützung, die ich erfahren habe, schlichtweg unmöglich gewesen.

Daher gilt mein höchster und uneingeschränkter Dank zuallererst meiner Familie: Meiner Mutter, die mit jeder Faser (und Faszie 😊), mit permanenter Hilfe und mit einer schieren Willensleistung schon seit meiner Geburt zurücksteckt, um mir ein großartiges Leben zu ermöglichen. Und meinem Vater, der von oben über mich wacht, mich auf Schritt und Tritt begleitet, mir das Wissen, die Ruhe und die Konstanz in die Wiege gelegt hat und mich zu dem Menschen gemacht hat, der ich heute bin. Hättet ihr mir nicht unter die Arme gegriffen, wäre die Last dieses Weges vielleicht sogar zu schwer gewesen.

Ein weiterer Anker, der mich immer auf dem Boden der Tatsachen gehalten und vorm Überflügeln bewahrt hat, sind die Menschen, die ich wie eine zweite Familie betrachte. In erster Linie mein bester Freund Sascha, der nun schon mehr als ein Jahrzehnt mit mir durch Dick und Dünn geht und auf den trotz einiger Widrigkeiten stets Verlass ist. Eines Tages sitzen wir mit grauen Haaren und qualmender Pfeife gemeinsam auf der Veranda eines unserer Häuser und schmunzeln über die erlebten Tage und Erlebnisse unserer Jugend.

Auf beruflicher Seite danke ich vorrangig Prof. Dr. Wolfgang Parak für die Möglichkeit, meiner universitären Laufbahn dieses i-Tüpfelchen zu verleihen. In meiner Heimatstadt promoviert haben zu können, bedeutet mir sehr viel. Großer Dank gilt auch Dr. Dingcheng Zhu, der mir in der Anfangsphase stets hilfreich zur Seite stand und mit seinen Ideen vieles erleichtert hat.

Zusätzlich zu erwähnen sind all diejenigen, die ich im Verlauf kennenlernen durfte. Ob nur ein kurzer Mittagspausenschnack oder doch eine längere Diskussion – all diese Geschehnisse bleiben sicher verwahrt und gespeichert. Speziell die Personen, welche mit einem Aquarium nicht nur Fische assoziieren, sind hiermit direkt angesprochen. Bleibt geschmeidig und zielstrebig!

Für die finanzielle Grundlage und Förderung gilt eine ganz spezielle Anerkennung dem Bundesministerium für Bildung und Forschung (BMBF), ohne deren Unterstützung die ganze Ausarbeitung nie stattgefunden hätte.

Gehabt Euch wohl!

## Eidesstaatliche Erklärung

Hiermit versichere ich an Eides statt, die vorliegende Dissertation selbst verfasst und keine anderen als die angegebenen Hilfsmittel benutzt zu haben. Die eingereichte schriftliche Fassung entspricht der auf dem elektronischen Speichermedium. Ich versichere, dass diese Dissertation nicht in einem früheren Promotionsverfahren eingereicht wurde.

With these words I certify that the present dissertation was composed independent and that no other resources than mentioned were used. The handed written version is similar to the electronically saved one. I certify that this work was not submitted in another doctorate process before.

---

Hamburg, 04.10.2022

Ort, Datum / Place, Date

A handwritten signature in black ink, appearing to read 'Black', written over a horizontal line.

Unterschrift/Signature